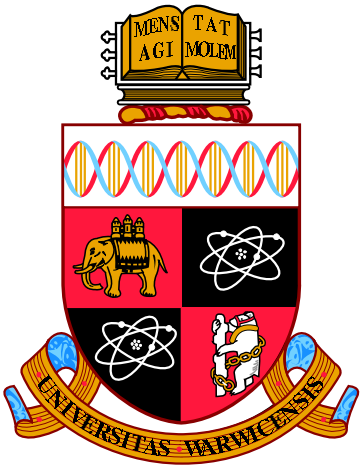


# Modelling Nanowires:
# Crystals Encapsulated in Carbon Nanotubes

by

**Samuel Brown**

**Thesis**

Submitted to the University of Warwick

for the degree of

**Doctor of Philosophy**

**Physics**

September 2016

THE UNIVERSITY OF
WARWICK

# Contents

# List of Tables

# List of Figures

Dedicated to my family
past, present and future.

# Acknowledgments

I am humbled to have benefitted from such good will and good fortune, and there are many more who deserve my thanks than I can mention here.

I would like to thank David Quigley, my supervisor, for his guidance, patience, experience and support throughout this project. I am indebted to past and current members of David Quigley's research group: Peter Brommer, Bart Vorselaars, Sally Bridgwater and Andrij Vasylenko have all at times been invaluable. Thanks are also due to my second supervisor, Jeremy Sloan, for interesting and useful discussion and for the opportunity to experience the experimental side of the field.

Many thanks to Nick Hine, whose assistance with ONETEP was extremely useful, and to James Kermode for his assistance with QUIP.

Anja Humpert, Gil Rutter and Mike Ambler have all made the experience heartwarming and nourishing, thank you. To all the rubber-ducks extraordinaires, particularly Dominic Branford and Nelson Yeung, thank you and good luck. Thanks also to the broader physics PhD community for making this an interesting, friendly and vibrant environment.

I am very grateful to Jake Langham, who has shared many useful insights, academic and personal, and to Rudolf Römer, who fostered my interest in computational science and quantum mechanics.

I would like to acknowledge the financial support I received from the EPSRC over the course of this project.

Finally, I would like to thank my family for their love and support, and Laurelin Griffiths for more than I could begin to list.

# Declarations

The work described in this thesis was carried out by the author at the University of Warwick between October 2012 and September 2016. The contents are the original work of the author except where otherwise indicated, and have not previously been submitted for any degree or qualification at this or another institution.

# Abstract

Nanotube-encapsulated ionic materials can be usefully modelled using *ab initio* methods to inform and validate experiment. This thesis models these materials using density functional theory, explores the specific challenges these materials pose, and presents results only visible once these challenges are addressed.

Chemical potentials and *ab initio* calculations are used to predict tube radii at which filling occurs for a range of filling conditions, which informs our choice of tube.

The practice of fitting both ionic core and encapsulating tube into the same unit cell causes artifical strain. A method of quantifying this mismatch is developed and the associated strain energy and distortions predicted.

Current methods of approximating the nanotube treat it as a smooth cylinder. We find significant texture which can resist core movement, allow metastable twisted states, and be used to determine which supercells have physically realistic mismatch strain.

Cores have previously been relaxed *in vacuo* with limited justification. We find that, in general, cores are not stable without constraints. We guide three bare silver iodide ansatze to metastable saddle-points by applying artifical symmetry constraints during *in vacuo* relaxation. An investigation into their unconstrained unstable phonon modes reveals them to be stabilised by an encapsulating tube. Two classes of stabilisation are identified, one due to radial encapsulation and a second due to mismatch-like effects.

Charge of a few tenths of $e$ per core ion is seen to transfer from core to tube, with magnitude depending on tube radius. In order to approximate the charge field by atomic charges, four population analysis schemes are investigated. The Bader and Density Derived Electrostatic and Chemical (DDEC) population analyses agree to physically sensible values while using different approaches. A machine-learned model is trained using local chemical-environment descriptors to transferrably predict atomic charges to within $0.004\,e$ of DDEC values with an orders-of-magnitude speedup.

# Abbreviations

AB@XY Material AB encapsulated in material XY

---

AFS Angular Fourier Series

AIRSS *Ab Initio* Random Structure Search

AO Atomic Orbital

BFGS Broyden–Fletcher–Goldfarb–Shannon extremisation algorithm

BPA Bader Population Analysis

BZ Brillouin Zone

CNT Carbon Nanotube

DDEC Density Derived Electrostatic and Chemical (charges or population analysis)

DFT Density Functional Theory

ESP Electrostatic Potential

FFT Fast Fourier Transform

GAP Gaussian Approximation Potential

GGA Generalised Gradient Approximation

GPR Gaussian Process Regression

GP Gaussian Process

| | |
|---|---|
| GTO | Gaussian-type orbitals (basis set) |
| HPA | Hirshfled Population Analysis |
| HRTEM | High-resolution Tunnelling Electron Microscopy |
| LAPW | Linearized Augmented Plane-wave |
| LDA | Local-density Approximation |
| LS-DFT | Linear-scaling DFT |
| MD | Molecular Dynamics |
| ML | Machine Learning |
| MM | Mismatch |
| MO | Molecular Orbital |
| MPA | Mulliken Population Analysis |
| MSM | Multilevel Summation Method |
| MVGD | Multi-variate Gaussian Distribution |
| MWCNT | Multiwall CNT |
| NAC | Net Atomic Charge |
| NCPP | Norm-conserving Pseudopotential |
| NGWF | Non-orthogonal Generalised Wannier Function |
| NIST | National Institute of Standards and Technology |
| NL | Non-local |
| NN | Neural Network |
| OTF | On-the-fly |

PAW Projector Augmented Wave

PBC Periodic Boundary Condition

PBE Perdew-Burke-Ernzerhof GGA

PES Potential Energy Surface

PP Pseudopotential

PW91 Perdew-Wang 1991 GGA

PW Plane-wave (basis set)

QED Quantum Electrodynamics

QEq Charge Equilibration

QM Quantum Mechanics

RPA Random Phase Approximation

SCF Self-consistent Field

SOAP Smooth Overlap of Atomic Positions

SWNT Single-walled Nanotube

TEM Tunnelling Electron Microscopy

TPSD Two-point Steepest Descent

USPP Ultrasoft Pseudopotential

XC Exchange-correlation

# Chapter 1

# Introduction

Carbon nanotubes (CNTs) have been a subject of much fascination and research over the last few decades, due to their unusual mechanical and electrical properties which depend significantly on radius and wrapping configuration. More recently the filling of these nanotubes has been investigated, with experimental success in encapsulating metals, salts and organic materials, even to the level of individual encapsulated atoms (see for example Chai et al. [1991]; Sloan et al. [2000, 2003]; Baldoni et al. [2007]). CNTs have been touted as templates for host material, and novel structures such as inorganic double-helices have been observed to form within the nanotubes [Philp et al., 2003]. The structure and properties of encapsulated materials are often quite different from those in bulk, due to the significant effects of close-packing which dominate coordination considerations.

Experimental synthesis is a major goal of condensed-matter physics, and microscopy, spectroscopy and other experimental techniques are the most reliable way to confirm the physical properties of particular materials. However, many properties are more easily examined at the atomic scale accessible with simulation, especially considering the fine control it permits. There is also the significant advantage of speed: a candidate material need not be physically synthesised for its properties to be predicted, and simulation allows broad predictive sweeps of potential systems to suggest promising subsets for more time-consuming experimental analysis.

The encapsulation of electron donors and acceptors can be used to alter the electronic properties of the nanotube [Eliseev et al., 2010; Lee et al., 2002]. While methods exist to address charge-transfer using chemical data, such as electronegativity equalization [Ferreira, 1963] which relies on the electronegativity of atomic species, true analysis of electron density and electronic structure requires more accurate quantum-mechanical (QM) simulation. At the condensed-matter scale of few

to hundreds (or even thousands) of atoms (and for systems which can be represented by an infinite periodic lattice with a unit cell of that size), electron density functional theory (DFT) [Martin, 2008] is commonly chosen as a good compromise between physical accuracy and computational tractability. This thesis uses DFT exclusively for its primary data, validated against and guided by experiment.

Modelling carbon is often the most expensive part of a DFT calculation of encapsulated material, owing to the multitude of carbon atoms required to surround any given system. Much of this thesis is aimed at numerically assessing the effect of the CNT on the host material, with a view to informing future 'pseudo-tube' approximations of CNT for inclusion in DFT simulations of encapsulated materials. With such approximations calculations could run much faster or simulate larger systems, allowing the exploration of longer-range behaviour or longer time-scale kinematics.

Existing pseudo-tube approximations have only ever taken the shape of smooth electrically-neutral cylindrical potentials [Fujimori et al., 2013; Carter et al., 2014; Bishop and Wilson, 2008, 2009a,b; Wilson, 2007]. A key property of the CNT which we investigate here is the physical texture of the wall, specifically how it deviates from a smooth cylinder and the energetic effect that such a deviation has. We also examine the importance of charge-transfer, which has so far been neglected in all pseudo-tube models. While our results are derived from DFT, we explore the possibility of charge-transfer prediction using machine-learning, which has been used previously to predict potential energies of systems to DFT accuracy with order-of-magnitude speedup. Charge-transfer prediction could be used to dynamically parameterise a pseudo-tube, or as part of a larger machine-learned potential.

An alternative approach to avoiding the expense of explicit CNT simulation is to neglect the tube completely. This has previously been used for certain systems to good effect, with predicted structures agreeing well with microscopy results. We attempt to use a similar approach for different systems, modelling AgI structures seen experimentally in encapsulation, but simulating them outside the tube, and explore ways to predict the encapsulated structure from this *in vacuo* simulation.

## 1.1 Outline of the thesis

The thesis is arranged as follows. In Chapter 2 we discuss *ab initio* approaches to material modelling, focusing on density-functional theory. Chapter 3 discusses methods of more coarse-grained atomistic modelling, including empirical potentials, as well as methods to assign point charges to atoms. It also describes various

machine-learning approaches to modelling the potential-energy surface. Chapter 4 focuses on the challenges particular to our systems of nanotube-encapsulated material, including the issue of mismatch between the tube and filling unit cells, and reviews the existing literature. In Chapter 5 we address the deviation of the encapsulating tube from the approximation of a simple confining cylinder, and explore the effect of encapsulation on unstable phonons of specific bare metal-halide wires. Chapter 6 examines the various methods of point-charge assignment in the context of our system of interest, leading to an investigation of charge-transfer between the filling and tube. The prediction of charges via machine-learning is also detailed. Many of our results show variation with respect to nanotube radius. The energetics of filling, with entropic considerations, are explored in Chapter 7, with the aim to inform the choice of radii chosen. Finally, Chapter 8 summarises our results.

# Chapter 2

# Ab-Initio Modelling

The laws which govern the world we see around us agree with the equations of quantum electrodynamics (QED) to better than one part in a billion [Hanneke et al., 2008]. In an ideal world, we could apply these equations to any model; unfortunately practical limitations such as data storage and computational speed require that we admit some level of approximation. Even the time-independent Schrödinger equation, when used naïvely, is impractical for investigation of multi-atom systems, requiring enormous amounts of data to store the multi-particle wavefunction.

However, the desire remains to model the world *ab initio*, both for its own sake and for the reliability and transferability of *ab initio* approaches over empirical ones, especially in exploratory regimes, and especially where electron density is of interest. It remains, then, to see what level of approximation is required for an approach to be practically useful while still producing reliable results and retaining the essence of the original equations.

### 2.0.1 Quantum Mechanics

The general time-dependent Schrödinger equation is given by

$$\hat{H}\Psi(\mathbf{R},t) = \left(-i\frac{\nabla^2}{2m} + V(\mathbf{R})\right)\Psi(\mathbf{R},t) = i\frac{\partial\Psi(\mathbf{R},t)}{\partial t}, \tag{2.1}$$

where $\hat{H}$ is the Hamiltonian of the time-dependent wavefunction $\Psi(\mathbf{R},t)$ and $\mathbf{R}$ contains the positions of all particles in the system. The standing wave solution $\Psi(\mathbf{R},t) = \Psi(\mathbf{R})\exp[iEt]$ gives the time-independent form $\hat{H}\Psi(\mathbf{R}) = E\Psi(\mathbf{R})$.

The much greater mass of the nuclei compared to electrons allows us to treat the electrons as moving in the field of stationary nuclei. This allows the Born-Oppenheimer approximation [Martin, 2008], wherein a condensed-matter system's

wavefunction $\Psi(\mathbf{R})$ is replaced by the electronic wavefunction $\psi_e(\mathbf{r}_e)$ (which depends on electronic positions $\mathbf{r}_e$) and nuclear wavefunction $\psi_Z(\mathbf{r}_Z)$ (which depends on nuclear positions $\mathbf{r}_Z$). $\psi_e$ can then be treated independently of $\psi_Z$ allowing the interaction between 'slow' nuclei and 'fast' electrons to be limited to an electrostatic potential felt by the electrons, reducing the complexity of the problem. If motion of the nuclei is of interest, for example when investigating relaxation or phonons, the nuclei can be modelled as responding classically to a relaxed electronic density. The neglect of more complex electron-nucleus coupling is often acceptable, though it precludes simulation of effects such as spin-spin coupling. Reducing the wavefunction to a purely electronic form also allows the use of Density Functional Theory (DFT), see §2.1.

## 2.1 Density Functional Theory

Even in a unit cell containing a relatively small number of electrons, solving the many-interacting-body system using the multi-particle wavefunction is a difficult problem. Fortunately, the Hohenberg-Kohn theorems [Hohenberg and Kohn, 1964] state that all observable quantities of an electronic system can be derived from the ground-state electronic density $n_0(\mathbf{r}) = \int |\Psi_0(\mathbf{r}, \mathbf{r}_2, \cdots, \mathbf{r}_N)|^2 \, \mathrm{d}\mathbf{r}_2 \cdots \mathrm{d}\mathbf{r}_N$ where $\Psi_0$ is the ground-state wavefunction [Martin, 2008]. A ground-state wavefunction can be written as a functional of the ground-state electron density [Hohenberg and Kohn, 1964], and therefore so can the ground-state expectation value of any observable, as

$$O[n_0] = \langle \, \psi[n_0] \mid \hat{O} \mid \psi[n_0] \, \rangle. \tag{2.2}$$

The strength of Density Functional Theory (DFT) stems from the Kohn-Sham equation [Kohn and Sham, 1965], where for any system of interacting electrons with wavefunction $\Psi(\mathbf{R})$ it is possible to construct a different, fictitious system which has the same density as the original interacting-electron system yet instead comprises the same number of non-interacting fermions with wavefunctions $\psi_i(\mathbf{r})$ moving in an effective potential. This reduces an intractable multi-body problem to a tractable set of single-body problems.

### 2.1.1 Exchange-correlation

The energy of a system is often the key to determining its physical properties, especially the change in energy as a function of some other varying property of the system.

The total energy of an interacting system of electrons is:

$$E[n] = T[n] + U[n] + V[n] \tag{2.3}$$

where $T$ is the kinetic energy of the system, $U$ is the energy of the electron-electron interaction and $V$ is the external potential, here $\int n(\mathbf{r})v(\mathbf{r})\,\mathrm{d}^3\,\mathbf{r}$ for the electron-nuclear interaction $v(\mathbf{r})$ where $\mathbf{r}$ spans real-space. The exact $T$ for a set of interacting electrons is not known, however that of a set of non-interacting electrons is

$$T_S[n] = -\frac{\hbar^2}{2m}\sum^{N}\int \phi^*\nabla^2\phi\,\mathrm{d}^3\,\mathbf{r}. \tag{2.4}$$

The difference between $T_S$ and $T$ is included in the exchange-correlation functional $\varepsilon_{xc}$, described shortly.

We approximate the electron-electron interaction as Coulombic:

$$U[n] \approx U_H[n] = \frac{q^2}{2}\int\int \frac{n(\mathbf{r})n(\mathbf{r}')}{|\mathbf{r}-\mathbf{r}'|}\,\mathrm{d}^3\,\mathbf{r}\,\mathrm{d}^3\,\mathbf{r}'. \tag{2.5}$$

Now our energy can be written as:

$$E[n] = T_s[n] + U_H[n] + E_{xc}[n] + E_{Ze}[n] + E_{ZZ} \tag{2.6}$$

where $T_s$ is the Kohn-Sham kinetic energy of a system of non-interacting fermions, $U_H$ is the Hartree energy, which relates to the electron density charge self-interaction, $E_{xc}$ is the sum of the exchange ($E_x$) and correlation ($E_c$) energies ($E_{xc} = E_x + E_c$), due to the anti-symmetric properties of the electron wavefunction, $E_{Ze}$ is the local electron-nucleus interaction and $E_{ZZ}$ is the nucleus-nucleus interaction. This has the advantage that $E_{XC}$ is typically much smaller than the other terms, while containing the physics we neglected in our approximations: $T - T_S$ and $U - U_H$. This neglected physics comprises the exchange interaction (sometimes called Fermi correlation) $E_X$ and electron correlation (sometimes called Coulomb correlation) $E_C$, such that $E_{XC} = E_X + E_C$. $E_X$ corresponds to the electrons' mutual avoidance due to their antisymmetric wavefunctions, whereas $E_C$ corresponds to many-body effects which cannot be described by the single Slater-Determinant form of Hartree-Fock theory.

While $E_{XC}$ is unknown, various common approximations are successfully used. The Local-Density Approximation (LDA) [Ceperley and Alder, 1980] approximates the per-electron exchange-correlation $\varepsilon_{xc}^{hom}$ at density $n(\mathbf{r})$ as that of a

homogeneous electron gas with the same density:

$$E_{XC}^{LDA}[n(\mathbf{r})] = \int n(\mathbf{r})\varepsilon_{xc}^{hom}(n(\mathbf{r}))\,\mathrm{d}^3\,\mathbf{r}. \tag{2.7}$$

Structural properties calculated using this approximation are often good, and minimum-energy structures are normally well-predicted. However, this neglect of the density-gradient causes overbinding [Martin, 2008], which leads to errors such as underestimating lattice constants, overestimating bulk moduli and predicting phonons which are too stiff.

Generalised Gradient Approximations (GGAs) consider the gradient of $n(\mathbf{r})$ as well as its value:

$$E_{XC}^{GGA}[n(\mathbf{r})] = \int n(\mathbf{r})\varepsilon_{xc}^{hom}(n(\mathbf{r}))F_{xc}^{GGA}[n(\mathbf{r}), \nabla(n(\mathbf{r}))]\,\mathrm{d}^3\,\mathbf{r}. \tag{2.8}$$

Many GGA enhancement factors $F_{xc}^{GGA}$ exist, notably PW91 [Perdew and Wang, 1992] and PBE [Perdew et al., 1996]. These succeed in slightly over-correcting LDA's overbinding; related properties are in general (over-)corrected and much more accurate [Martin, 2008].

### 2.1.2 Self-consistent field equation

The Kohn-Sham equation [Kohn and Sham, 1965] links the energy $\epsilon_i$ to its associated single-particle wavefunction $\psi_i$ as

$$\left[-\frac{1}{2}\nabla^2 + \phi(\mathbf{r}) + \varepsilon_{xc}[n(\mathbf{r})]\right]\psi_i(\mathbf{r}) = \epsilon_i\psi_i(\mathbf{r}) \tag{2.9}$$

where $\phi(\mathbf{r})$ comprises the Hartree and external potential, $\varepsilon_{xc}$ is the exchange-correlation functional and

$$n(\mathbf{r}) = \sum_i |\psi_i(\mathbf{r})|^2 \tag{2.10}$$

where the sum is over the occupied states (in an insulator this is the lowest-energy states which can accommodate the modelled electrons, in a metal extra partially-occupied states must be included above the Fermi energy). It is a self-consistent field (SCF) equation, meaning that $\psi_i(\mathbf{r})$ and $n(\mathbf{r})$ are defined in terms of each other, as in $x = f(x)$. Values must be found for $\psi_i(\mathbf{r})$ and $n(\mathbf{r})$ which satisfy both the above equations simultaneously. This is not a simple case of simultaneous equations, but rather a non-linear eigenvalue problem.

SCF equations are usually solved iteratively. Random initial $\{\psi_i(\mathbf{r})\}$ are

taken, from which an initial $n(\mathbf{r})$ is easily calculated using Equation (2.10). This initial $n(\mathbf{r})$ is then used to construct the Hamiltonian of Equation (2.9), the eigenvectors of which become the new $\psi(\mathbf{r})$ which in turn create the new $n(\mathbf{r})$ and so on. The expansion coefficients from this SCF cycle can then be varied so as to minimise the total energy. Often this cycle will result in a convergent series for both $\psi(\mathbf{r})$ and $n(\mathbf{r})$. However, many other situations can arise instead of simple convergence, and there are many techniques for encouraging convergence, such as oscillation damping [Hartree, 1947] and density mixing (such as that of Pulay [1980]).

### 2.1.3 Minimisation

The classic steepest-descent method to iteratively minimise some function $f(\mathbf{x})$ [Cauchy, 1847] takes the form $\mathbf{x_{k+1}} = \mathbf{x_k} + \alpha_k d_k$ where the search direction $d_k = -\nabla f(\mathbf{x_k})$ and the step size $\alpha_k = \arg\min_\alpha f(\mathbf{x_k} + \alpha d_k)$. In describing the two-point steepest-descent (TPSD) minimisation method, Barzilai and Borwein [1988] show that given two points in the iteration, $\mathbf{x_k}$ and $\mathbf{x_{k+1}}$, the secant method can be used to derive a step size $\alpha_k$ without an explicit line-search.

The Broyden–Fletcher–Goldfarb–Shanno (BFGS) algorithm is an iterative quasi-Newtonian extremisation method, in which the Hessian matrix is first approximated and then iteratively updated as the extremisation search progresses. More detail is given in standard textbooks e.g. Fletcher [2000].

### 2.1.4 Bloch theorem

A single gram of carbon contains approximately $5\times10^{22}$ atoms, each with 6 electrons. This is far too many to model explicitly, and so we treat the system as periodic and model only those atoms inside a unit cell. The Bloch theorem states that the wavefunction of a periodic system such as a repeated unit-cell need only have $|\psi(\mathbf{r})|^2$ be periodic, and so many wavefunctions $\psi_\mathbf{k}(\mathbf{r})$ with arbitrary cell-to-cell phase precession are valid. Each such $\psi_\mathbf{k}(\mathbf{r})$ can be split into a periodic function $u_\mathbf{k}(\mathbf{r})$ and a phase-factor $\exp[i\mathbf{k}\cdot\mathbf{r}]$ [Martin, 2008], as follows:

$$\psi_\mathbf{k} = \sum_{j=1}^{N} c_j e^{i(\mathbf{G}_j+\mathbf{k})\cdot\mathbf{r}} = \left[\sum_{j=1}^{N} c_j e^{i(\mathbf{G_j}\cdot\mathbf{r})}\right] e^{i\mathbf{k}\cdot\mathbf{r}} = u_\mathbf{k}(\mathbf{r})\cdot e^{i\mathbf{k}\cdot\mathbf{r}} \tag{2.11}$$

where $\mathbf{G}_j$ is a reciprocal lattice vector, $\mathbf{k}$ is a wavevector restricted to the first Brilloin zone and $N$ is the number of plane-waves used in the approximation. The $c_j$ are coefficients which are optimised numerically subject to orthonormality such that they satisfy the Kohn-Sham equations [Kohn and Sham, 1965].

As an approximation to averaging by integrating over all k-points, a finite number of them can be chosen and their associated energies averaged. This lends itself well to parallel computation, as the computation can be split across processors by k-point, minimising inter-processor communication. Commonly, a small set of k-points is chosen, often distributed on a Monkhorst-Pack grid [Monkhorst and Pack, 1976] to cover the Brillouin zone efficiently and without bias. The size of the set of k-points is increased until convergence, though convergence is not generally monotonic.

The $\Gamma$ point is the point in reciprocal space where $\mathbf{k} = 0$. It gives rise to many exploitable symmetries, to the extent that for sufficiently large cells accurate approximations to many properties can be computed using just the $\Gamma$ point.

### 2.1.5 Wavefunction representations

To model a system quantum-mechanically, we must have a representation of its wavefunction. Any complete basis set can be used to decompose a wavefunction, though our choice must be one where a finite manageable number of basis functions gives a reasonable representation. If the truncation of a basis set is required, the contribution of neglected terms must be bounded.

Two commonly used basis sets are the plane-wave set (PW) and atomic-like orbitals, including Gaussian type orbitals (GTO). Each of these approaches has its respective benefits, and each is implemented in various codes.

PW is well-suited to periodic systems, for example a unit cell with periodic boundary conditions, and has a simple measure of basis-set quality: the included plane-wave with the shortest wavelength. This is the approach taken by the CASTEP code [Clark et al., 2005], used in this thesis.

GTO consists of atom-centred Gaussians and so has an advantage when representing large vacuum gaps or non-periodic systems, however the relative quality of GTO-type basis sets is difficult to determine. GTO also struggles in situations where electrons are delocalised, many terms are needed to capture conduction bands which are more naturally described with plane-waves.

Hybrid approaches also exist, such as Quickstep [Quickstep website] and the Linearised-Augmented Planewave (LAPW) approach used by the ELK code [ELK website]. A notable example is ONETEP [ONETEP website], which will be discussed in more detail in §2.2.

In each case, an infinite amount of basis-elements will be able to exactly represent any wavefunction. More importantly, well-behaved wavefunctions[1] can be

[1] 'Well-behaved' here is a heuristic term describing the wavefunctions of most physical systems.

represented to some desired finite accuracy using only a finite subset of elements of either basis.

For example, using a plane-wave basis-set, at the Γ point (see §2.1.4) a wave-function $\psi_\alpha$ of a single-particle $\alpha$ can be defined as

$$\psi_\alpha(\mathbf{r}) = \sum_{\mathbf{g}}{}' c_{\mathbf{g}} \exp[i\mathbf{g}\cdot\mathbf{r}] \tag{2.12}$$

where each $c_{\mathbf{g}}$ is the coefficient corresponding to the reciprocal lattice vector $\mathbf{g}$. The prime indicates that the basis summation can be truncated to finite number of $\mathbf{g}$-vectors by bounding by $|\mathbf{g}| \leq g_{\max}$, set with a cutoff energy such that $E_{\text{cutoff}} = \hbar^2 g_{\max}^2 / 2m_e$.

Clearly a longer expansion will more accurately represent the true wavefunction. Increasing the number of terms in the expansion, we can see convergence in the energy of the system as it gradually approaches the ground-state, see Figure 2.1. The convergence due to increasing coverage of the basis set is always from above, since any deviation from the ground-state increases the energy of the system. Typically this convergence eventually reaches a level where further terms make a negligible contribution and the sum can be safely truncated to a manageable size.

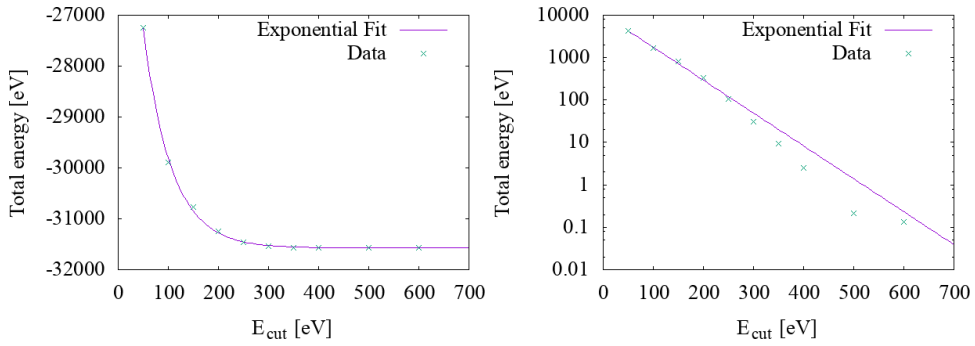


Figure 2.1: Convergence of total energy of a 200-atom unit-cell of (10-10) carbon nanotube, with respect to $E_{cut}$, at the Γ-point.

CASTEP also has an FFT grid [Segall et al., 2002] for storing the Fourier transform of the plane-wave basis set without aliasing, which is commonly set between 1/1.5 to 1/2 of the spacing of the standard grid, with this spacing controlled via the parameter `grid_scale`. In addition, the augmentation charge of ultra-soft pseudopotentials (see Section 2.1.6) can introduce high-frequency components into the charge density, requiring an even finer real-space grid which can be controlled via the `fine_grid_scale` parameter. Both grid spacings can be decreased to reach

Specifically, such a function is continuous, smooth and has a decaying power-spectrum.

convergence at smaller values of $E_{\text{cutoff}}$, increasing computational efficiency.

### 2.1.6 Pseudopotentials

In condensed-matter systems, the electronic wavefunctions tend to oscillate very rapidly close to the atomic nuclei, requiring a large PW basis set. However, these core electrons are typically well-localised and normally unaffected by the chemical environment. By comparison, the wavefunctions of valence electrons - those actively involved in chemical interactions - typically vary far more slowly.

Pseudopotentials (PPs) [Martin, 2008] are approximations of the core of an atom, they 'freeze' the core electrons along with the nuclear core, representing them as a much simpler effective potential, allowing a much smaller PW basis set to accurately reproduce the system's behaviour while simultaneously reducing the number of Kohn-Sham orbitals which need to be explicitly modelled. Many methods of pseudisation exist [Kresse and Joubert, 1999], including the Projector Augmented Wave (PAW) method of Blöchl [1994], however here we focus on the two used in this work.

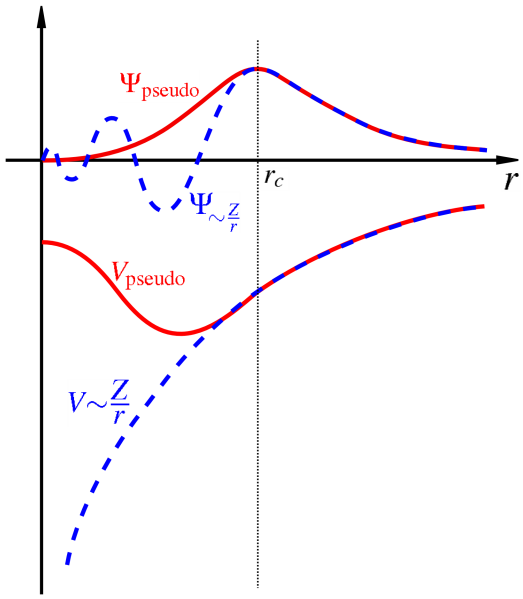


Figure 2.2: Sketch of the pseudisation of a wavefunction, without projectors. Here $r$ is distance from the nucleus. (Reproduced from wikimedia.org, public domain)

**Norm-Conserving Pseudopotentials**

One of the simplest forms of PP is the Norm-Conserving Pseudopotential (NCPP) [Hamann et al., 1979], consisting of a few simple requirements. Firstly the eigenvalues $\epsilon_l^{ps}$ of the pseudised electron with angular momentum $l$ must equal those of the reference all-electron wavefunction $\epsilon_l^{ae}$. The radial part of the pseudopotential, $\phi(r)_l^{ps}$, must be nodeless within some cutoff $r_c$ and equal to the radial part of the atomic valence wavefunction for $r > r_c$. Finally, as befits the name, the norms of the potentials within $r_c$ must be equal, that is $\langle \phi_l^{ps} | \phi_l^{ps} \rangle_{r_c} = \langle \phi_l^{ae} | \phi_l^{ae} \rangle_{r_c}$, or

$$\int_{r<r_c} |\phi_l^{ps}|^2 r^2 dr = \int_{r<r_c} |\phi_l^{ae}|^2 r^2 dr \tag{2.13}$$

**Ultra-Soft Pseudopotentials**

NCPPs, while a significant improvement on explicit treatment of core electrons, are still 'hard', in that they still require large PW basis sets. Ultra-soft pseudopotentials (USPPs) [Vanderbilt, 1990] relax the norm-conserving condition of NCPPs at the expense of introducing an augmentation-charge $Q_{lm} = \langle \phi_l^{ps} | \phi_m^{ps} \rangle_{r_c} - \langle \phi_l^{ae} | \phi_m^{ae} \rangle_{r_c}$. This allows the various constraints of the NCPP formulation to be relaxed, replaced with the requirement only that $\phi^{ps} = \phi^{ae}$ beyond $r_c$.

The price for this is the introduction of non-locality. To make up the charge deficit the valence charge density is now

$$n_v(\mathbf{r}) = \sum_i |\psi_i|^2 + \sum_{i,l,m} \langle \psi_i | \beta_l \rangle \, Q_{lm}(\mathbf{r}) \, \langle \beta_m | \psi_i \rangle \tag{2.14}$$

where the $\beta_i$ are the duals to the pseudo-wave-functions. A non-local potential $\hat{V}_{NL}$ must also be constructed from the $\beta_i$, so that the total $\hat{V}_{US} = V_{loc}(\mathbf{r}) + \hat{V}_{NL}$, where $V_{loc}(\mathbf{r})$ is some smooth function equal to $V_{ae}(\mathbf{r})$ beyond some cutoff.

## 2.2 Linear-Scaling DFT

The traditional plane-wave pseudopotential approach to DFT, while efficient and accurate, is subject to cubic scaling. This restricts the system size for which DFT can be sensibly harnessed, since a doubling of system-size requires an eight-fold increase in computational power.

The origin of this $\mathcal{O}(N^3)$ scaling is the delocalisation of the Kohn-Sham orbitals (see Figure 2.3), which must be explicitly orthogonalised, $\langle \psi_m | \psi_n \rangle = \delta_{mn}$. The number of orbital pairs scales as $N^2$, and the computational cost of a single

orthogonalisation scales as $N$ since the overlap integral spans the entire simulation volume, giving a total cost $\mathcal{O}(N^3)$.

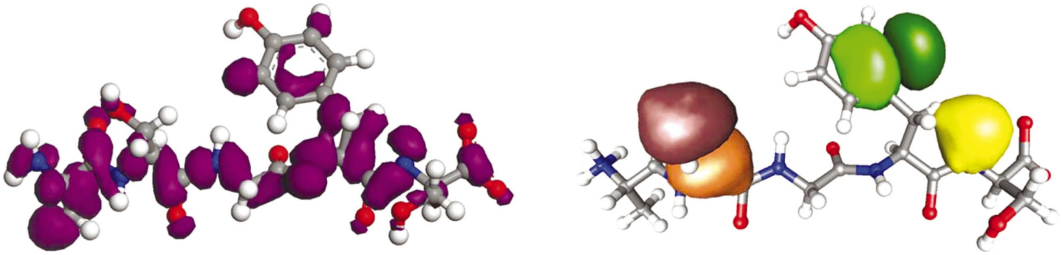

Figure 2.3: Left: A delocalised Kohn-Sham orbital from a conventional $\mathcal{O}(N^3)$ CASTEP calculation of an example peptide. Right: Three optimised NGWFs from an $\mathcal{O}(N)$ ONETEP calculation on the same peptide. Reproduced from [Skylaris et al., 2005].

Linear-scaling DFT has thus seen much interest (see e.g. review article [Galli, 1996]) and many approaches. Here we will focus on that taken by the ONETEP code, used in this thesis.

### 2.2.1 ONETEP

ONETEP is a density functional code which avoids delocalised orbitals [Skylaris et al., 2005], and so achieves $\mathcal{O}(N)$ scaling, though with a large prefactor which makes CASTEP faster for small $N$. Whereas a PW code such as CASTEP would express the single-particle density matrix $\rho(\mathbf{r},\mathbf{r}')$ as a sum of contributions from single-particle Bloch states $\psi_{nk}(\mathbf{r})$:

$$\rho(\mathbf{r},\mathbf{r}') = \sum_n f_n \frac{V}{(2\pi)^3} \langle \psi_{nk} | \psi_{nk} \rangle_{BZ} \tag{2.15}$$

where $f_n$ is the occupancy, BZ the Brillouin Zone and $V$ the simulation cell volume, ONETEP instead represents it as:

$$\rho(\mathbf{r},\mathbf{r}') = \sum_{\alpha\beta} \sum_R \phi_{\alpha R}(\mathbf{r}) K^{\alpha\beta} \phi^*_{\beta R}(\mathbf{r}') \tag{2.16}$$

where the sum over $R$ runs over lattice vectors [Skylaris et al., 2002, 2005]. The $\{\phi_{\alpha R}\}$ are spatially-localised, non-orthogonal functions, called Non-orthogonal Generalised Wannier Functions (NGWFs). $K^{\alpha\beta}$ is the representation of the density matrix in the duals of the NGWFs, and is called the density kernel. Exponentially decreasing "tails" of the density matrix allow the density kernel to be truncated by

enforcing the sparsification that $K^{\alpha\beta} = 0$ when $|\mathbf{r}_\alpha - \mathbf{r}_\beta| > r_{\text{cut}}$, where $\mathbf{r}_\alpha$ and $\mathbf{r}_\beta$ are the centers of $\phi_\alpha$ and $\phi_\beta$. Such truncation must be calibrated by comparison to untruncated calculations.

ONETEP specialises in large systems, where the unit cell is typically much larger than the primitive cell. This allows the Bloch-wave phase-factor that would otherwise be captured via the use of k-points to instead be captured explicitly, and so ONETEP energy calculations are restricted to the Γ-point. This ensures the NGWFs are real, and removes the dependence on $R$. In a similar manner to k-point convergence, the size of the supercell should thus be converged in ONETEP.

### NGWFs and the psinc grid

ONETEP's NGWFs $\phi_\alpha$ are expanded in a basis of periodic sinc (psinc) functions $\{D_k(\mathbf{r})\}$:

$$\phi_\alpha = \sum_k D_k(\mathbf{r}) C_{k,\alpha}. \tag{2.17}$$

where $C_k, \alpha$ are the psinc coefficients.

These psinc functions are highly localised, and the index $k$ labels their position on a grid. The spacing of this grid is tunable analogous to the plane-wave cutoff in PW codes, such that the psinc basis can by systematically and transferably improved. Convergence of the psinc grid spacing closely follows that of CASTEP's $E_{cut}$ [Skylaris et al., 2005].

The maximum grid spacing is a primary means of controlling the accuracy of ONETEP calculations. However, systems with an equal maximum grid spacing but different simulation cell sizes may have a different number of psinc functions, leading to discontinuities in derivative quantities, see for example Figure 2.4. This can be avoided by explicitly setting the number of grid points, taking care that the coarsest grid is still converged.

A localisation sphere of radius $r_{loc}^{\alpha}$ is also imposed, such that only psinc functions within the sphere can contribute to the expansion in Equation (2.17). Convergence of these NGWF radii is also required. We have therefore a truncation of the density kernel when the NGWF centers are far apart, allowing the linear scaling [Skylaris et al., 2005]. This should be an accurate assumption for insulators, where the NGWFs decay exponentially. The case of simulation of band-gapless systems without an $\mathcal{O}(N^3)$ diagonalisation of the Hamiltonian is less clear [Ruiz-Serrano and Skylaris, 2013; Bell et al., 2015].

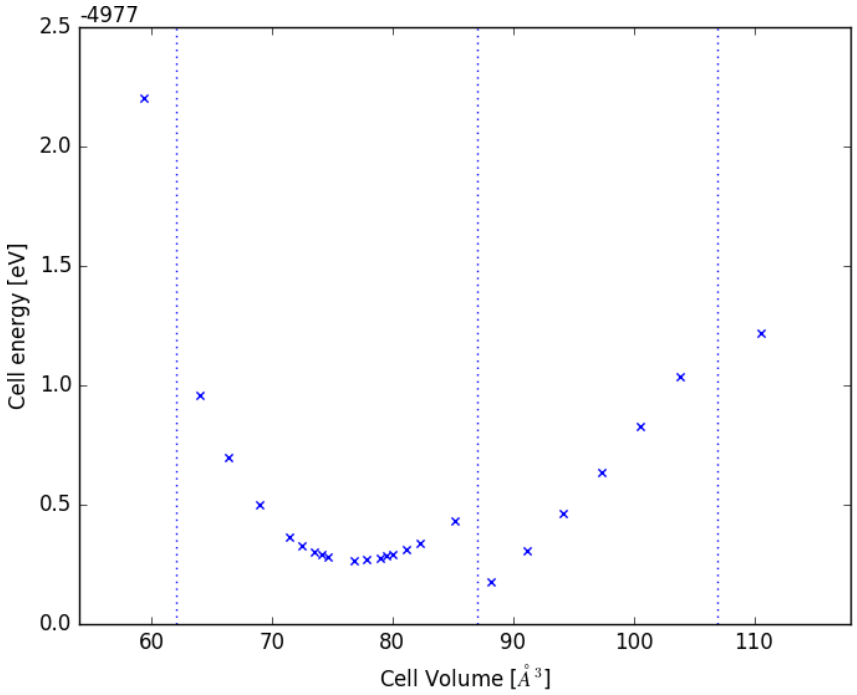


Figure 2.4: Discontinuities in the energy-volume curve of bulk fcc-phase KI due to a changing psinc grid. The psinc grids here are $N \times N \times N$, where the dotted vertical lines separate the four regions where (left-to-right) $N = 81, 91, 99, 105$.

# Chapter 3

# Atomistic Modelling

While *ab initio* methods remain the most reliable approach to material modelling, particularly in exploratory regimes, significant progress is possible at a fraction of *ab initio*'s computational expense by the use of atomistic modelling. Here the priority is to reproduce molecular[1] behaviour while approximating (or even ignoring) the mechanism behind it. This is especially useful when the potential energy surface (PES) of a system's components is already known to some desired accuracy, and emergent collective behaviour is of interest. Even the trivial hard-sphere potential is capable of exhibiting dendritic growth in a crystal-liquid coexistence region[Cheng et al., 2001], and more advanced models integrating more complex interactions are used to model systems such as phase boundaries, colloids, polymers and biomolecules [Frenkel and Smit, 2001; van Gunsteren et al., 1997].

## 3.1 Force Fields

Force fields aim to treat the energy $E$ of a system as a contribution from components (typically atoms), whose energy $E_i$ follows some predetermined functional form. This function is chosen to simulate some known aspect of physical behaviour, and parameters are commonly fitted to reproduce experimental or quantum-mechanical (QM) data.

While the author knows of no quantitative justification for the transferability of this decomposition of total energy into local contributions in the context of quantum mechanics, in practice localised functional groups emerge, allowing force fields to constitute a staple of condensed matter physics.

[1] In this work we use the term 'molecule' loosely, to mean any collection of interacting atoms or ions, regardless of specific bonding connectivity. In particular, we would freely call a nanostructure consisting of ions encapsulated within a nanotube a 'molecule'.

### 3.1.1 Pair Potentials

The simplest interatomic potentials usually consist of a potential energy term between pairs of interacting particles, such that $E_i = 1/2 \sum_{i \neq j} V_{ij}$, where the factor of $1/2$ corrects for double-counting. Commonly, there is a long-range attractive term (putatively describing Van der Waals, dispersion or similar forces) and a steeper short-range 'Pauli' repulsion. In the Lennard-Jones potential, for example:

$$V_{LJ}(r) = \varepsilon \left[ \left( \frac{r_m}{r} \right)^{12} - 2 \left( \frac{r_m}{r} \right)^{6} \right] \tag{3.1}$$

where $r_m$ is the equilibrium distance between particles and $\varepsilon$ is the depth of the potential well. Values for these parameters can be calculated from a material's lattice constant and cohesive energy [Zhen and Davies, 1983] though, since they serve only to define length and energy scales respectively, behaviour is universal at all scales.

Various modification of this foundational form are common: the Buckingham potential [Buckingham, 1938] replaces the $r^{-12}$ repulsion with one of the form $Ae^{-r/\rho}$, while the Born-Mayer potential [Born and Mayer, 1932; Abrahamson, 1969] chooses $Ae^{(\sigma - r)/\rho}$ and also includes a $B/r^8$ correction. The Morse potential [Morse, 1929], often used in its augmented Morse/Long-range form in spectroscopy for fitting results [Roy et al., 2009], can be written as

$$V_M(r) = \varepsilon(e^{-2a(r-r_m)} - 2e^{-a(r-r_m)}). \tag{3.2}$$

Potentials are usually truncated to some cutoff $r_c$ beyond which $V = 0$; usually a constant shift is then applied for continuity, an integrated correction can also be applied for smoothness.

The deficiencies that these pair-potentials share include the neglect of higher n-body terms such as bond-order[2], and that the potentials — being spherically symmetric — ignore bond angles.

However, the Lennard-Jones potential proves sufficient for the modelling of some mono-atomic gases, and various crystal structures can be modelled with pair-potentials, such as face-centered cubic (fcc), body-centered cubic (bcc) and hexagonal close-packing (hcp) [Parrinello and Rahman, 1980].

[2]Bond-order was originally defined as the number of electrons involved in bonding (diatomic nitrogen would have a bond of order 3, that of diatomic fluorine would be of order 1) and was extended by Pauling [1947] to a continuous measure based on bond-lengths. Various measures now exist, including *ab inito* measures related to the population analyses of §3.2 (described therein).

### 3.1.2 Higher-order Potentials

To be able to simulate more intricate systems, models are often bolstered with additional physics. This often requires a dependence on the angles between atoms; as a simple example the Van der Waals interaction between three atoms $i, j$ and $k$ described by Axilrod and Teller [1943] takes the form

$$V_{AT} = E_0 \frac{1 + 3\cos(\theta_i)\cos(\theta_j)\cos(\theta_k)}{(r_{ij} r_{jk} r_{ki})^3}, \tag{3.3}$$

where the coefficient $E_0$ is a constant, $r_{ij} = \mathbf{r}_{ij}/\hat{\mathbf{r}}_{ij}$ is the separation of $i$th and $j$th atoms, and the angle $\theta_i$ is subtended by the vectors $\mathbf{r}_{ij}$ and $\mathbf{r}_{ik}$.

To include the effects of the chemical environment on the strength of chemical bonds between atoms $i$ and $j$, the attractive term of the potential can be modified by the neighbours $k$. For example, the version of the Tersoff potential introduced in the seminal paper [Tersoff, 1986] is of the form:

$$V_T = f_c(r_{ij}) \left[ f_R(r_{ij}) + b_{ij} f_A(r_{ij}) \right] \tag{3.4}$$

where $f_c$ is a sinusoidal cutoff, $f_A$ and $f_R$ are exponential attractive and repulsive functions respectively, and $b_{ij}$ is a term representing bonding, dependant on the local environment. An improved potential was introduced in 1988 [Tersoff, 1988a,b] to better describe elastic properties, the full version of which includes a parameter $\lambda_3$ to control a term $(r_{ij} - r_{ik})^3$. Tersoff finds that setting this $\lambda_3$ to zero does not greatly change the results obtained, while significantly simplifying the potential to:

$$b_{ij} = \left(1 + \beta^n \zeta_{ij}^n\right)^{-1/2n} \tag{3.5}$$

$$\zeta_{ij} = \sum_{k \neq i,j} f_c(r_{ik}) \left(1 + c^2/d^2 - c^2 / \left[d^2 + (h - \cos(\theta_{ijk}))\right]\right) \tag{3.6}$$

where $\beta, c, d$ and $h$ are all parameters to be fitted, generally by regression to reproduce experimental or simulation data. More parameterisation is required to tune the length-scales of $f_A, f_R$ and $f_c$ as well as the amplitudes of $f_A$ and $f_R$. In the full version of the potential the $\lambda_3$ parameter features in $\zeta_{ij}$ and also in a prefactor term to $f_R$.

This significant increase in the complexity of the potential produces far richer results: beyond simple cubic, fcc and bcc, the Tersoff potential can also simulate dimeric, graphitic and diamond forms of carbon as well as its liquid and amorphous phases, and is extensible to silicon and germanium [Tersoff, 1989].

Multi-species interactions can be included by having a parameter-set for each species pairing (i.e. one parameter set for C-C bonds, another for C-Si bonds, a third set for Si-Si bonds). Mixing rules can be used to generate coefficients of mixed-species interaction from single-species parameter sets (e.g. a C-Si interaction generated from C-C and Si-Si parameter sets), though this does not generalise well to the case where bonding types are dissimilar [Billeter et al., 2006]. Alternatively, multi-species interactions can be included by an explicit addition to the potential, such as that of Brenner [1990] for hydrocarbons.

Continuing this theme of manually adding more partial energy contributions to force-fields, ReaxFF [van Duin et al., 2001] consists of energy contributions from the bond-order (obtained directly from the distance to neighbours), over- and under-coordination, valence angle, torsion angle, conjugation, Van der Waals interactions, and Coulombic interactions. In total, 93 parameters are required for a ReaxFF model of hydrocarbon systems, and many parameter sets are available for different materials. This comprehensive consideration of physical interactions — and lack of additional constraints such as fixed connectivity — make ReaxFF transferable to many phases and materials, including oxides, metals and biomolecules [Senftle et al., 2016]. However, while these quite substantial parameter sets are powerful tools for interpolation, their large size arguably leads to overparameterisation, and the parameter sets are not in general as transferable as the model itself.

## 3.2 Coulombic Interactions

Forcefields are often subject to cutoffs around the contributing fragment of interest, such that only the local neighbourhood affects the fragment's energy. This greatly reduces the computational cost, and allows tractable scaling of system size. At the same time, such cutoffs ignore long-distance interactions which can have significant effects in larger systems. The most obvious such interaction is the Coulombic, since its $1/r$ behaviour converges slowly compared to other interactions such as electric multipoles ($1/r^2$ behaviour for dipoles, $1/r^3$ for quadrupoles). Indeed, in the general case of a charged system periodic in 3 dimensions it fails to converge at all, since the number of interacting ions increases with $r^2$. For systems with charged particles, inclusion of the Coulombic interaction is crucial; this is commonly achieved by attributing point-charges at the centre of fragments (called net atomic charges (NACs)), and adding the Coulombic energy of such a system of point charges to the short-range interactions calculated as though for neutral particles. While the addition of multipoles is often required, and even short-range behaviour should

properly depend on particle charge, this somewhat artificial decomposition of energy into long- and short-range components is often successful [Hansen et al., 2012].

These net atomic charges can be assigned in a variety of ways. The simplest is by assigning 'formal charge', calculated as $FC = V - N - B/2$ where $V$ is the number of valence electrons of the neutral atom, $N$ the non-bonded electrons in the atom in the system, and $B$ the number of electrons in bonds with other atoms, and all of $FC, V, N, B$ are integral. More precise static charges can be assigned by considering the relative electronegativity of atoms [Pauling, 1932], for example via electronegativity equalisation [Ferreira, 1963].

In real systems charge-transfer plays a significant rôle, and a reactive model must allow dynamic NACs. The charge equilibration method (QEq) introduced by Rappe and Goddard [1991] can be used to predict charge distributions from experimental atomic ionisation potentials, electron affinities and atomic radii. Alternatively, there are many ways of assigning charges to molecular fragments from a continuous electron-density field. Some, such as the Mulliken [1955] and Hirshfeld [1977] methods, involve projecting the electron density onto some pre-chosen basis. Others partition the charge based on some feature of the electron density, such the Bader method [1994] which partitions by minima. Still others, such as DDEC [Manz and Sholl, 2010], choose the assignment to best reproduce the electrostatic potential. All these methods are well-suited to use in *ab initio* approaches, where density fields and electrostatic potentials are easily accessible. We discuss the machine-learning of these charge-assignment schemes in Chapter 6.

### 3.2.1 Mulliken Population Analysis

Mulliken population analysis [Mulliken, 1955] consists of breaking down molecular orbits (MOs) into a linear combination of atomic orbitals (AOs)[3]. For example, a diatomic molecule with normalised MO $\phi$ can be written as a linear combination of normalised AOs $\chi_r$ and $\chi_s$ of the two respective atoms $k$ and $l$, such that $\phi = c_r\chi_r + c_s\chi_s$. The population of $N$ electrons can then be divided as:

$$N = N{c_r}^2 + 2Nc_rc_sS_{rs} + N{c_s}^2 \tag{3.7}$$

where $S_{rs}$ is the overlap integral $\int_\infty \chi_r\chi_s dv$, so that $N{c_r}^2$ and $N{c_s}^2$ can be identified as net atomic populations and $2Nc_rc_sS_{rs}$ as the overlap population (sometimes used as a measure of bond-order [Minkin, 1999]). The general case, where $\phi_i =$

[3]In the case of density-functional theory, it is the Kohn-Sham eigenstates which are projected onto atomic orbitals.

$\sum_{r_k} c_{ir_k}\chi_{r_k}$, follows straightforwardly:

$$N(i) = N(i)\sum_{r_k} {c_{ir_k}}^2 + 2N(i)\sum_{l>k} c_{ir_k}c_{is_l}S_{r_k s_l} \tag{3.8}$$

To assign Mulliken charges to atoms, the population of each AO in the decomposition is assigned to the atom at its centre. Overlap populations are assigned half-each to each contributing atom centre, regardless of $c_r$ and $c_s$, since the overlap term is symmetrical in $r$ and $s$. In the diatomic case, atoms $k$ and $l$ have populations:

$$N(k) = N({c_r}^2 + c_r c_s S_{rs}); \quad N(l) = N(c_r c_s S_{rs} + {c_s}^2) \tag{3.9}$$

and in the general case:

$$N(k) = \sum_i N(i)c_{ir_k}(c_{ir_k} + \sum_{l\neq k} c_{is_l}S_{r_k s_l}). \tag{3.10}$$

While conceptually simple, and informative in such matters as electron promotion and bonding/antibonding, Mulliken atomic populations are extremely sensitive to choice of AO and have little quantitative significance [Hirshfeld, 1977].

### 3.2.2 Hirshfeld Population Analysis

The approach taken by Hirshfeld [1977] focuses more on the difference in charge density between the molecule in question and a corresponding 'promolecule' consisting of noninteracting atoms, such that:

$$\rho^{pro}(r) = \sum_i \rho_i^{at}(r) \tag{3.11}$$

where the $\rho_i^{at}$ are "suitable positioned, spherically averaged ground-state atomic densities".

To assign charge to atoms, first a sharing function is defined:

$$w_i(r) = \rho_i^{at}(r)/\rho^{pro}(r) \tag{3.12}$$

such that $\sum_i w_i = 1$ everywhere. The actual molecular density $\rho^{mol}$ is then shared out to bonded-atom distributions as:

$$\rho_i^{b.a.}(r) = w_i(r)\rho^{mol}(r). \tag{3.13}$$

The net atomic charge is given by $q_i = Q_i + Z_i$ where $Z_i$ is the nuclear

charge and total electronic charge $Q_i = -\int \rho_i^{b.a.}(r)dv$. For convenience the atomic deformation charge $\delta\rho_i(r) = \rho_i^{b.a.}(r) - \rho_i^{at}(r)$ can be integrated directly, so that (assuming an overall-neutral system) $q_i = -\int \delta\rho_i(r)dv$.

While superior to Mulliken charges, Hirshfeld charges are subject to overestimation of deformation charge, especially in the cases of small atoms [Saha et al., 2009], and to underestimate atomic charge magnitudes due to optimising the distributions to resemble neutral atoms [Manz and Sholl, 2010].

### 3.2.3 Bader Charges

Bader analysis [Bader, 1994] consists of dividing charge into Bader volumes, each with a single charge-density maximum and bordered by surfaces of minimum charge-density normal to the surface. In most physical systems, these maxima correspond to atomic centres, though there exist physical non-nuclear attractors in certain systems [Madsen et al., 1999]. The total charge contained within a Bader volume is the Bader charge, usually assigned to a point centred at the atom nearest the Bader volume's maximum. Distance from the maximum to the atom can indicate polarisation, in which case the Bader volume can be decomposed into multipoles, see §3.2.5.

In practice, the electron density is usually stored as a grid. The points of this grid can then be assigned to local maxima (and therefore to Bader volumes) via a simple steepest-ascent of the charge density, with corrections for lattice bias [Tang et al., 2009]. We discuss the implementation of this analysis to *ab inito* data in Section 6.1.1.

### 3.2.4 DDEC Charges

The Density-Derived Electrostatic and Chemical (DDEC) charges of Manz and Sholl [2010] aim to simultaneously reproduce the electrostatic potential (ESP) both inside and outside the modelled material, and to yield well-defined NACs which resemble those in isolated atoms in appropriate reference states. This latter condition is non-trivial since in systems with 'buried' atoms (those whose Van de Waals surface lies within that of the system as a whole) many combinations of buried charges (NACs assigned to buried atoms) can give similar ESPs.

The total ESP $V(\mathbf{r})$ is written as a sum of atomic ESPs $V_A(\mathbf{r_A})$ of atoms $A$, where

$$V_A(\mathbf{r_A}) = \frac{z_A}{r_A} - \oint \frac{\rho_A(\mathbf{r'}_A)}{|\mathbf{r}_A - \mathbf{r'}_A|}\, \mathrm{d}^3\, \mathbf{r'}_A = \frac{q_A}{r_A} + B + C \tag{3.14}$$

and $z_A$ is the nuclear charge of atom $A$, $\rho_A$ is its non-negative electron density, $q_A$ is its NAC, B is the term due to its atomic multipoles (AMs) and C is due

to penetration of $\rho_A$ which is negligible beyond a certain $r_A$. $B$ and $C$ are then implicitly functionals of $\rho_A$.

Multipolar contributions ($B$ in Equation (3.14)) are minimised when the $\rho_A$ are as spherical as possible, and so following Manz and Sholl [2010] we define an information metric

$$F_{\mathrm{ESP}} = \sum_A \oint \rho_A(\mathbf{r}_A) \ln \left( \frac{\rho_A(\mathbf{r}_A)}{\rho_A^{\mathrm{avg}}(r_A)} \right) \mathrm{d}^3 \mathbf{r}_A \tag{3.15}$$

where $\rho_A^{\mathrm{avg}}$ is the spherical average of $\rho_A$, and so minimising $F_{ESP}$ minimises $B$.

$\rho_A$ should also approximately equal the non-interacting reference density $\rho_A^{\mathrm{ref}}(r_A, n_A)$ with the same number of electrons $n$, determined by linear interpolation of reference densities (from for example DFT) with the closest lower ($\tau$) and higher ($\tau + 1$) number of electrons (i.e. $n_A = \tau + f$, $0 \leq f \leq 1$).

$$\rho_A^{\mathrm{ref}}(r_A, n_A) = (1 - f)\rho_A^{\tau}(r_A) + f\rho_A^{\tau+1}(r_A) \tag{3.16}$$

To this end a distance metric $F_{\mathrm{chem}}$ is defined:

$$F_{\mathrm{chem}} = \sum_A \oint \rho_A(\mathbf{r}_A) \ln \left( \frac{\rho_A(\mathbf{r}_A)}{\rho_A^{\mathrm{ref}}(r_A, n_A)} \right) \mathrm{d}^3 \mathbf{r}_A. \tag{3.17}$$

The assignment of DDEC charges consists of the iterative minimisation of a function

$$G = \chi F_{\mathrm{chem}} + (1 - \chi) F_{\mathrm{ESP}} + \int_\Omega \lambda(\mathbf{r}) \Theta(\mathbf{r}) \, \mathrm{d}^3 \mathbf{r} \tag{3.18}$$

with respect to the $\rho_A$, where $\lambda$ is a Lagrange multiplier to enforce $\Theta(\mathbf{r}) = \rho(\mathbf{r}) - \sum_A \rho_A(\mathbf{r}_A) = 0$ and $\Omega$ is the unit cell. $\chi$ is small ($0.01 \leq \chi \leq 0.4$) so that $F_{\mathrm{chem}}$ only becomes important in shallow landscapes, such as in the presence of buried atoms.

In the improved DDEC3 implementation [Manz and Sholl, 2012], new 'conditioned reference densities' $Y_A^{\mathrm{avg}}(r_A)$ are introduced to replace the reference densities $\rho_A^{\mathrm{ref}}(r_A, n_A)$, defined as

$$Y_A^{\mathrm{avg}}(r_A) = \rho_A^{\mathrm{ref}}(r_A, n_A) \left\langle \rho(\mathbf{r}) / \rho^{\mathrm{ref}}(\mathbf{r}) \right\rangle_{r_A}. \tag{3.19}$$

Manz and Sholl show that by using these smoothed densities the deviation of the reproduced ESP is system-independently minimised when $\chi = 3/14$.

### 3.2.5 Polarisation

In cases of an asymmetrical $\rho_A$, dipoles or even higher-order moments should properly be considered. These can be obtained by for example the method of Kosov and Popelier [2000] of projection onto renormalised spherical harmonics, which they show leads to rapid convergence to the exact *ab initio* ESP. While multipoles are non-trivial to implement in point-like force-field systems, there are common ways to implement dipoles and polarisability. Methods such as the Drude induced dipole model (see for example Lamoureux and Roux [2003]) and the adiabatic core-shell model of Mitchell and Fincham [1993], use satellite charged particles attached by a harmonic spring of spring constant $k$ to create an ion polarisability $\alpha = q_{\text{shell}}^2/k$, where $q_{\text{ion}} = q_{\text{core}} + q_{\text{shell}}$. However, fixed effective atomic partial charges are often used without explicit polarisation effects to successfully model molecular systems, though the magnitude of particular atomic partial charges may need to be adjusted to account for the system's average induction (see Lamoureux and Roux [2003] and references therein). For representing individual, non-averaged systems this adjustment is not necessary since the induction is already represented in the electron density field.

## 3.3 Machine-learned Potentials

Rather than attempting to predict the behaviour of a potential, and then to fit some chosen functional form to data, a more general approach can be taken. In the Machine Learning (ML) approach, the problem of calculating system properties is framed as one of statistical interpolation from training data calculated by other reliable means, such as *ab initio* methods (see for example Alpaydin [2010]; MacKay [2003]; Behler and Parrinello [2007]; Behler [2011]; Bartók et al. [2010]; Manzhos et al. [2014]; Rupp et al. [2012]).

While chemical intuition can be harnessed as a framework for ML, as with the protein force-field QCTFF of Popelier [2015], it is possible to rely only on the most general assumptions of an atom's environment. Such mathematical, 'non-physical' potentials (in the sense that modelled physical interactions do not form the conceptual basis of the potential, not that the potentials produce unphysical results) have the advantage of being free from bias and agnostic to details such as bonding and metallicity, at the expense of requiring more data to reveal the underlying PES. There is also far less justification for extrapolation, and so a measure of the expected uncertainty is crucial.

In our case, we wish to machine-learn some function which reproduces the

outputs of an *ab initio* code from a high-level description of the system, typically the positions of the nuclei. There are multiple approaches to this problem, we will limit discussion to artificial neural networks and Gaussian process regression, before addressing the importance and challenges of system representation.

### 3.3.1 Feed-Forward Neural Networks

A growing body of research centers around artificial neural networks (NN). NNs have been adopted as useful tools to detect complex patterns in data analysis, famously in pattern recognition and classification, and are seeing increasing use in various areas of chemistry and physics [Behler, 2011; Manzhos et al., 2014].

In its most general form [See for example Alpaydin, 2010], a NN is a mapping from some input vector $\mathbf{G} = \{G_i\}$ to an output $E$ (chosen here to be scalar, though a vector in general), via intermediate vectors $\mathbf{y}^l$ called 'layers' (hence the alternative name 'multilayer perceptron'), as shown in Figure 3.1. All non-input, non-output layers are termed 'hidden layers', since their values are not discernable from the output $E$. Each element $y_i^l$ (node or neuron $i$) of each non-input vector $\mathbf{y}^l$ (layer $l$) is calculated from those of the previous layer $l-1$ via:

$$y_i^l = f\left(b_i^l + \sum_j a_{ij}^{l-1,l} y_j^{l-1}\right) \tag{3.20}$$

where $b_i^l$ is a parameterised bias and the $a_{ij}^{l-1,l}$ are weights that determine the overall function of the NN. Thus the argument to $f$ is a linear combination of the elements of the preceding layer, with some added bias weight. $f$ is generally a non-linear function, which allows the NN to reproduce non-linear functions.

The fitting of the weights $a_{ij}^{kl}$ and biases $b_i^l$ is the main task of NN training. Their number scales as $LN^2$, where $L$ is the number of layers, each with $N$ nodes (though it is not necessary for all layers to be of the same size), and it is not unusual for a NN to contain thousands of these parameters. The fitting of the weights comprises the minimisation of some loss term, for example

$$L = 1/2T \sum_i^T (E_{i,\mathrm{ref}} - E_{i,\mathrm{NN}})^2 \tag{3.21}$$

where $E_{i,\mathrm{ref}}$ is the reference energy and $E_{i,\mathrm{NN}}$ the NN output of each $i$ of $T$ 'training' systems. Many optimisation algorithms exist, generally variations of iterative gradient-descent approaches. The backpropagation algorithm in particular is a com-

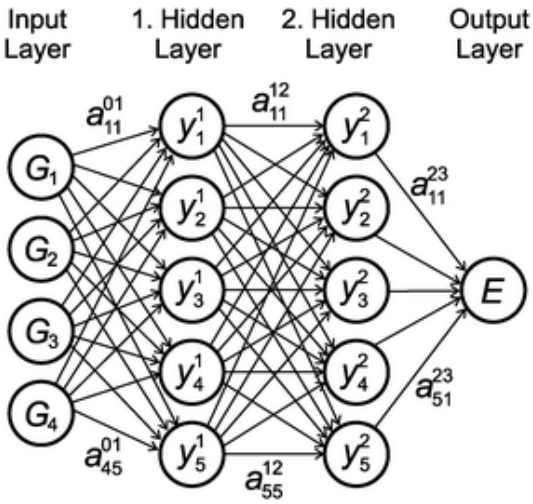


Figure 3.1: An example of a 4-5-5-1 feed-forward neural network defining a functional relation between E and the four-dimensional input $G$. The individual neurons (circles) are arranged in layers, and all neurons in each layer are connected to the neurons in the adjacent layers by weight parameters $a_{ij}^{kl}$ (arrows). For clarity, the bias weights have been omitted. [Reproduced from Behler [2011]]

mon standard [Alpaydin, 2010], but we will not enter into detail here.

The architecture of the NN (that is, the number of layers, and number of nodes in each) is normally considered a hyper-parameter, and in practice is usually optimised empirically by comparing multiple fitted NN [Alpaydin, 2010]. The available training data is partitioned into training- and test-sets for this purpose. A separate validation-set is also frequently created, the mean-squared-error of which is used as an estimate of the variance of the data, giving a single confidence-interval for the entire NN (see for example Behler and Parrinello [2007]).

It has been show that in the limit of layers of infinite size, a NN approaches a Gaussian Process (described in §3.3.2) [Neal, 1996].

### 3.3.2 Gaussian Process Regression

Gaussian Process Regression (GPR) uses statistical inference directly to predict the distribution of possible functions underlying the data [Rasmussen, 2006]. This extends NN's function-agnosticism to its logical conclusion, but the true strength of GPR lies in the straightforward access to the confidence intervals of each individual prediction.

A Gaussian Process (GP) is an extension of the concept of multivariate Gaussian distributions (MVGD) over vectors. Comprehensive descriptions are given in

Alpaydin [2010]; Rasmussen [2006]; MacKay [2003], but we give an overview here. An MVGD is a continuous probability distribution over some vector space which is completely defined by its mean $\boldsymbol{\mu}$ and covariance $\Sigma$, so that the probability density $P(\mathbf{x}|\boldsymbol{\mu}, \Sigma)$ at point $\mathbf{x}$ given some $\boldsymbol{\mu}$ and $\Sigma$ is

$$P(\mathbf{x}|\boldsymbol{\mu}, \Sigma) = |2\pi\Sigma|^{-1/2} \exp\left[-1/2(\mathbf{x}-\boldsymbol{\mu})^T\Sigma^{-1}(\mathbf{x}-\boldsymbol{\mu})\right] \tag{3.22}$$

where the index $T$ indicates a transpose. In general such an MVGD is written as $\mathcal{N}(\boldsymbol{\mu}, \Sigma)$.

By contrast, a GP is a continuous probability distribution over functions $f(\mathbf{x})$ which map $d$-dimensional vectors $\mathbf{x} = \{x_i\}$ to outputs $y$ (here chosen to be scalar). A GP is defined by a mean function $\mu(\mathbf{x})$ (usually chosen to be the zero function, for simplicity) and a covariance function $k(\mathbf{x}, \mathbf{x}')$ (where $\mathbf{x}'$ is some other input vector) which controls the smoothness, stationarity, isotropy and periodicity of the functions in the distribution. Much as a particular MVGD can be written as $\mathcal{N}(\boldsymbol{\mu}, \Sigma)$, a particular GP can be written as $\mathcal{GP}\left(\mu(\mathbf{x}), k(\mathbf{x}, \mathbf{x'})\right)$.

We wish to infer an underlying function $f(\mathbf{x})$ underlying our data (for example a function which maps atomic positions to an energy surface) which we assume is sampled from $\mathcal{GP}\left(\mu(\mathbf{x}), k(\mathbf{x}, \mathbf{x'})\right)$. Our training data consists of a dataset $\mathcal{D} = \{X, \mathbf{y}\}$ of $N$ inputs $X = \{\mathbf{x}_i\}$ and corresponding outputs $\mathbf{y} = \{y_i\}$ , and we assume some noise $\sigma_n$ on our observations so that the output points $y_i$ given $f(\mathbf{x}_i)$ are normally distributed around the value of $f(\mathbf{x}_i)$, that is $y_i|f(\mathbf{x}_i) \sim N\left(f(\mathbf{x}_i), \sigma_n^2\right)$.

$k(\mathbf{x}, \mathbf{x}')$, also called the kernel, can be thought of as a (symmetric) similarity measure between inputs $\mathbf{x}$. Perhaps the simplest kernel is the dot-product kernel $k_{DP}(\mathbf{x}, \mathbf{x}') = \mathbf{x} \cdot \mathbf{x}'$. Another common choice is the squared-exponential kernel $k_{SE}(\mathbf{x}, \mathbf{x}') = \exp\left[-\sum_i \sigma_i^{-2}(x_i - x_i')^2\right]$, where the $\sigma_i$ are parameters which can be tuned to deal with any isotropy in dimensional length-scales. Many other kernels exist, Rasmussen [2006, Chapter 4] goes into more depth.

Assuming that 'new', unmeasured data will be distributed identically to $\mathcal{D} = \{X, \mathbf{y}\}$ (equivalently, that there is some underlying function $f$) and using the fact that a marginal of a joint Gaussian is Gaussian, we can define a distribution over both $\mathcal{D}$ and a new datapoint $\mathbf{x}_*$ and target $f_*$ (distinguished from $y_*$ since there is no error on its measurement):

$$P\left(\begin{bmatrix}\mathbf{y}\\ f_*\end{bmatrix}\right) = \mathcal{N}\left(0, \begin{bmatrix}(k(X,X) + \sigma_n^2\mathbb{I} & k(X, x_*)\\ k(x_*, X) & k(x_*, x_*)\end{bmatrix}\right). \tag{3.23}$$

The rule for conditionals of joint Gaussians states that $P(f_*|x_*, X, \mathbf{y})$ is Gaussian, with mean

$$\bar{f}_* = k(x_*, X)\left(k(x_*, X) + \sigma_n^2 \mathbb{I}\right)^{-1} \mathbf{y} \tag{3.24}$$

and covariance

$$\mathrm{Cov}(f_*) = k(x_*, x_*) - k(x_*, X)\left(k(X, X) + \sigma_n^2 \mathbb{I}\right)^{-1} k(x_*, X). \tag{3.25}$$

For our purposes, we learn some property $y$ of the local environment $\mathbf{x}$, and predict that for some new given environment $\mathbf{x}_*$ the property takes the mean value $f_*$ with uncertainty $\mathrm{Cov}(f_*)$.

### 3.3.3 System Representation

In order to minimise the amount of training data required, the choice of representation of our molecular system is extremely important. Ideally, our representation preserves various symmetries which we know to be preserved in reality, so that training data need not be 'spent' learning them, while at the same time we intend to minimise the bias of functional potentials. In particular, our representation should be invariant to the permutation of identical atoms and to the rotation or translation of a fixed environment.

Clearly a naive list of Cartesian coordinates satisfies neither of these properties, and in addition is inflexible with regards to system size: adding atoms to the system would increase the size of the input vector, and a naive NN approach would require one NN per system size. Behler and Parrinello [2007] surmount this by training one 'subnet' per species, which takes as input some generalised coordinates $\{G_i\}$ and reproduces an atomic energy $E_i$. This is a similar approach to that of the functional potentials of §3.1, though while the generation of the $G_i$ may follow functional forms (Behler and Parrinello for example take radial Gaussian functions of various widths, and cosine terms for triplets), the prediction of atomic energies from the $G_i$ has no such bias.

Bartók et al. [2013] have undertaken an review of such invariant descriptors, including the bond-order parameters of Steinhardt et al. [1983], the descriptor suggested by Behler and Parrinello [2007], the Coulomb matrix approach of Rupp et al. [2012], the power-spectum and bispectrum approaches of Bartók et al. [2010], and introduce their own Smooth Overlap of Atomic Positions (SOAP) approach. They show relations between many of these descriptors. One such relation is that the angular parts of the power-spectum, bispectrum and of the Parrinello-Behler descriptors are all simple polynomials of the canonical set $\sum_{ii'} \cos^m \theta_{ii'}$, which Bartók

et al. use to motivate the creation of a further Angular Fourier Series (AFS) descriptor, $\text{AFS}_{n,l} = \sum_{i,j} g_n(r_i) g_n(r_j) \cos(l\theta_{ij})$, where $g_n$ are radial functions, to aid in the comparison of these descriptors.

While all these invariant descriptors respect the required symmetries, this is not the only consideration. An incomplete system will assign the same descriptor to different structures, and the 'descriptor distance' between two systems may also have many local minima, hampering the ability to describe a PES. Bartók et al. [2013] compare various descriptors by their ability to reconstruct silicon clusters after perturbation, minimising $d_{\text{ref}} = \min_P ||\Sigma - P\Sigma' P^T||$, where $\Sigma_{ij} = \mathbf{r}_i \cdot \mathbf{r}_j$ and $P$ is a permutation matrix. They also generate silicon interatomic potentials using the Gaussian Approximation Potential (GAP) framework [Bartók et al., 2010]. Both tests support the superior performance of SOAP compared to power-spectum, bispectrum, and AFS approaches.

### 3.3.4 Descriptors of Neighbourhoods

Many descriptors begin with the definition of an atomic neighbourhood density:

$$\rho(\mathbf{r}) = \sum_i w_{Z_i} \delta(\mathbf{r} - \mathbf{r_i}) \tag{3.26}$$

where the sum runs over the atomic neighbours $i$ within some cutoff radius $r_c$, $w_{Z_i}$ is some species-dependent weight, and $\delta$ is either the usual delta-function or, in the case of the SOAP descriptor, a Gaussian of finite width centred at $r_i$.

The angular part can then be expanded in terms of spherical harmonics $Y_{lm}$

$$\rho(\hat{\mathbf{r}}) = \sum_{l=0}^{\infty} \sum_{m=-l}^{l} c_{lm} Y_{lm}(\hat{\mathbf{r}}) \tag{3.27}$$

where $\hat{\mathbf{r}} = \mathbf{r}/r$ ($r$ being the magnitude of $\mathbf{r}$) and hence radial information is absent ($\rho(\hat{\mathbf{r}})$ can be considered a projection of $\rho(\mathbf{r})$ onto the unit sphere). These $c_{lm}$ are the foundation of the Steinhardt bond-order parameters [Steinhardt et al., 1983]. In practice the expansion can be truncated at some $l_{max}$, neglecting unphysical rapidly-varying modes. The rotational power spectum $p_l \equiv \mathbf{c_l}^\dagger \mathbf{c_l}$, where $\mathbf{c_l}$ are the vectors of coefficients $c_{lm}$ for $|m| \leq l$, can be shown to be rotationally invariant. However, since each mode $l$ is independently invariant the power spectum is an incomplete descriptor, in the same manner that phase information is lost for each frequency in the one-dimensional power-spectrum.

The bispectrum of a one-dimensional function $f(x)$ with Fourier transform

$F(\omega)$ is defined as $B(\omega_1, \omega_2) = F(\omega_1)F(\omega_2)F^*(\omega_1 + \omega_2)$, where $F^*$ is the complex conjugate of $F$ [Rao and Dianat, 1990], and so the bispectrum can be used to recouple rotational modes, while retaining a global rotational invariance. Bartók et al. [2010] discuss the extension of the bispectrum to the case of coefficients of SO(3)/SO(4) harmonics, and the use of these bispectra as descriptors.

To include the radial information, radial basis functions $g_n(r)$ may be introduced:

$$\rho(\mathbf{r}) = \sum_n \sum_{l=0}^{\infty} \sum_{m=-l}^{l} c_{nlm} g_n(r) Y_{lm}(\hat{\mathbf{r}}). \tag{3.28}$$

Any complete basis set of $g_n$ will perfectly encode the radial information, but if the $g_n$ are constructed from orthonormalised polynomials of $r$ then the expansion can be truncated at some $n_{max}$, giving a finite vector representation of coefficients $c_{nlm}$ which can be similarly used in power spectum or bispectrum approaches. Bartók et al. [2010] also investigate the projection of $\rho(\mathbf{r})$ onto the surface of a four-dimensional hypersphere (similarly to the Riemann sphere construction), as

$$(\phi, \theta, \theta_0) = \left[\tan^{-1}(y/x), \cos^{-1}(z/r), r/r_0\right] \tag{3.29}$$

where $r_0 > r_{\text{cut}}/\pi$. This surface can be decomposed into four-dimensional spherical harmonics, that is to say an irreducible representation of the group SO(3), specifically Wigner matrices $U^j_{m'm}$ [Khersonskii et al., 1988], as

$$c^j_{m'm} = \langle U^j_{m'm} | \rho \rangle \,. \tag{3.30}$$

The bispectrum of these hyperspherical coefficients is invariant to 4D (and therefore 3D) rotations, while retaining radial information.

### 3.3.5 Smooth Overlap of Atomic Positions

Bartók et al. [2013] introduce the Smooth Overlap of Atomic Positions (SOAP) approach as a method of directly constructing a similarity measure between environments, that can be utilised as a simple dot-product kernel.

The overlap of two atomic environments $\rho$ and $\rho'$ can be defined as

$$S(\rho, \rho') = \int \rho(\mathbf{r}) \rho'(\mathbf{r}) \, \mathrm{d}\mathbf{r}. \tag{3.31}$$

This allows a smooth positive-definite kernel giving the similarity between two en-

vironments as

$$k(\rho, \rho') = \int |S(\rho, \hat{R}\rho')|^2 \, \mathrm{d}\hat{R} = \int \left| \int \rho(\mathbf{r})[\hat{R}\rho'(\mathbf{r})] \, \mathrm{d}\mathbf{r} \right|^2 \mathrm{d}\hat{R} \tag{3.32}$$

where the integration over rotation operator $\hat{R}$ is over all possible rotations. The power of 2 preserves radial information since without it the order of integrations can be interchanged (any arbitrary power $\geq 1$ would suffice). This can be normalised by each environment's self-similarity and the sensitivity then accentuated by raising to some positive integer power[4] $\zeta$:

$$K(\rho, \rho') = \left( \frac{k(\rho, \rho')}{\sqrt{k(\rho, \rho) k(\rho', \rho')}} \right)^{\zeta}. \tag{3.33}$$

Bartók et al. show that the kernel of Equation (3.32) can be expressed as

$$k(\rho, \rho') = \sum_{n,n',l,m,m'} c_{nlm} \left( c'_{nlm'} \right)^* (c_{nlm})^* \, c'_{n'lm'} \tag{3.34}$$

$$= \sum_{n,n',l} p_{nn'l} p'_{nn'l} \tag{3.35}$$

where the $\mathbf{c}$ are the coefficients of Equation (3.28) and $p_{nn'l} \equiv \sum_m c_{nlm} (c_{n'lm})^*$ are the power spectra, with all primed quantities referring to the primed environment.

This allows a descriptor $\mathbf{p}$ to be computed for each environment, such that their dot-product acts as a good machine-learning kernel.

A complication arises in that *ab initio* methods give an energy for a complete system, but we require per-neighbourhood energies. Fortunately, the use of a Gaussian Process allows the inference of an underlying function even when only linear combinations of the function values are available. Given a vector $\mathbf{u}$ of $u$ unobserved atomic energies which combine discretely to give a vector $\mathbf{o}$ of $o < u$ observed system energies, and the $u \times o$ matrix $L$ which describes their relationship such that $\mathbf{o} = L\mathbf{u}$, then the covariance matrices $C_u$ and $C_o$ are related as $C_o = L^T C_u L$.

There is also the issue of degeneracy in the training data, where neighbourhoods are very similar to each other. Bartók et al. use the sparsification procedure of Snelson and Ghahramani [2006] to create a much smaller set of representative points, avoiding the expense of training and predicting with many data points while retaining their spread.

[4]Larger values of $\zeta$ accentuate the difference between different structures, but an excessive sensitivity leads to instability as differences between similar structures are over-exaggerated, especially when the training set is sparse. In practice values of $2 \leq \zeta \leq 16$ give good results.

# Chapter 4

# Modelling Materials Encapsulated in Nanotubes

## 4.1 Literature Survey

Filled nanotubes have been a subject of much research since the discovery of carbon nanotubes (CNTs). CNTs are carbon allotropes consisting of cylindrical nanostructures, often described as 'rolled-up' graphene sheets. The way a graphene sheet is 'wrapped' to form a CNT can be represented by wrapping indices ($n$,$m$), see Figure 4.1, and affects various physical properties (such as band structure, discussed in more depth in Chapter 6).

The discovery of CNTs themselves is commonly attributed to Iijima [1991], though controversy exists [Pujadó, 2012] with Radushkevich and Lukyanovich [1952] having published the first known TEM images of CNTs to little notice. In some of the earliest simulations of CNTs, Mintmire et al. [1992] used LDA DFT to confirm the metallic behaviour of infinite empty nanotubes in the regime predicted by the Brillouin-zone cutting theory of Hamada et al. [1992].

Chai et al. [1991] produced the first fullerene-encapsulated materials: lanthanum in small fullerenes of $60, 70, 74$ and 82 atoms of carbon. Pederson and Broughton [1992] used LDA DFT to predict the capillary filling of hydrogen-capped CNT with HF molecules, and shortly thereafter Ajayan and lijima [1993] successfully experimentally filled CNTs with liquid lead through capillary action. Dujardin et al. [1994] found that wetting behaviour of a given material, intimately related to its capillarity, is critical to determine whether the material will fill the tube without an additional pressure gradient. Carbon nanotubes are not the only such encapsulating material: Han et al. [2004] showed boron nitride nanotubes imbibing potassium

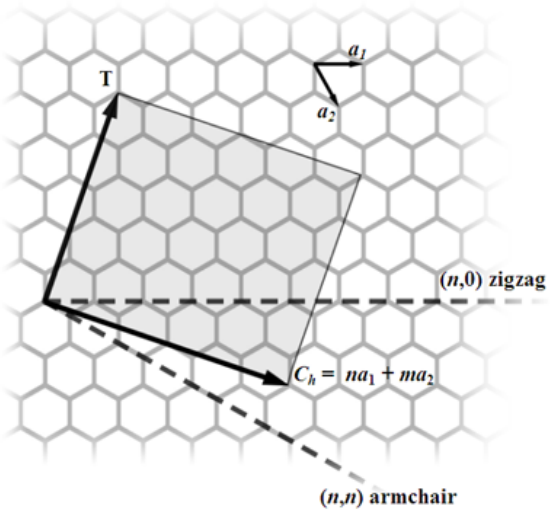


Figure 4.1: An $(n,m)$ nanotube is formed by rolling up an infinite graphene sheet (with real-space unit-vectors $a_1$ and $a_2$) along the vector $C_h = na_1 + ma_2$, such that $C_h$ becomes the circumference of the new tube. $T$ is the tube axis. Tubes are called 'zigzag' when $m = 0$, 'armchair' when $m = n$ and 'chiral' in other cases. (Reproduced from wikimedia.org, public domain)

halides and Golberg et al. [2004] fabricated CNTs already encapsulating nanowires of $MgO_2$. However, carbon nanotubes are the only encapsulating material investigated in this thesis, partly because the large strain energy of inorganic nanotubes leads to their diameter being typically an order of magnitude larger than that of CNTs [Enyashin et al., 2009].

Molecular dynamics simulations of nanotube imbibition have been performed by Enyashin et al. [2009], focussing on $PbI_2$ encapsulated in BN, $MoS_2$ and carbon nanotubes. Their simulations modeled relatively large tubes, with chirality (25,25) corresponding to a radius of 123 Å. This scale allowed the use of effective pair potentials based on the Born-Mayer model with a long-range Coulomb interaction based on static Pauling charges (affording no additional insight into charge-transfer). This level of theory was sufficient to agree with the experimentally-seen imbibition of PbI at 1000 K [Kreizman et al., 2008], providing justification for the macroscopic capillary approach, and also the emergence of a structure of alternating Pb and I shells, similar to the arrangement of PbI shells seen experimentally by Hong et al. [2010], while similar simulations of potassium iodide encapsulated in molybdenum disulfide nanotubes (KI@$MoS_2$) showed no such structure.

Bishop and Wilson [2008, 2009a,b] used a similar MD Born-Mayer approach to find that filling of CNTs with a simplified model salt of 'M-X' ions with formal

($\pm 1$) charges fills the tubes systematically via neutral 'M-X-M-X-$\cdots$' chains. They also found that explicitly modelling the CNT, as opposed to their previous fixed-cylinder work (for example [Wilson, 2007]), can significantly affect the kinetics of formation by changing the activation energies of diffusion pathways.

Encapsulated materials have been shown to take structures unlike those of bulk [Sloan et al., 2002b] and even to take a stochiometry unlike that of bulk [Friedrichs et al., 2005], since coordination is over-ruled by close-packing concerns [Eliseev et al., 2011]. Helical structures have also been seen experimentally [Philp et al., 2003; Sloan et al., 2003] and in simulation [Wilson, 2002; Baldoni et al., 2007], as have double-helix structures [Fujimori et al., 2013].

Yam et al. [2004] used DFT to investigate the absorption spectrum, electron density and band-structure of high-symmetry KI octopoles within (10,10) CNT, but did not relax the structure, nor did they address the unusually high mismatch of 7% between KI and CNT unit cells. They also used only a single $k$-point at the $\Gamma$-point, which was not converged in our equivalent systems. However, they did see significant electron-transfer from iodine ions to the interstitial regions of the CNT and a slight change in its band-structure, though its metallic character was maintained.

Sceats et al. [2006] performed a similar DFT simulation, with more focus on structure relaxation, 4 $k$-points in the irreducible Brillouin-zone and with an explicit gap to manage mismatch. They saw the planes of $K_2I_2$ form rhomboids when relaxed, which was not considered by Yam et al. [2004]. However, they performed only Mulliken charge analysis, which saw negligible charge-transfer in the opposite direction to Yam et al. [2004]. These contradictions call for a more detailed analysis of the system, considering both mismatch and charge-transfer.

## 4.2 Periodic Images

Periodic boundary conditions (PBCs) are often unavoidable in DFT, since they are a result of basis functions in plane-wave DFT, or due to the use of fast Fourier transforms (FFTs) for calculations such as that for the Hartree potential. While PBCs are very useful for bulk materials, allowing the use of physically-sensible unit cells, for the surface (2D) or wire (1D) case they produce spurious periodic images which can have unphysical effects on the simulated material. (One typical artefact is the 'squaring-off' of CNT cross-sections in orthorhombic unit cells.) The common approach to this problem is to increase the unit cell size in the 'non-periodic' directions, adding vacuum 'padding' until some quantity of interest is converged.

There is no common agreement on vacuum gap size in the literature, with values for the same system ranging from a vacuum gap of 16 Å [Brommer and Quigley, 2014] to as little as 5 Å[Yam et al., 2004]. Large vacuum gaps are often effective [Hine et al., 2011], with most values converging within 40 Å. However, the increased cell size comes with associated computational cost and especially for polar materials this quickly restricts the size of practical simulations. This is mitigated to some extent by the need to only use a single $k$-point in the 'non-periodic' directions, since phase-progression in those directions is non-physical. This is not universally taken advantage of (see for example [Senga et al., 2014, Suppl. Inf.]) and such excess $k$-points may in fact mask unconverged separations.

LS-DFT is one possible solution, since vacuum is beyond a certain point 'free', assuming a density-kernel cutoff or similar localisation. However, the long-range Coulombic interaction is not, by default, shielded in any way across periodic boundaries and as discussed in Chapter 3 is slow to converge.

Hine et al. [2011] note that any *a posteriori* approach to correcting the electrostatic energy will fail to correctly reproduce the 'open' case, since the electron-density itself is affected by the PBCs. They examine three approaches that can be applied within SCF calculations, therefore correctly identifying both energy and potential. The Cutoff-Coulomb technique zeroes the Coulombic interaction $(1/|\mathbf{r}-\mathbf{r'}|)$ at $|\mathbf{r}-\mathbf{r'}| < R_{\text{cut}}$ for 3D (such as isolated molecules) [Jarvis et al., 1997], or at more complicated cutoffs for the lower-dimension cases [Rozzi et al., 2006]. The Minimum-Image Convention introduced by Martyna and Tuckerman [1999], with wires addressed by Minary et al. [2004], uses an analytic screening potential which corrects for the interactions of the periodic images. The third approach is the Open Boundary approach [Hine et al., 2011], where the PBCs are removed entirely by recasting electrostatic terms of the Kohn-Sham functional into real-space, including Hartree, core-core and pseudopotential terms. The approximations required to rend this computationally feasible produce significant finite-size errors of their own [Hine et al., 2011].

## 4.3 Cylindrical Potentials

For each encapsulated ion there are typically 10 to 100 carbon atoms in the surrounding CNT. Especially when treating the filling-tube unit-cell mismatch prudently, the number of carbon atoms required to represent an explicit nanotube becomes very large, dominating the expense of any nanowire calculation. The CNT, due to its many covalent bonds, is also typically much stiffer than the encapsulated material,

and as such undergoes much less distortion than the filling. It is natural, then, to seek an approximation to the CNT so that the carbon atoms need not be modelled explicitly. While Bishop and Wilson [2008] see significant kinetic effects resulting from the explicit modelling of carbons, it is not clear that static properties, such as the equilibrium structure, would suffer equally from a static approximation. An extreme example of this approach is seen in the work of Carter et al. [2014], where predicted AgI structures are validated against encapsulation experiments even though the tube is neglected completely, prompting the claim that "the validity of this approach is apparent from the results obtained" . In this work we aim to validate our approaches before trusting their results.

Fujimori et al. [2013] create a smooth cylindrical interaction potential which is applied to encapsulated selenium, fitted to the interaction between an infinite linear chain of Se and an infinite graphene layer. This allows encapsulation without the explicit modelling of carbon atoms, and avoids the issue of mismatch between unit cells of tube and filling, but neglects both charge-transfer and nanotube texture.

## 4.4 Mismatch

When a periodic outer material of relaxed unit-length $a$ is filled with a periodic inner material of unit-length $b$, it is not straight-forward to find the periodicity of the composite material. If $a$ and $b$ were integers, simply finding the lowest-common-multiple length would suffice, such that $na = mb$. However, as $a$ and $b$ are real numbers, without rounding to some rational number there is not necessarily any finite unit-cell for the composite material. Unit cells are very useful for modelling, so it is worthwhile trying to resolve this issue.

Sceats et al. [2006] propose gaps of size $S$ in the inner material, so that $mb + S = na$ (see Figure 4.2). This resolves the issues of length and strain, and they have success in matching the structural parameters of atoms in the centre of their $K_{24}I_{24}$ crystals to those of infinite crystals. However, it is not *a priori* clear how these gaps affect the properties of the composite material as a whole, such as phonons in the longitudinal direction.

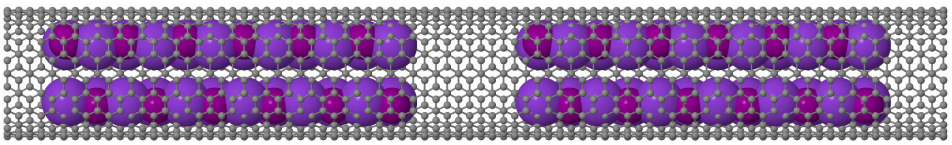

Figure 4.2: 6 KI octopoles inside 21 units of (10-10) CNT with a gap like that of Sceats et al. [2006], showing a single periodic image.

A different, more straightforward, approach is to specify an 'acceptable' amount of mismatch between the inner and outer material, implying a strain in the material. This strain is similar to the case in surface physics, where epitaxial growth forces deformation of the deposited layer, often resulting in Moiré patterns. This 'acceptable' mismatch additionally allows the sacrifice of strain in exchange for a smaller system, where for example a finite common-multiple-length supercell is known but is large. While a naïve choice might find a strain of say 5% acceptable, Lee et al. [2002] find that a strain of 4% in the tube-axis direction can induce an electronic band-structure gap reduction of 60% for SWNT encapsulating $Gd@C_{82}$. Strain values in the literature range from 1% [Brommer and Quigley, 2014] to over 7% [Yam et al., 2004].

For our systems of ionic filling materials in carbon nanotubes (CNTs), the CNT is many times stiffer than the ionic filling due to its structure and many covalent bonds, with a Young's modulus of $\sim$1 TPa[1]. This strain can cause major distortions in the inner material, whose bonds are few and ionic, at high mismatch values, see for example Figure 5.4. Lower values of mismatch relax the composite material towards accepted configurations.

One can consider pressures at which phase-change occurs in similar material in bulk: bulk KI transitions from cubic to face-centred at 1.8 GPa [Piermarini, 1962], bulk CsI transitions from rocksalt structrure to orthorhombic at 45 GPa and at higher pressures to a metallic (115 GPa) and superconducting (180 GPa) phases [Xu et al., 2009], and bulk AgI transitions from hexagonal wurzite-type to cubic halite-type above 0.3 GPa (with many other phases existing in a narrow stability field in the transition region) [Davis and Adams, 1964]. Such pressures occur in a CNT with Young's modulus of 1 TPa at strains of only a few percent; the pressure caused by a 5% strain of a CNT is 50 GPa, above bulk state transition pressures for any of the materials examined here, and even 1% strain creates enough pressure to change the phase of bulk AgI. It seems likely that the vulnerability of nanomaterials to buckling distortions would make them even more pressure-sensitive, and physical properties can vary significantly with pressure even within the same structure, and

[1]The Young's modulus of CNTs can be defined in a variety of ways, either based on the cross-sectional area of the whole tube (in which case care must be taken to specify whether the circumference is interior, exterior or based on the positions of atomic centres) or as $C/t$ where $C$ is the in-plane stiffness of the curved graphene sheet and $t$ is the tube-wall thickness. There is some ambiguity in specifying the thickness of a single atomic layer, and so the equilibrium spacing of graphene layers (0.340 nm) is usually used [Pantano et al., 2004]. Different values can be derived from using elastic parameters of continuum models (see e.g. Yakobson et al. [1996]; Pantano et al. [2004] which give values of up to 5.5 TPa for a wall-thickness of 0.066 nm) but Ãvila and Lacerda [2008] show that projection to a choice of $t = 0.340$ nm invariably brings the Young's modulus to $\sim$1.00(4) TPa with clear chirality and curvature effects.

so a mindful treatment of mismatch is required.

### 4.4.1 Defining Mismatch

The difference in length between our inner and outer material is $na - mb$. However, this value is larger for larger wires, so for example $2a : 4b$ wire would have a larger difference than $1a : 2b$, though their mismatch is in some sense equal. If we normalise the difference by the average length of the composite material, $na + mb/2$, we have a value which ranges from $-2$ at fully-outer:zero-inner to 2 at fully-inner:zero-outer. Removing the numerical factor gives us:

$$\Delta = \frac{na - mb}{na + mb} \tag{4.1}$$

which ranges from $-1$ to 1, where 0 is a perfect match.

A simple way to estimate the significance of a given mismatch is via the strain energy $E_s$ of such a deformation. The one-dimensional nature of the systems reduces the bulk-modulus to a simple spring-constant $k = 2E_s/\Delta L^2$, which can be found by simulating the system around the equilibrium length. For small perturbations a parabola can be fit to the electronic-structure energy.

For two Hookean springs of equilibrium lengths $L_A, L_B$ and spring constants $k_A, k_B$, the strain energy of a deformation to a mutual length $L$ is

$$E_s(L) = \frac{1}{2}\left(k_A(L_A - L)^2 + k_B(L_B - L)^2\right) \tag{4.2}$$

which minimises at an equilibrium length

$$L_{eq} = \frac{k_A L_A + k_B L_B}{k_A + k_B} \tag{4.3}$$

with minimised strain energy

$$E_{s,eq} = \frac{k_A k_B (L_A - L_B)^2}{2(k_A + k_B)}. \tag{4.4}$$

Building the system from $n$ units of CNT (of length $L_C$ and spring-constant $k_C$) and $m$ of XTL (of length $L_X$ and spring-constant $k_X$), and since the spring constant of $n$ springs in series is $k/n$, we have

$$E_{s,eq} = \frac{k_C k_X (nL_C - mL_X)^2}{2(mk_C + nk_X)}. \tag{4.5}$$

Note that minimising $\Delta$ minimises the energy normalised by the combined

length of outer and filling. Other normalisations may be preferable in certain cases, for example if the two unit cells have very different numbers of atoms per unit length, however in our quasi-1D case this is unlikely to occur.

In our case, since the ionic inner is so much softer than the CNT outer, the deformation $\Delta L_X$ of the inner material also deserves special attention:

$$\Delta L_X = \frac{mk_C(mL_X - nL_C)}{mk_C + nk_X}. \tag{4.6}$$

This simple approach assumes the equilibrium length of the filling and CNT are unaffected by the act of filling, and yet successfully predicts the equilibrium length of mismatched systems within the regime of interest. For example, we simulate a 1D KI wire represented by a single KI octopole using the DFT code CASTEP. An energy cutof of 900eV was chosen, which converged the total energy to less than 0.1meV per atom of the value at 700eV. The total energy when 4 k-points lay along the axis (with only a single k-point in the non-periodic directions) agreed with the value at 2 axial k-points to the same tolerance. Norm-conserving pseudopotentials (NCPPs) were used, from the Opium Rappe-Bennett library [Rappe-Bennet pseudopotential library], and the Perdew-Burke-Ernzehof (PBE) [Perdew et al., 1996] exchange-correlation functional was chosen. A vacuum-spacing of 20 Å was used.

We find that the bare KI wire has a unit-length of 6.87 Å and spring-constant of $1.716\,\mathrm{eV\,\AA^{-2}}$. When encapsulated in 2 units of (10,10) CNT, which was simulated similarly to calculate a unit-length 4.93 Å and spring-constant $172.88\,\mathrm{eV\,\AA^{-2}}$, Equation (4.3) predicts an equilibrium length for the composite system of 4.95 Å, remarkably close to the value of 4.96 Å found by relaxing the compound system under DFT simulations, especially considering the significant mismatch of 0.16, which would lead one to expect deviation from the harmonic approximation. For our usual, much smaller values of mismatch we can expect even better results.

### 4.4.2 Finding Acceptable Matches

We can now define a maximum acceptable mismatch, $\Delta_{max}$, such that:

$$\left|\frac{na - mb}{na + mb}\right| < \Delta_{max} \tag{4.7}$$

If we define $\gamma$ such that $m = \gamma n$ then we can solve the inequality:

$$\left(\frac{na - mb}{na + mb}\right)^2 = \left(\frac{a - \gamma b}{a + \gamma b}\right)^2 < \Delta_{max}^2 \tag{4.8}$$

to give us, for a given $a$,$b$ and $\Delta_{max}$, a range of acceptable $\gamma$:

$$\gamma_L = \left(\frac{a}{b}\right)\frac{(1+\Delta_{max}^2)-2\Delta_{max}}{(1-\Delta_{max}^2)} < \gamma < \left(\frac{a}{b}\right)\frac{(1+\Delta_{max}^2)+2\Delta_{max}}{(1-\Delta_{max}^2)} = \gamma_H \qquad (4.9)$$

This also satisfies $\gamma \geq 0$, which is required since $m$ and $n$ are both non-negative.

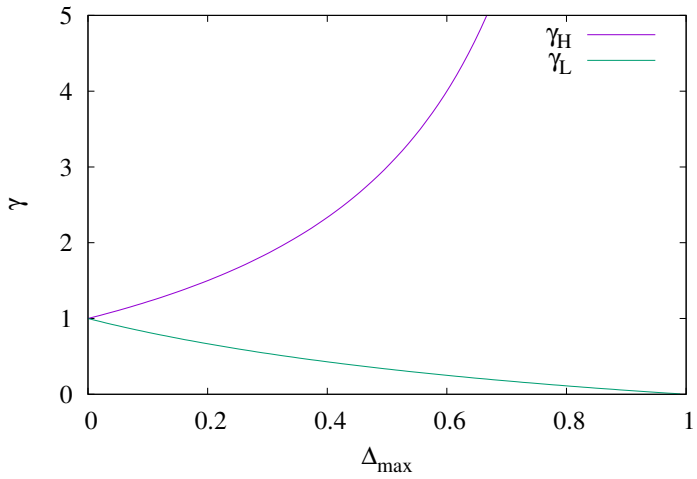


Figure 4.3: Bounds of acceptable values of $\gamma$ in the case that $a/b = 1$.

Any $\gamma$ in the range $(\gamma_L, \gamma_H)$ which satisfies $m = \gamma n$ with $m, n \in \mathbb{Z}$ gives us a valid $n$ and $m$. To find valid values of $m$ given $n$, find $L = \lceil \gamma_L n \rceil$ and $H = \lfloor \gamma_H n \rfloor$. If $L = H$ then $m = L$ gives acceptable mismatch. In fact, all integers $m \in (L, H)$ give an acceptable mismatch with $n$, though $(L, H)$ usually contains 0 or 1 integers at small $n$.

The problem is now to find a minimum $pn + qm$, where $p$ and $q$ are weights For example, $p$ and $q$ might be the number of atoms in a unit cell of the outer and inner materials respectively, or how difficult a particular material is to model. These can be simply found by iterating over $n$ (for $p > q$) or $m$ (for $q > p$), starting at 1. The first pair $(n, m)$ found where $m = \lceil \gamma_L n \rceil \leq \gamma_H n$ minimises $pn + qm$.

### 4.4.3 An Example Case

Consider the example of $2 \times 2 \times 2$ simple-cubic potassium iodide in $10 - 10$ carbon nanotubes (KI@CNT). The relaxed isolated unit lengths are, to the nearest 0.001Å, 6.776Å and 2.467Å respectively. As there are 40 atoms in the $10 - 10$ CNT and only 8 in the KI, it makes sense to iterate CNT unit lengths, and check for the first

occurrence of an acceptable match, given some $\Delta_{max}$. In practice deformations $\Delta L$ and strain energies $E_s$ are more likely to be constrained, in which case progressively smaller mismatches can be examined until all constraints are satisfied.

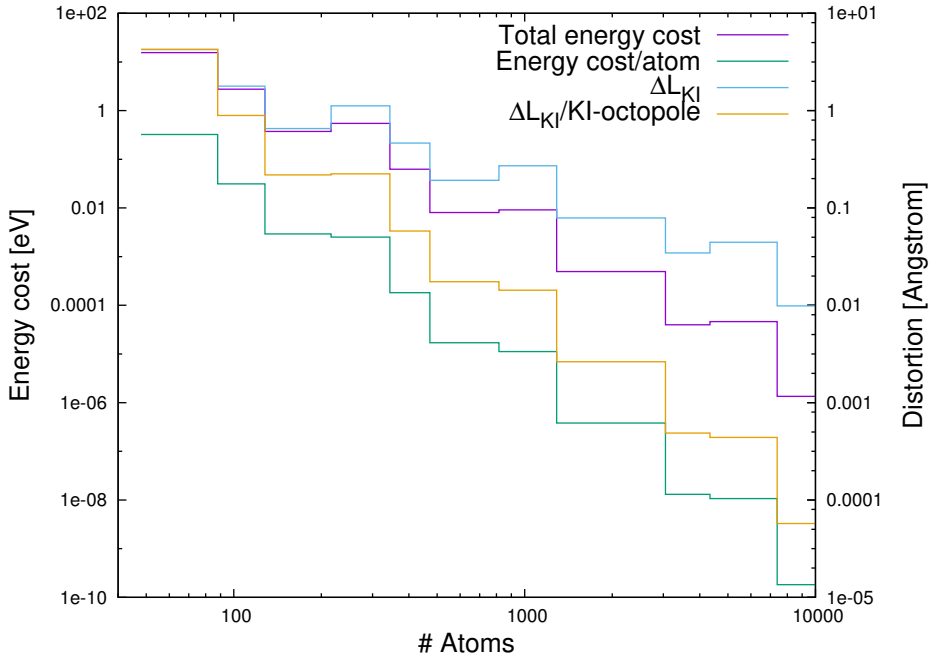


Figure 4.4: Number of atoms required to model $2 \times 2$ rocksalt KI encapsulated in $10 - 10$ CNT with a maximum mismatch. At $1 : 1$ the mismatch is -0.466. Each line indicates the strain energy or crystal deformation of the lowest-$\Delta$ system constructable with at-most the number of atoms on the x-axis.

Restricting $\Delta_{max}$ to $10^{-2}$ requires 11 CNT : 4 KI, a total of 472 atoms (see Figure 4.5a). In this system the CNT is 27.137 Å long, 0.033 Å longer than the enclosed KI. In practice this almost certainly meets our needs, however should we require a tighter match the next smallest mismatch is $< 5 \times 10^{-4}$, requiring 118 CNT unit cells encapsulating 43 KI octopoles with a total of 5064 atoms (see Figure 4.5b).

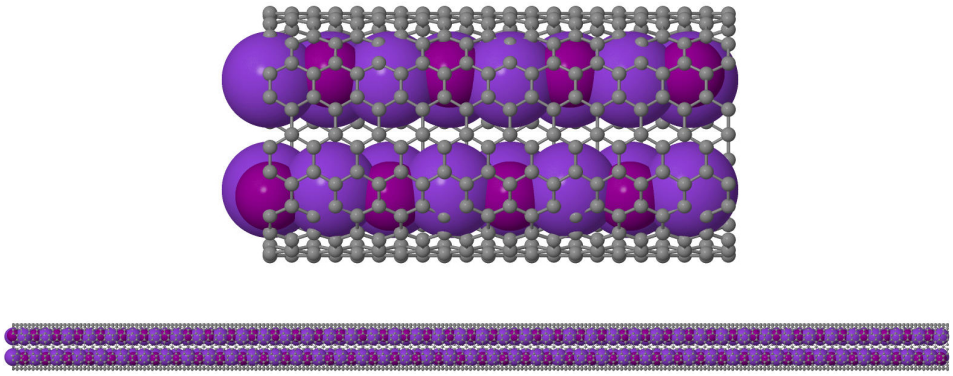

Figure 4.5: Supercell size increases rapidly as $\Delta$ is restricted. Above: 4 KI octopoles inside 11 units of $10-10$ CNT, $\Delta_{max} \approx 6 \times 10^{-4}$. Below: 43 KI octopoles inside 118 units of $10-10$ CNT, $\Delta_{max} \approx 4 \times 10^{-4}$.

# Chapter 5

# Tube Crystal Interaction

## 5.1 Nanotube Texture

In order to assess limits for acceptable mismatch strain energy, we now look at the energy associated with translating the core along the axis of the nanotube. There is a ridged texture to the inside of the tubes, which we will show can resist smooth axial gliding. If the strain energy for some mismatch is greater than the energy associated with this ridging, then we could expect a real system to correct this mismatch via the expansion or contraction of the core along the inside of the tube. Conversely, a real system could be expected to possess mismatch strain-energies less than the ridging energy, giving a physical justification for compound supercells of a given size. Additionally, helical structures have been seen experimentally [Philp et al., 2003] and in simulation [Wilson, 2002; Baldoni et al., 2007], which could conceivably be affected by the chirality of the CNT texture.

We focus our investigation on KI@CNT, since clear experimental results are available, including TEM images [Sloan et al., 2000, 2002a], and the practice of DFT prediction is well-established [Sceats et al., 2008; Yam et al., 2004; Wilson, 2002; Bichoutskaia and Pyper, 2008]. Sloan et al. [2002a] report on $2 \times 2 \times 2$ KI crystals forming within a 1.4 nm SWNT, and $3 \times 3 \times 2$ crystals forming in 1.6 nm SWNTs.

### 5.1.1 Translating 1D chain of KI

To begin, we look at a 1D chain of alternating potassium and iodine atoms, encapsulated within tubes of different radii. The initial system consists of two crystal atoms within two unit-cells of nanotube. The mismatch here is at most 0.23, which is very high, but this was deemed acceptable since the feature of interest is the potential energy-surface of the inside of the tube, rather than the equilibrium structure of the

crystal.

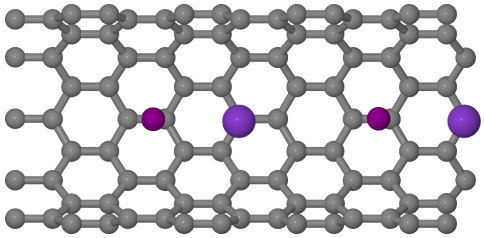

Figure 5.1: 1D chain of KI encapsulated in a CNT. Dimerisation of the chain is caused by mismatch. A manual shift of one atom can cause the dimerisation to swap orientation, i.e. K-I to I-K. Here the shorter K-I distance is 3.25 Å, while the longer is 5.30 Å.

An energy cutoff of 900 eV was chosen, which converged the total energy to less than 0.1 meV per atom of the value at 700 eV. The total energy when 8 k-points lay along the axis (with only a single k-point in the non-periodic directions) agreed with the value at 6 axial k-points to the same tolerance. NCPPs from the Opium Rappe-Bennet library [Rappe-Bennet pseudopotential library] were used, as was the PBE exchange-correlation functional [Perdew et al., 1996].

The starting structures were fully relaxed until the maximum force was below 0.02 eV $\text{Å}^{-1}$. The minimisation method chosen was two-point steepest-descent (TPSD), since this was the only method found for which CASTEP would relax the periodic dimension while keeping the non-periodic directions fixed to provide an inter-image spacing (which was set to 20 Å). The convergence of the self-consistent-field (SCF) calculations was erratic, likely due to charge sloshing. Charge sloshing is a failure mode of DFT on metallic systems, due to quadratic divergence of the dielectric matrix [Kresse and Furthmüller, 1996]. Density mixing is used to stabilise the algorithm in these cases. Linear density mixing introduces a stabilising inertia by mixing the electron density of the last SCF iteration $\rho_{\text{old}}(\mathbf{G})$ into the new density $\rho_{\text{out}}(\mathbf{G})$ such that $\rho_{\text{new}}(\mathbf{G}) = a\rho_{\text{old}}(\mathbf{G}) + (1-a)\rho_{\text{new}}(\mathbf{G})$ where the mixing amplitude $0 \leq a \leq 1$ and $\mathbf{G}$ are reciprocal lattice vectors. More advanced density mixing schemes weight the mixing as a function of $G$-vectors or use densities of more than one past SCF cycle. The Broyden scheme [Kresse and Furthmüller, 1996; Broyden, 1965] was used with a mixing amplitude of 0.5 to achieve fast and reliable convergence.

After the initial full relaxation, the carbon atoms were frozen in place. The potassium ion was then manually shifted along the axis and the iodine atom allowed to move freely along the axis, while being constrained in the off-axis direction to avoid mismatch-induced buckling. The effect on the relaxed position of the free

iodine atom is shown in Figure 5.2, the energy of the system is shown in Figure 5.3.

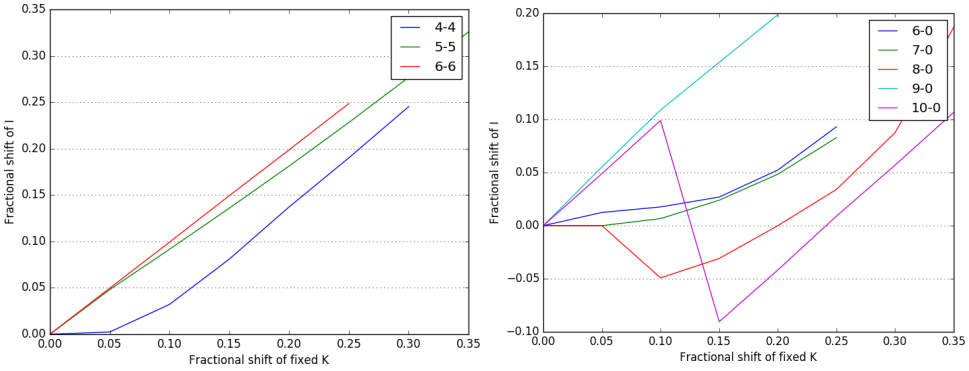


(a) (b)

Figure 5.2: The position of the relaxed iodine atom along the tube after a forced shift of the potassium. Armchair ($n$-$n$) tubes on the left show a clear resistance to free translation at narrower diameters, disappearing at wider diameters. The case for the zig-zag ($n$-0) chiralities is more complicated, but focusing on the areas of positive gradient show the same behaviour as before. Sharp negative gradients are artefacts caused by changing orientation of the dimerisation of the crystal, shown in Figure 5.1.

### 5.1.2 Octopole rotation and translation

By progressing to $2 \times 2 \times 2$ KI octopoles (see Figure 5.4) we can explore the effects of both translation and rotation of the core. We begin with a bare crystal wire consisting of $(KI)_4$ octopoles cut from bulk rocksalt KI. DFT calculations of bulk rocksalt KI converged at a cutoff energy of 900 eV, with a $7 \times 7 \times 7$ k-point grid and using a PBE exchange-correlation functional. This gave a K-I bond-length of 3.7 Å, in close agreement with the experimental value of 3.5 Å [Sirdeshmukh et al., 2010]. The initial KI octopole-wire structure was chosen to have this same 3.7 Å K-I bondlength, and the structure was then relaxed in vacuum, without applied symmetries and in a unit cell of fixed length in the non-periodic direction of 25 Å and with a $1 \times 1 \times 2$ k-point grid, until the maximum force was less than 0.02 eV Å$^{-1}$. The structure relaxes in vacuum with the iodine ions slightly further from the wire axis than the potassium, at 4.95 Å compared to 4.40 Å, see Figure 5.4a.

This structure was translated and rotated along the inside of carbon nanotubes, keeping the axial center-of-mass constant, and the energy of these movements were analysed. The crystal was not allowed to relax at these new positions, resulting in an energy landscape corresponding to adiabatic crystal motion.

This initial structure, of 2 units of vacuum-relaxed $(KI)_4$ encapsulated in 4

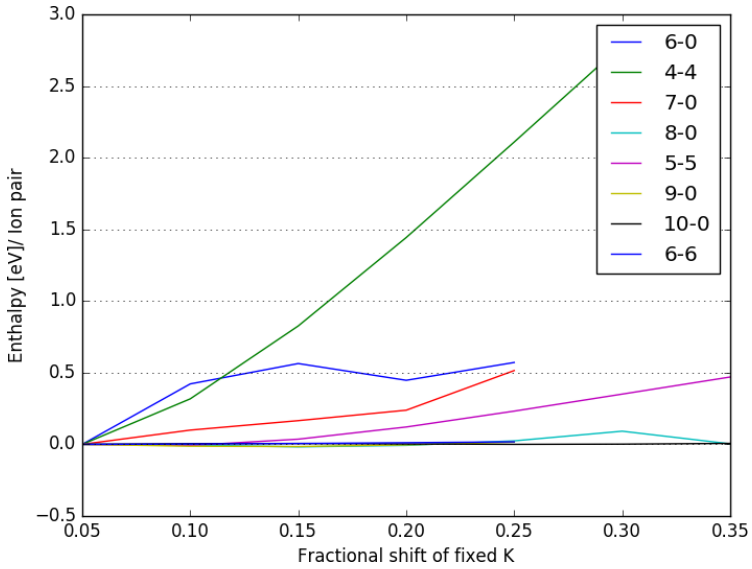


Figure 5.3: The total energy of a system of 1D KI inside a frozen CNT after a forced shift of the potassium and subsequent relaxation of the iodine atom. The CNT chiralities are listed in the key in increasing diameter, from 4.79 Å for the 6-0 tube to 8.14 Å for the 6-6. For tubes larger than 5-5 (6.78 Å) forced translation has a small energy cost, on the order of meV per ion pair. Armchair ($n$-$n$) chiralities are more resistant to translation than zig-zag ($n$-0) tubes of similar diameter.

units of (10-10) CNT, has a high mismatch of $-0.13$. As with the 1D case, mismatch itself should not inherently affect the interaction between tube and filling. However, it will affect the equilibrium structure of the filling. Any mismatch-induced swelling of the filling could be expected to increase the tube-filling interaction.

When relaxed inside the tube until the maximum force on an atom is less than 0.02 eV Å$^{-1}$, before any other motion takes place, it departs significantly from the rock-salt-like wire (Figure 5.4c), and the iodine and potassium ions move much closer to the tube axis, at 3.29 Å and 3.57 Å from the axis respectively. This relaxed structure is much less resistant to internal motion. Figure 5.6a shows that the peak-to-peak energy difference due to rotation of its core is of the order of 0.1 eV per KI octopole. Resistance to reptation is a tenth of that at rotations of 0 or $\pi$, and even less at other rotations.

We now investigate the effect of CNT radius of the potential energy surface. Figures 5.5 and 5.6a make it clear that the vacuum-relaxed filling is a poor approximation to the actual state of the encapsulated filling. Relaxing the filling within the tube makes a significant difference, effective pressure easily causes phase-change of the soft material (see Section 4.4), and so mismatch must be minimised to avoid the distortion seen in Figure 5.4c. We run stress-strain calculations on the vacuum-

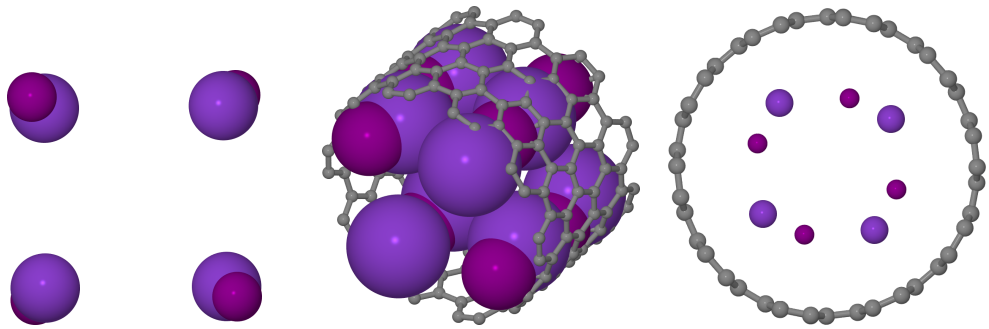

(a) (b) (c)

Figure 5.4: (a) Axial view of an octopole-based KI wire relaxed in vacuum. Potassium ions are 4.40 Å from the axial centre-of-mass, iodine ions are 4.95 Å away. (b) Two $2 \times 2 \times 2$ KI octopoles inside four units of (10-10) CNT. The K-I bonds are of length 6.24 Å, the diameter of the tube is 13.75 Å. (c) The vacuum-relaxed octopole structure after relaxation in two units of (10-10) CNT. There is a four-fold rotational symmetry in the plane, though the top two and bottom two ions are in a different plane to the other four ions, with planes equally spaced along the 4.87 Å unit cell.

relaxed KI-octopole wire and on the CNTs listed in Table 5.1 in their unfilled state. The fortuitous respective cell-lengths produce mismatch values of ∼0.002 for ratios of 2 units of $KI_4$ in 3 units of CNT for the zigzag (n-0) tubes, corresponding to a $\delta L$ of less than 0.03 Å per octopole and a strain-energy of ∼0.01 meV per atom. However, the crystal cores were then relaxed inside the CNT, and the stress-strain calculation was repeated with these tube-relaxed fillings in a vacuum. The same ratios of tube-to-filling now produce a higher mismatch of ∼0.08, leading to a $\delta L$ of 0.9 Å per octopole and a strain-energy of 6 meV per atom. A ratio of 4:3 was required in all zigzag cases to reach tolerances where $\delta L = 0.2$ Å per octopole and

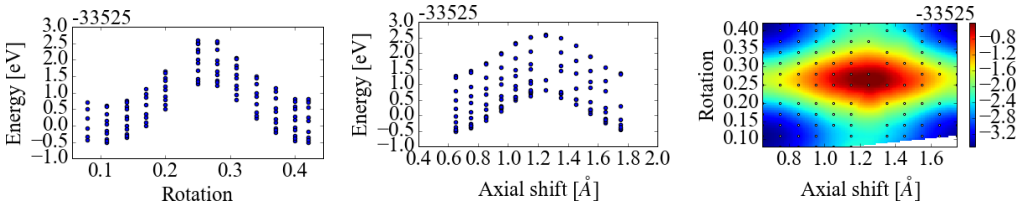


(a) (b) (c)

Figure 5.5: Energy [eV per octopole] of high-mismatch vacuum-relaxed KI octopoles encapsulated in a (10-10) CNT when the core is rotated or translated along the centre of the CNT. Energy differences between maximum and minimum are of the order of 3 eV per KI octopole. Figures (a) and (b) show a projection of the energy surface for multiple core-shifts and rotations respectively. Figure (c) shows a cubically interpolated surface, dots indicate sampling points.

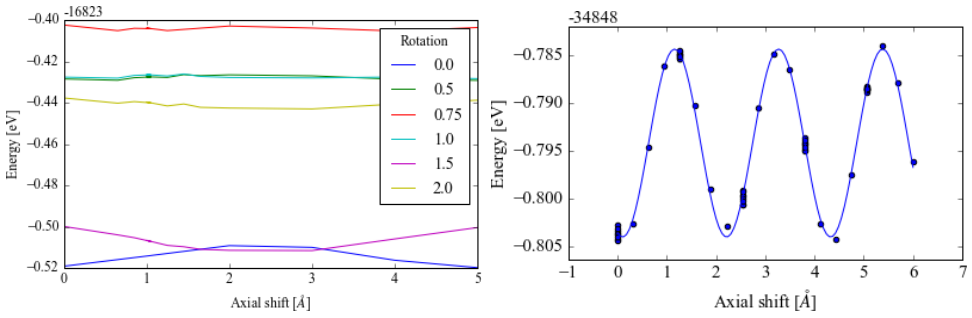


(a) (b)

Figure 5.6: (a) Energy [eV per octopole] of the relaxed high-mismatch $(KI)_4$@(10-10) CNT (shown in Figure 5.4c). Each line represents a particular rotation. (b) Energy of (14-0)-encapsulated tube-relaxed KI octopoles in eV per octopole. Where there are multiple points at a single axial shift these refer to different core rotations. The line corresponds to a sinusoidal fit.

$E_s = 0.4\,\text{eV}$ per atom, whereas a ratio of 5:2 was required for armchair systems.

Referring to Table 5.1, the tube-crystal interaction decreases with increasing CNT radius, as expected, and is almost always weak, though measurable. Except in the tightest tubes or at high mismatch, an unfavourable rotation or translation never costs more than a few meV.

One unexpected result is the ratio of energy cost of translation to rotation. The zigzag (n-0) tubes uniformly resist translation approximately 10 times as strongly as rotation. For example, Figure 5.7a shows the energy with respect to rotation and translation of the core in the case of the (15-0) CNT. Axial shift is much more resisted than rotation, with an well-depth of 2 meV per octopole compared to rotation's 0.5 meV. However, the armchair (n-n) CNTs are in general much more evenly-resistant, with rotation roughly as energetically expensive as translation (see for example Figure 5.7b), and are also more resistant to rotation at the same radius.

### 5.1.3 Validity of rigid-rod approximation

The previous section assumes that treating the filling as a rigid rod is appropriate: that the internal forces of the filling maintain its structure despite the axial or rotational force applied by the tube. We now assess that assumption, by concatenating our previous systems to create a compound system with octopoles at different extrema of the rotational-translational energy landscape, and observing the relaxation of the compound system.

The systems required begin to become quite large, since we must minimise mismatch of each individual extremum-dwelling section of the filling. For this reason

| System | CNT Radius | Rotation | Translation |
|---|---|---|---|
| (10-10) (V,MM) | 13.6 | 1349 | 1910 |
| (10-10) (MM) | 13.6 | 11.7 | 116.6 |
| (8-8) | 10.8 | 92.3 | 88.5 |
| (9-9) | 12.2 | 0.70 | 0.44 |
| (11-11) | 14.9 | 0.59 | 0.30 |
| (13-0) | 10.2 | 2.72 | 332.9 |
| (14-0) | 11.0 | 1.67 | 20.3 |
| (15-0) | 11.8 | 0.43 | 2.53 |
| (17-0) | 13.3 | 0.03 | 0.37 |

Table 5.1: Peak-to-peak energy-differences due to rotation and translation of KI octopoles within a CNT. Radius is in Å, energies are in meV per octopole. Systems labelled (V) refer to those where the KI is relaxed in a vacuum before being transplanted, otherwise the filling is relaxed inside the tube. Systems labelled (MM) have high mismatch, else mismatch between the crystal-structure relaxed inside the tube (with a spring-constant calculated in a vacuum) and the CNT is small enough that $\Delta L < 0.2\,\text{Å}$ per atom and $E_s < 1\,\text{meV}$ per atom.

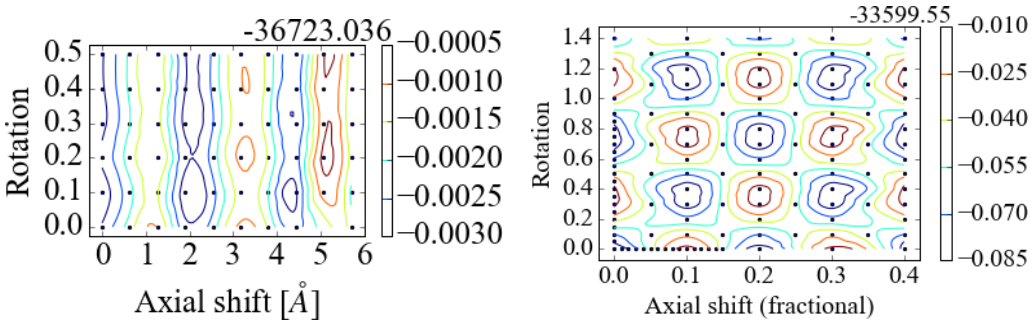


(a) (15-0) (b) (8-8)

Figure 5.7: Energy [eV per octopole] of tube-relaxed KI octopoles encapsulated in (15-0) (left) and (8-8) (right) CNT when rotated or translated. Black dots indicate sampled points, which are cubically interpolated to generate the contour map. The cubic interpolation results in a slight flattening of the landscape compared to a sinusoidal fit.

we transition to the linear-scaling ONETEP code. In order to agree to the CASTEP results to the precision required (converging the peak-to-peak values of Table 5.1 to $\sim$1 meV per octopole) we required 13 NGWFs for each potassium ion (covering the n=3 sp manifold, the n=4 sp manifold and the 4d shell) and 4 NGWFs for each carbon or iodine, covering their outer-layer sp manifold, all with radius 12 $a_0$. The cutoff energy remained at 1000 meV, and the same pseudopotentials and exchange-correlation functional were used. No kernel cutoff was used. Since ONETEP models only the $\Gamma$-point, at least a 2-unit supercell is needed to match the $1 \times 1 \times 2$ k-point grid, however 3 units were chosen for smaller validation calculations to ensure that NGWFs did not self-interact across periodic boundaries.

For the high-mismatch (10-10) case, shown in Figure 5.8, the mismatch completely dominates the behaviour. The octopoles are alternately placed at maxima and alternate minima (see Figures 5.8a and 5.8b), and allowed to relax until the maximum force was less than 0.1 eV Å$^{-1}$. The addition freedom allowed by the supercell is used to find a more favourable helical state, and the effect of rotational position is negligible.

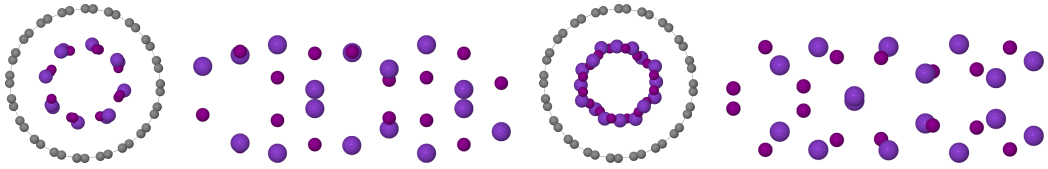

(a) (b) (c) (d)

Figure 5.8: Structures of rotated high-mismatch KI octopoles within (10-10) CNT before (a,b) and after (c,d) relaxation. Carbon is hidden in Figures (b) and (d). Leftmost and rightmost two atoms in (b) belong to the same plane.

Figure 5.9b shows the case of KI octopoles in a (13-0) CNT, with octopoles alternately at maxima and separate minima of the rotational landscape. The octopoles were initially manually placed at the extrema, then allowed to relax until the maximum force was less than 1 eV Å$^{-1}$. The planes of the octopoles begin to rotate, but remain centered around their extrema, while slight zig-zagging occurs to increase inter-ionic distance. It is important to note that the octopole placed at the maximum also remains straddling the maximum. It is likely that inter-ionic forces prevent wholesale rotational shearing of the core, leaving the system in a local energy minimum.

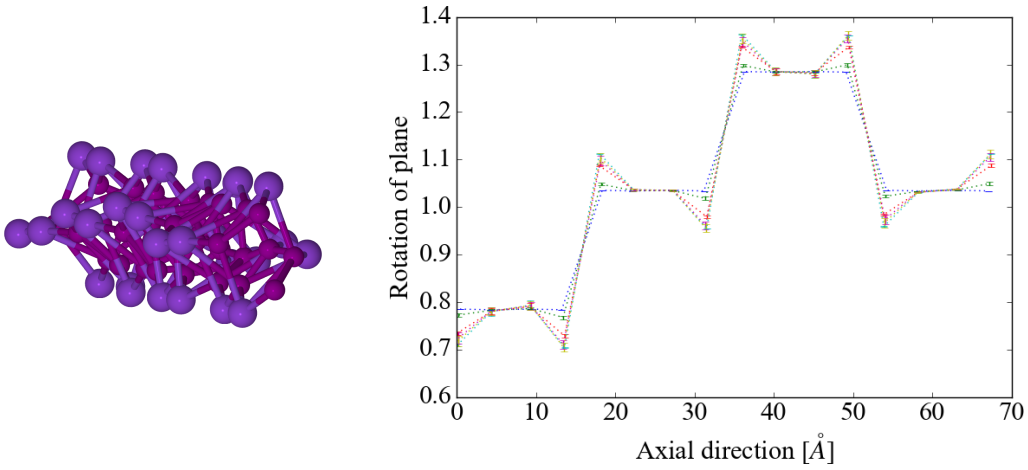


(a) (b)

Figure 5.9: KI octopoles rotated within a (13-0) CNT. (a) Ball-and-stick model, with carbon atoms hidden. (b) Graph of the orientation of KI quadrupolar planes. Planes rotated at ∼0.8 and ∼1.3 are located at rotational minima, those at ∼1.05 are at maxima. The blue, squared-off lines represent the initial structure; green, yellow and red lines show progressively tighter relaxations. Error bars show the deviation of the planes from regular rhomboids.

## 5.2 Stabilisation of Phonon modes inside CNTs

When interested in modelling properties of a material it is common to choose an initial structure based on experiment, and relax the structure within the modelling framework used before calculating the properties of interest. In this section we investigate whether structures suggested by experiment to exist within nanotubes can be simulated *in vacuo* by the application of symmetric constraints, and whether the unphysical instabilities such symmetries entail would be stabilised by the presence of a nanotube.

### 5.2.1 Choice of Structures

Experimental results, such as the high-resolution transmission electron microscopy (HRTEM) images of Sloan et al. [2003] (see Figure 5.10), are excellent touchstones for theory. They suggest promising initial structures for theoretical structure analysis and provide final validation of results.

Based on HRTEM images of CNT-encapsulated AgI by Sloan et al. [2003], two rocksalt structures were chosen. The first, see Figures 5.11a and 5.11d, was a slice of unsheared rocksalt, based on that in Figure 5.10(d). The second, see Figures 5.11b and 5.11e, was this same rocksalt slice but sheared in the periodic

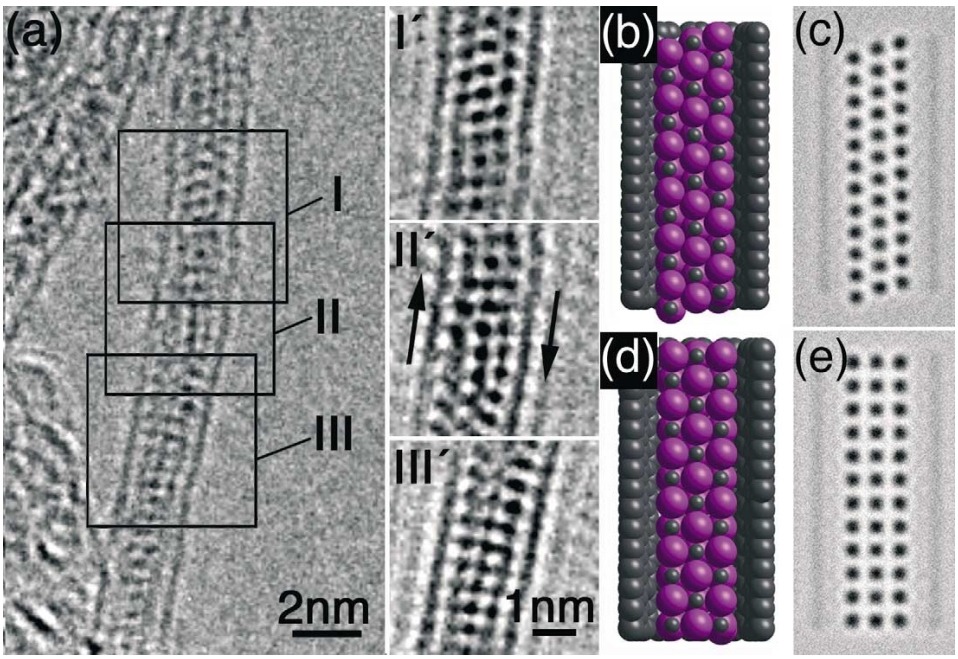


Figure 5.10: HRTEM image of AgI encapsulated within 1.6nm carbon nanotubes. (b) and (d) are models based on the regions I and III respectively, while (c) and (d) are simulated HRTEM images of those models. Reproduced from Sloan et al. [2003].

direction, based on that in Figure 5.10(b). Carter et al. [2014] suggest that shear-inversion behaviour occurs in nanotubes wider than ∼1.4 nm, raising the possibility of reversible phase-change.

Initial Ag-I bonds for the unsheared structure were 3 Å. The sheared structure was sheared linearly, so that the Ag atom on the top plane was nearly above the I atoms on the bottom plane. The slight displacement breaks symmetries that might unintentionally restrict relaxation. More extreme shearing is symmetrically equivalent to a smaller shear with an inversion.

Additionally a third structure was considered, unlike that of any bulk AgI, based on results of Eliseev et al. [2011], see Figures 5.11c and 5.11f. The Ag-I bonds here are 2.35 Å, the width is 4.7 Å and the interplanar distance is 2.78 Å. A similar structure has been posited for encapsulated AgI, AgCl and AgBr [Eliseev et al., 2010], however the stochiometry in this latter work is unclear, and so we examine only the former three structures.

Though HRTEM images show that only 50% of AgI filling is typically predominantly crystalline, with 30% being glassy [Sloan et al., 2002c] and the rest amorphous, we investigate only the crystalling phases in this work.

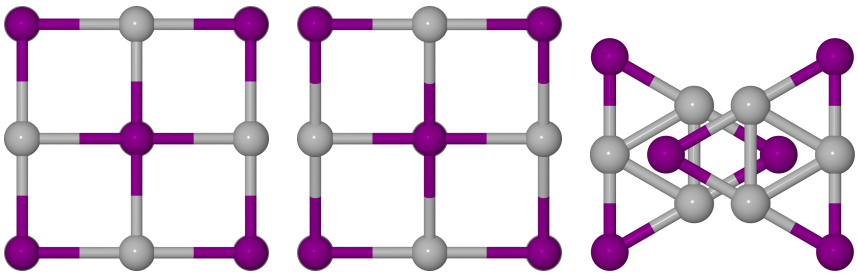

(a) Unsheared, front (b) Sheared, front (c) Eliseev, front

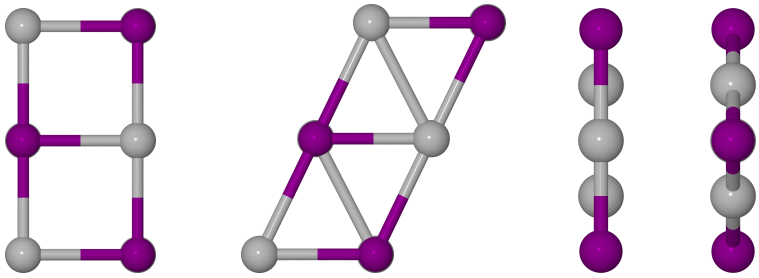

(d) Unsheared, side (e) Sheared, side (f) Eliseev, side

Figure 5.11: Initial unit-cells of chosen structures of AgI wires. The top row shows the structure looking along the periodic direction, the bottom rows shows the side-view.

### 5.2.2 Bare Relaxation

The structures shown in Figure 5.11 were initially relaxed without any applied symmetries, and with a small noise of 0.2 Å applied to prevent the search from being trapped in a quasi-stable state. The minimisation method chosen was again TPSD to allow CASTEP to relax the periodic dimension at fixed inter-image spacing. The two rocksalt systems were considered relaxed when the forces were smaller than $0.02\,\mathrm{eV\,Å^{-1}}$, the weak interplanar interactions of the Eliseev structure required a tighter tolerance of $0.001\,\mathrm{eV\,Å^{-1}}$. This tight force convergence was unachievable with the TPSD minimisation method, and so once the axial stress had reached $5 \times 10^{-4}\,\mathrm{GPa}$ the cell vectors were fixed and the BFGS minimisation method was used to relax the atom positions.

CASTEP also requires the use of norm-conserving pseudopotentials for the perturbative phonon calculations discussed later (in particular we use the norm-conserving special-relativistic PBE pseudopotentials included with CASTEP 9.0 [CASTEP website]), which require a relatively high cutoff energy of 1000 eV to achieve an energy-difference between the unsheared rocksalt and 'Eliseev' structures converged to within 1 meV per atom of the value at 1200 eV. A similarly-converged energy-difference between sheared and unsheared rocksalt structures required 8 k-

points along the periodic direction (with only 1 in each non-periodic direction) and grid-scale of 2 and fine-grid-scale of 2.5.

The resultant relaxed structures are show in Figure 5.12a–f. While the 'Eliseev' structure remains fairly similar to the initial structure, both the rocksalt-inspired have relaxed to a structure which seems unphysical. In particular, the 'interstitial' silver atom in the top-left of Figure 5.12a and bottom-right of Figure 5.12b suggest an alternative structure, with a different stochiometry, would be energetically preferable.

The structures were then relaxed while constrained to remain subject to their initial symmetries, by contraining the forces to act orthogonal to symmetry-breaking lines. This results in systems which are relaxed to metastable states, on saddle-points of the energy-surface. The unsheared rocksalt AgI was subject to the dihedral $D_{4h}$ symmetry, which is to say a 4-fold rotational symmetry with 4 perpendicular 2-fold axes, and a horizontal mirror plane (where the first rotation axis is by convention vertical), which exerts a total of 8 symmetry constraints. The sheared rocksalt AgI (without maximal shear) was subject to the cyclic $C_{2h}$ symmetry, which is a simple 2-fold rotation symmetry with a horizontal mirror plane, giving 4 symmetry constraints. The 'Eliseev' structure was subject to the $D_{2h}$ symmetry, a 2-fold rotational symmetry with 2 perpendicular 2-fold axes and a horizontal mirror plane, which also creates 8 symmetry constraints.

The resultant structures are shown in Figure 5.12g–l. The unsheared rocksalt and 'Eliseev' structure are constrained by these symmetries to resemble their ansatz structures, however the side view of the sheared rocksalt resembles neither the ansatz nor any experimental image.

### 5.2.3 Unstable bare phonons

The symmetries applied to the rocksalt system to produce the systems of Figure 5.12(g–l) are clearly unphysical, and those systems are not stable *in vacuo*. Rather, the manual restriction that atomic positions satisfy the applied symmetries has forced the systems into metastable states, where the atomic forces are zero but the systems lie on saddle-points of the energy surface. However, if we suspect that the systems actually exist within tubes, it would be worthwhile to investigate their unstable phononic modes in order to predict the effect of an encapsulating tube.

We briefly describe the harmonic approximation of lattice dynamics, following Martin [2008], beginning with the Taylor expansion of the total energy at

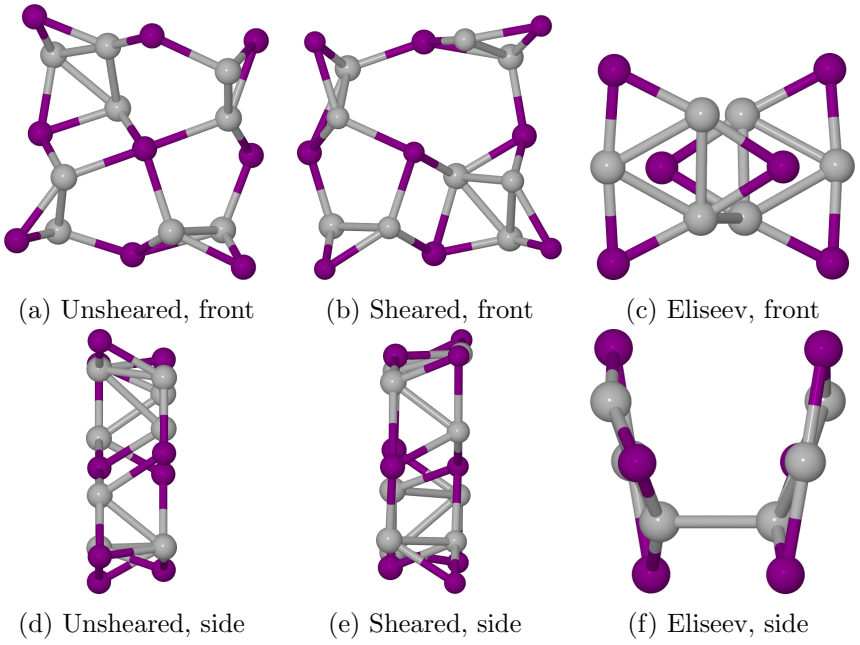

(a) Unsheared, front (b) Sheared, front (c) Eliseev, front

(d) Unsheared, side (e) Sheared, side (f) Eliseev, side

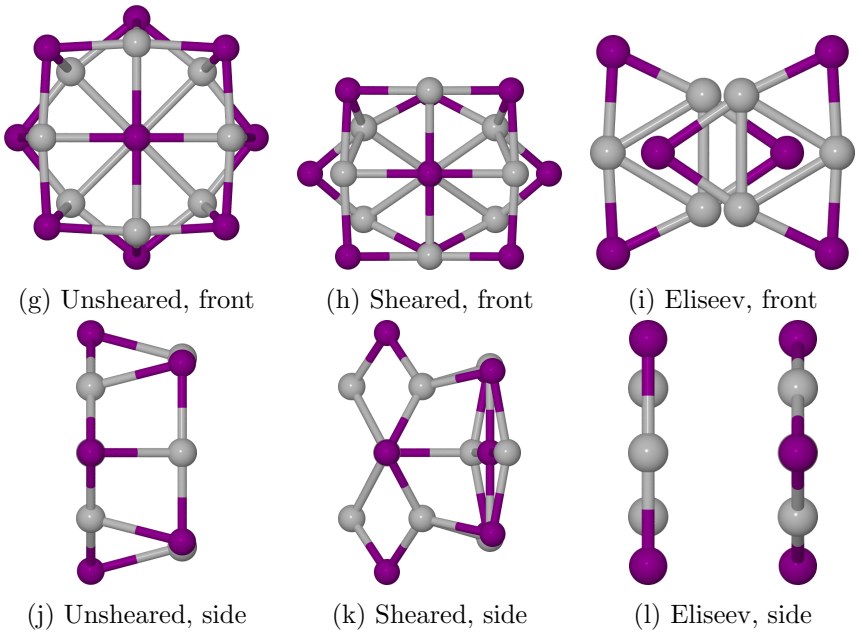

(g) Unsheared, front (h) Sheared, front (i) Eliseev, front

(j) Unsheared, side (k) Sheared, side (l) Eliseev, side

Figure 5.12: Unit-cells of chosen structures of AgI wires after relaxation with no applied symmetries (a–f) and with symmetries enforced (g–l). The top row of each set of 6 shows the structure looking along the periodic direction, the bottom rows shows the side-view.

equilibrium:

$$E = E_0 + \sum_{i,\alpha} \frac{\partial E}{\partial u_{i,\alpha}} u_{i,\alpha} + \frac{1}{2} \sum_{i,\alpha,i',\alpha'} u_{i,\alpha} \Phi^{i,i'}_{\alpha,\alpha'} u_{i',\alpha'} + \text{h.o.t.} \tag{5.1}$$

where $u_{i,\alpha}$ is the $\alpha^{\text{th}}$ Cartesian coordinate of the $i^{\text{th}}$ atom, which has mass $M_i$. $E_0$ is a constant and so can be ignored. Since our systems are at a saddle-point equilibrium the first-derivative term is zero. This leaves only the matrix of force constants $\Phi^{i,i'}_{\alpha,\alpha'}$ where

$$\Phi^{i,i'}_{\alpha,\alpha'} = \frac{\partial^2 E}{\partial u_{i,\alpha} \partial u_{i',\alpha'}}. \tag{5.2}$$

This has as a solution

$$u_{i,\alpha} = \varepsilon_{m,i,\alpha} \exp[i\mathbf{q} \cdot \mathbf{R}_{i,\alpha} - \omega_m t] \tag{5.3}$$

for some lattice vector $\mathbf{R}_{i,\alpha}$, phonon wavevector $\mathbf{q}$ and mode $m$ with frequency $\omega_m$ and polarisation vector $\varepsilon_{m,i,\alpha}$. This leads to the eigenvalue-equation

$$\omega^2 M_i u_{i,\alpha} = \sum_{i',\alpha'} \Phi^{i,i'}_{\alpha,\alpha'} u_{i',\alpha'} \tag{5.4}$$

which can be solved by standard numerical methods.

If the system is at a minimum, then the matrix $\Phi^{i,i'}_{\alpha,\alpha'}$ is positive definite, and all values of $\omega^2$ are positive. Otherwise, there are modes corresponding to saddle-points along a polarisation vector $\varepsilon_{m,i,\alpha}$ with negative values of $\omega^2$, or equivalently imaginary mode frequencies. It is these saddle-point polarisation vectors which we investigate in §5.2.4.

We use CASTEP to calculate the phonons of both symmetry-constrained rock-salt-like structures, as well as the unconstrained 'Eliseev' structure. A much tighter electronic energy tolerance is used, requiring convergence to within $2 \times 10^{-10}$ eV for four SCF cycles. The phononic spectrum must be sampled at different $\mathbf{q}$-vectors, corresponding to different propagation directions of the phonon. In our one-dimensional systems all such propagation is along the axis, so we can choose $\mathbf{q}$-vectors of the form $(0, 0, q)$, where we term the axial component a $q$-point. The $q$-point path was sampled from $(0, 0, 0)$ to $(0, 0, 1/2)$ with 12 full calculation points, symmetry-reduced to 6 or 7 explicit calculations, and Fourier-interpolated onto a fine path with spacing $0.02\,\text{Å}^{-1}$.

The phonon plots of Figure 5.14 show clear unstable phonon modes. The unsheared rocksalt structure has 5 modes at a $\mathbf{q}$-vector of $(0, 0, 0)$, three of which are

still unstable at the $(0, 0, 1/2)$ **q**-vector where they are joined by two more, in total 7 modes are unstable at some point along the $q$-vector path. The sheared rocksalt structure has a similar phonon plot, with one less unstable mode. The 'Eliseev' structure, while relaxed to $0.001\,\mathrm{eV\,\AA^{-1}}$, still has four unstable modes. This seems contradictory, but is resolved by the observation that the unstable perturbation vectors all involve either the radial movement of neutral AgI planes, implying a shallow Van der Waals surface which would properly require an even tighter force tolerance to fully converge, or a rotation around the periodic axis, shown in Figure 5.13.

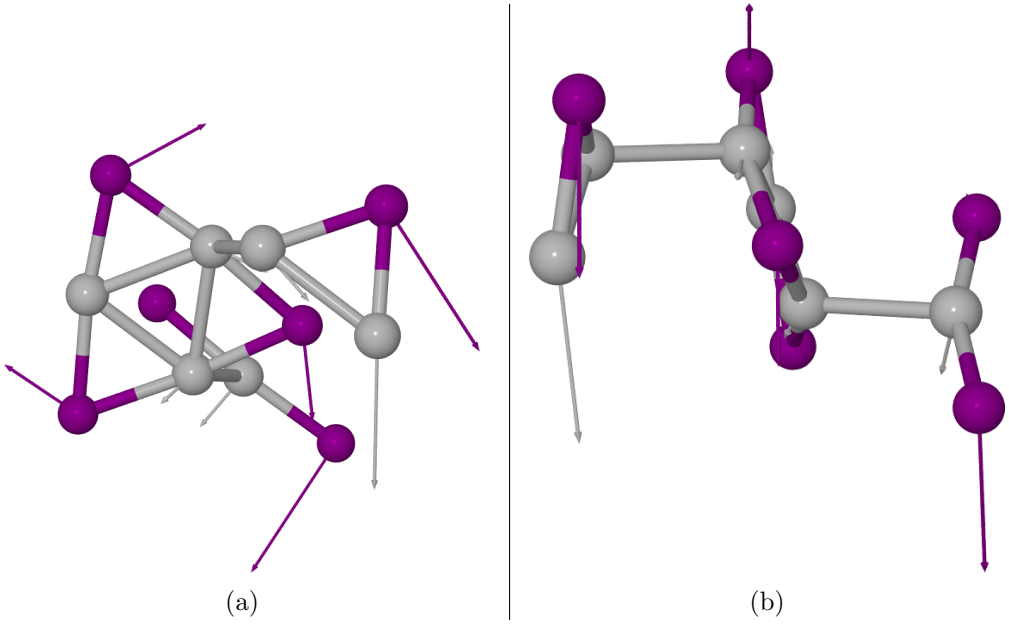


Figure 5.13: Perturbations corresponding to unstable phonon modes of incompletely-relaxed 'Eliseev' AgI. (a) shows a rotation around the periodic axis, while (b) shows neutral planes shearing past each other.

### 5.2.4 Stabilisation in tubes

These unstable modes can be 'followed', such that $r'_\alpha = r_\alpha + a u_\alpha$, for some amplitude $a$. For non-zero $q$-points, the term $i\mathbf{q} \cdot \mathbf{R}_{i,\alpha}$ in Equation (5.3) results in complex perturbations in the unit cell, corresponding to perturbations with longer periods than the atomic unit-cell. In order to represent the phonon as a real perturbation of atoms, that is, in order for the displacement $u_\alpha$ to be real, $\mathbf{R}_{i,\alpha}$ must be altered. In our case, a supercell is be created so that the phonon's phase can precess and the phonon can be fully represented. For simple q-points, such as the $(0, 0, 1/2)$ point, a simple $(1, 1, 2)$ supercell suffices. Away from these high-symmetry points, much

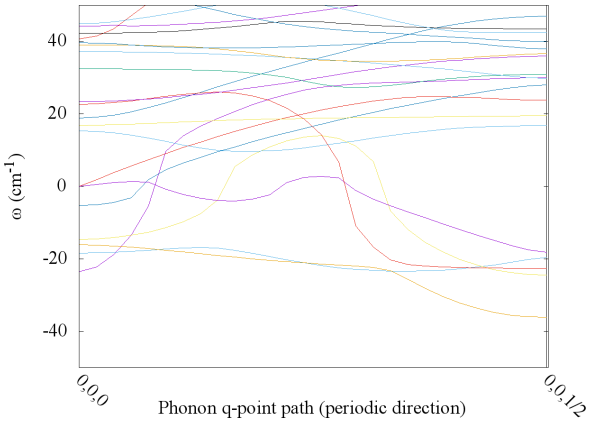


(a) Unsheared

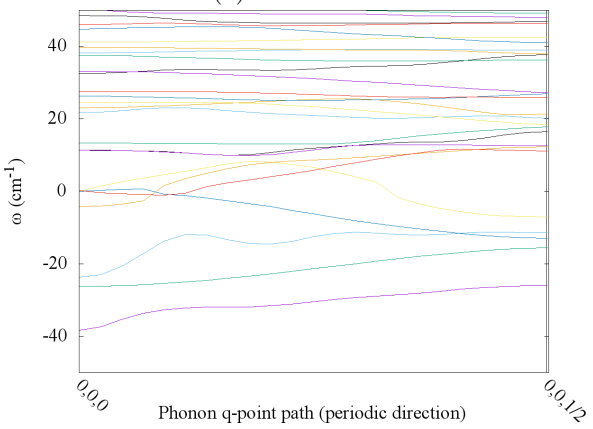


(b) Sheared

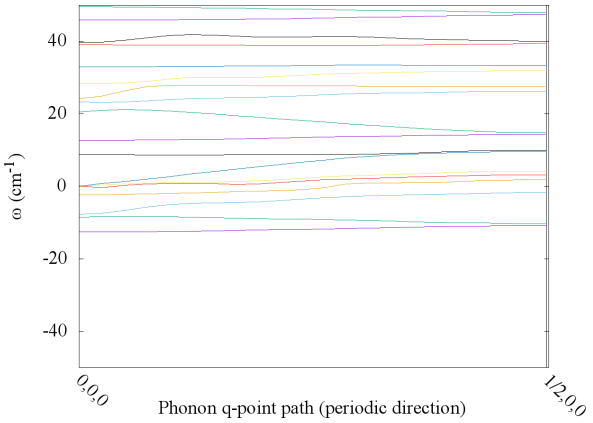


(c) 'Eliseev'

Figure 5.14: Phonon plots of bare AgI wires. In cases where $\omega^2$ is negative, $\omega$ is plotted here as negative for convenience. Bands are colored in no particular order.

larger supercells are required, for example $(0, 0, 25/54)$ requires a $(1, 1, 54)$ supercell. Fortunately all the unstable modes of interest for our systems are unstable either at $(0, 0, 0)$ or at $(0, 0, 1/2)$, meaning that a two-unit supercell is sufficient to represent all phonons of interest.

Now we investigate the effect of encapsulation on these 'followed' modes. Mismatch is again a consideration here, and compound systems were chosen so that the maximum strain $\Delta L$ was 0.1 Å per crystal unit and the maximum strain-energy was 1 meV per atom.

The incommensurability of the nanotube and core means that different core images lie at different points along the tube's unit-cell. At narrow tube diameters this can cause significant differences in the interaction, see Figure 5.15, as a core atom might be, for example, just to the left of a tube atom in one image, and just to the right in another.

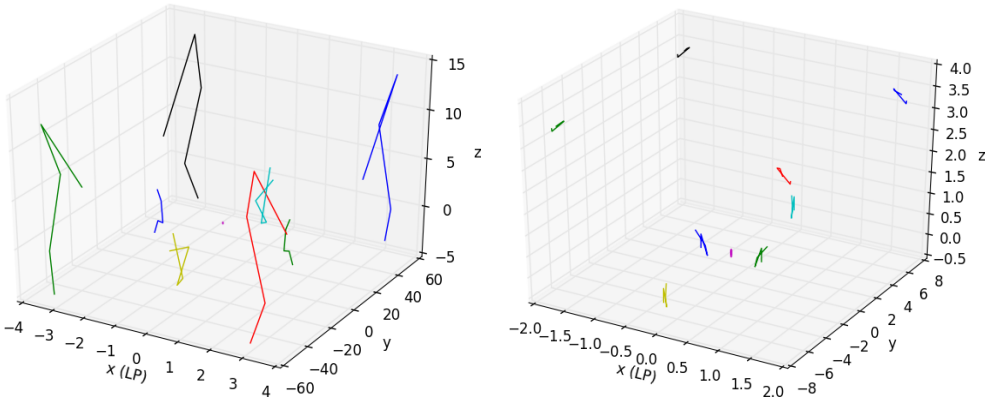


(a) (14-0) CNT (b) (16-0) CNT

Figure 5.15: Forces on Ag atoms of a system of 5 units of unsheared-rocksalt AgI followed along mode-1 with an amplitude of 3.0, encapsulated by CNTs of different radii. Atoms which are periodic images of each other are joined by lines of arbitrary color. Units are eV $\text{Å}^{-1}$. The axial direction is $x$; $y$ and $z$ are radial.

One advantage of dealing with orthogonal phonon modes is that the complex interactions between tube and $N$-atom core can be represented by a single dot-product $d = \mathbf{f} \cdot \mathbf{u}$ for each mode, where $\mathbf{u}$ is the $3N$ perturbation vector of the phonon mode and $\mathbf{f}$ the $3N$ vector of resultant forces on the crystal core. A negative dot-product $d$ indicates that the effect of the tube is restorative. While the force on a single atom may act along the direction of its individual perturbation, suggesting instability, it is only the dot-product of the entire mode that is important: deviations from the mode are represented by separate modes.

The graph of these force-perturbation dot-products for the unsheared rock-

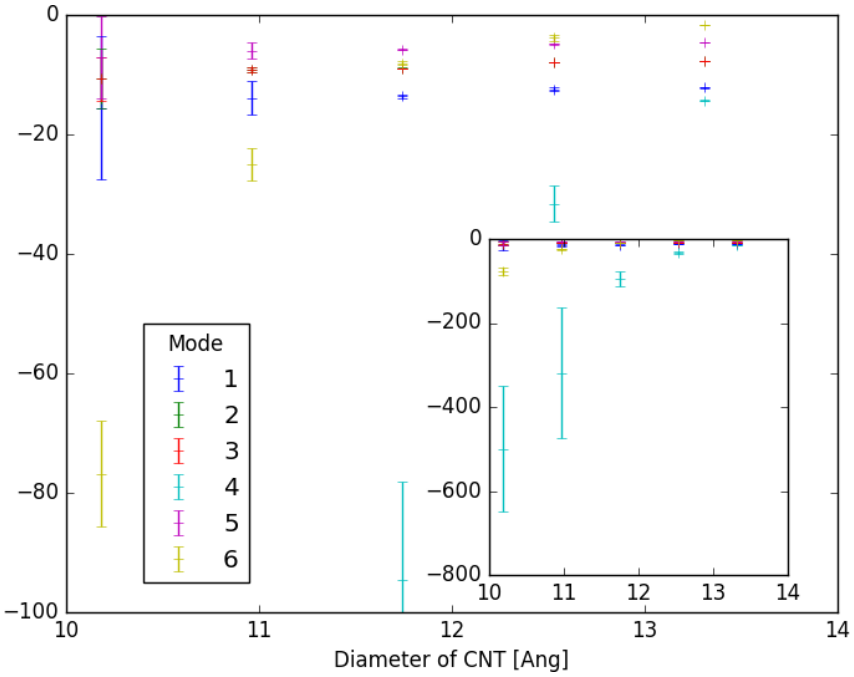


(a) Unsheared

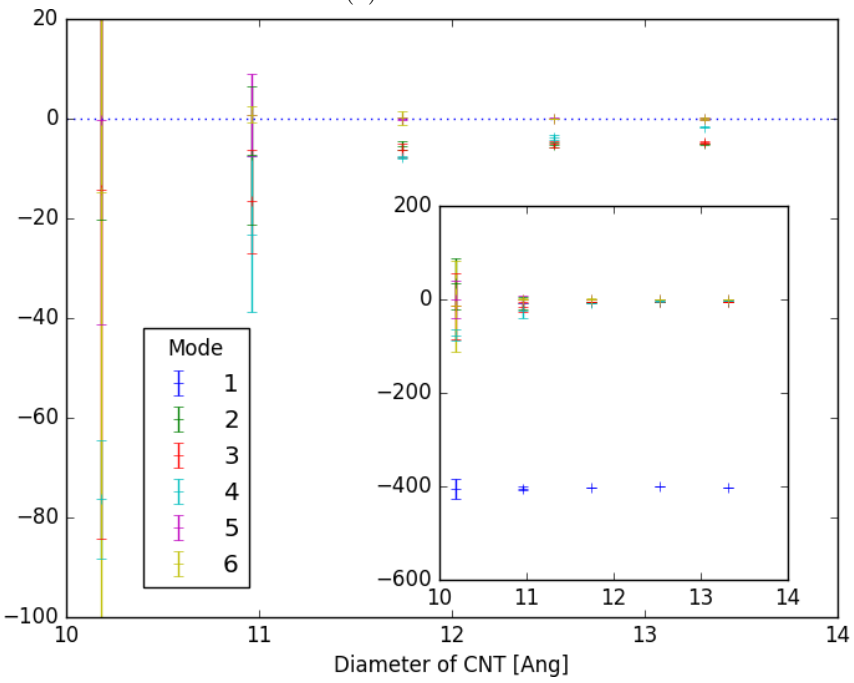


(b) Sheared

Figure 5.16: Dot-products of phonon perturbations [Å] and resultant force on filling ions [eV $\text{Å}^{-1}$] for unstable bare AgI wire modes at the $(0, 0, 0)$ **q**-vector. The central point gives the mean dot-product over all periodic images, the error bars give the standard-deviation of the spread due to mismatch.

salt structure (see Figure 5.16a) exhibits a few notable features. Firstly, all the dot-products are negative, indicating that all the modes which are unstable in the bare system are stabilised by the constraining nanotube.

In addition, there are two different behaviours of dot-products with varying nanotube diameter. Some modes, most notably modes 4 and 6 of the unsheared rocksalt, are significantly less stabilised in wider tubes, as one would expect; presumably in the case of a tube of infinite diameter these modes are no longer stabilised. These modes correspond to perturbations with significant expansions in the radial direction, see Figure 5.17a for an example.

The other behaviour, that of the unsheared rocksalt's mode 5 and of the sheared rocksalt's mode 1, seems less physical. Here the interaction of tube and unstable phonon seems independent of tube diameter. On closer inspection these modes correspond to axial, rather than radial, perturbations, as shown in Figure 5.17b. When such modes are followed, investigation of the equilibrium axial length $L_p$ of the bare filling shows that the unstable modes require an axial relaxation which is constrained by the length of the encapsulating nanotube unit-cell, similar to the effects of mismatch.

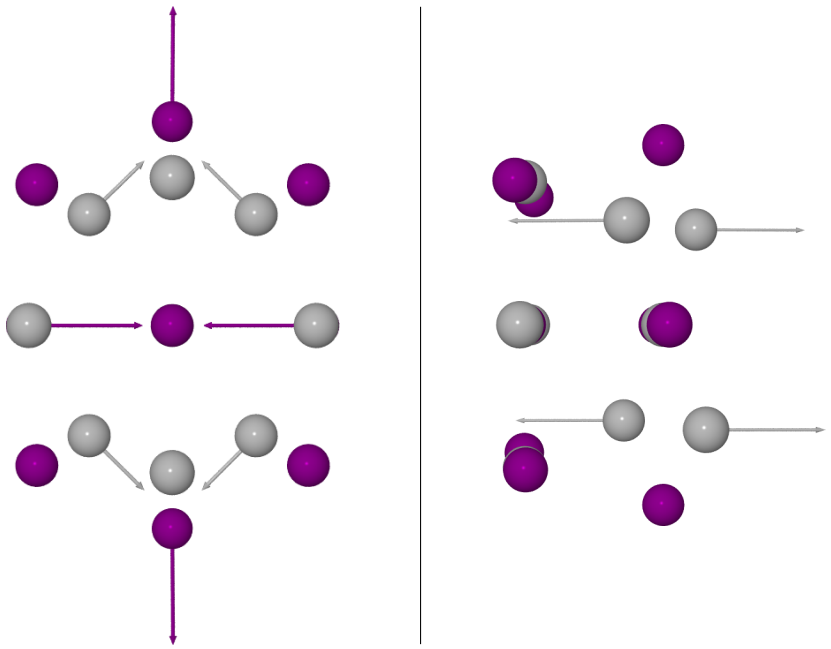

(a) Unsheared mode 4, front (b) Unsheared mode 5, side

Figure 5.17: Perturbation corresponding to phonon modes of bare crystal nanowires. Absolute amplitudes of vectors are arbitrary. Axial components of (a) are all zero, as are the radial components of (b).

## 5.3 Summary

At the start of this chapter we see that the ridged texture of the inside of encapsulating tubes resists smooth axial gliding (see Figures 5.2 and 5.3) as well as rotation of the core within the tube (see Figures 5.5 and 5.6). The magnitude of this resistance depends, as expected, on the radius of the tube. However we find that, more surprisingly, the ratio of translation-resistance to rotation-resistance depends on the tube chirality, with armchair tubes resisting rotation and translation equally but zigzag tubes preferring rotation to axial shift by an energetic factor of 10 (see Table 5.1 and Figure 5.7).

These results are achieved by moving the crystal core as a rigid rod. For longer nanowires different parts of the core can sit in different rotational minima, and we show that for the case of a chain of KI octopoles encapsulated in a (13,0) CNT a system initialised to straddle a maximum between two such minima relaxes to a metastable state away from the global minimum (see Figure 5.9), while the inter-ionic forces prevent wholesale rotational shearing of the core. Importantly, this metastable state relies on the tube texture and so would not be discoverable if a smooth confining potential were used.

While the results so far deal with the effects of texture on the core crystal, Section 5.2 investigates the feasibility of modelling confined crystal completely *in vacuo*, using symmetry constraints in the place of a constraining tube In general there is no justification for ignoring the confining tube, and we see structures which we expect to exist within CNTs (such as the $3 \times 3 \times 2$ rocksalt) collapse to unlikely structures when not confined (although the 'Eliseev' structure is stable even outside the tube). However, by restricting the structures to remain subject to their initial symmetries we relax the experimentally-incentivised anzatze to 'unphysical' metastable states on saddle-points of the energy surface, where we analyse the phononic spectrum to find the modes which are stabilised by the artificially-applied symmetries.

When these unstable modes are 'followed' and simulated inside an encapsulating tube we see that movement along these modes is opposed by the force applied by the tube. Two classes of mode are distinguishable. The first class comprises radial modes which are restored by the encapsulating tube wall, which become unstable as the tube diameter increases. The second comprises axial modes which lead to a longer crystal-core equilibrium length, who are restored by a diameter-independent mismatch-like constraint.

The results so far suggest the need for more than a simple smooth cylindri-

cal confining potential to accurately model the state of the encapsulated crystal. However, a more advanced textured confining potential would address all the issues raised in this chapter. In the coming chapter, we address the next significant hurdle: charge transfer.

# Chapter 6

# Charge Transfer

Charge transfer between nanotubes and their filling is a well-established phenomenon [Kharlamova, 2013], and charge can also be transferred between filling ions themselves so that their charges are quite different from those in bulk. This charge transfer may cause positive and negative core ions to behave differently in the presence of the tube, with the wall charge causing additional radial attraction or repulsion, as well as a modified electronic interaction between the core ions themselves. Charge injection of $\pm 0.01\,e$ has also been predicted to affect the length of C-C bonds in CNTs by up to 0.05 Å [Sun et al., 2003]. Charge transfer has been observed in simulations of KI@CNT, CsI@CNT and AgX@CNT (X=Cl, Br, I) [Sceats et al., 2006, 2008; Bichoutskaia and Pyper, 2008; Eliseev et al., 2010]. Bandgap narrowing has been seen in the case of CNT-encapsulated metallofullerenes [Lee et al., 2002], attributed to charge transfer from the tube to encapsulated Gd@$C_{82}$. Raman spectroscopy can be used to observe vanishing metallic behaviour due to encapsulation of donors [Eliseev et al., 2010], however the understanding of atomic-level charge-transfer behaviour requires the use of *ab initio* techniques.

In general the simple chirality rule [White et al., 1993] for nanotube band gaps is that CNTs with chirality ($n$-$m$) have zero band gap if $n - m = 3q$ for some integer $q$, else the CNT has a moderate band gap of the order of 1 eV which increases with diameter [Wilder et al., 1998]. This fails for the case of narrow tubes with large wall surface curvature: small band gap semiconducting CNTs have band gaps which arise solely from the symmetry-breaking of the tube wall curvature [Kleiner and Eggert, 2001]. For example, the (8-2) CNT has a zero band gap as expected, but the (9-0) CNT has a band-gap of ∼80 meV [Matsuda et al., 2010]. An exciting result of this is that the electronic properties of CNTs can be modified by radial deformation due to pressure or strain, even metallising semiconductive tubes [Lu

| Chirality | Diameter [Å] | Band gap type | Band gap [meV] |
|---|---|---|---|
| 9-0 | 7.05 | small | 79 |
| 8-2 | 7.18 | metallic | 0 |
| 10-0 | 7.87 | moderate | 1081 |
| 6-6 | 8.14 | metallic | 0 |
| 7-5 | 8.18 | moderate | 1105 |
| 11-0 | 8.61 | moderate | 1139 |

Table 6.1: Chiralities, diameters (carbon centre to carbon centre) and bad gaps of CNTs chosen to encapsulate 1D CsI chains. (Values from simulations by Matsuda et al. [2010, Suppl. Inf.], which agree to experimental work by Ouyang [2001] with error ±5 meV.)

and Chen, 2005].

In this chapter we describe the case for the less-explored case of encapsulated CsI, though the principles should extend to KI or other ionic crystals. We begin by investigating the charge transfer for a system comprising a perfect 1D chain of 6 units of CsI, evenly spaced along the centre of a carbon nanotube. The exact spacing depends on the equilibrium length of the CNT, but in each case is 7.3(2) Å. We choose nanotubes with a range of diameters from 7.05 Å to 8.61 Å, including metallic, small band gap semiconducting and moderate band gap semiconducting nanotubes, see Table 6.1.

We then investigate systems with perturbed filling, keeping the nanotube fixed. For each tube we take 100 instances of evenly spaced 1D $(CsI)_6$ along the axis before perturbing the filling ions randomly in each Cartesian coordinate (where $z$ is the axial direction) according to a uniform distribution of magnitude 0.6 Å, leading to a quasi-normal perturbation of magnitude 1 Å.

Later, in §6.1.5, we investigate structures found via the *ab initio* random structure searching method of Pickard and Needs [2006].

### 6.0.1 Density field

The foundation of our investigation into charge transfer must be the valence electron density field, together with the pseudised ion cores. CASTEP can output the valence electron density of the electronic ground-state of a system, stored on a cubic grid whose granularity is controlled by a combination of cutoff-energy, `fine_grid_scale` and unit-cell dimension. Seven valence electrons were modelled for each iodine ion, nine for caesium (explicitly modelling the outermost complete shell) and four for carbon. A cutoff energy of 500 eV was used which converged the final energy to within 1 meV per atom of the values at 400 eV. Only the Γ-point was required

for similar convergence. The pseudopotentials used were the standard CASTEP-8 on-the-fly (OTF) PBE ultrasoft PPs [CASTEP website].

The electron density field for one particular system, a perfect 1D chain of 6 units of CsI encapsulated in a (9-0) carbon nanotube, is shown in Figures 6.1a and 6.1b. Of particular note is the negative space at ionic cores, where the pseudised cores exclude valence electrons.

To investigate the interaction of the tube and filling, we calculate an electron density difference $\delta\rho = \rho_{\text{nanowire}} - \rho_{\text{CNT}} - \rho_{\text{filling}}$, where $\rho_{\text{CNT}}$ and $\rho_{\text{filling}}$ are the electron densities of the bare, non-interacting systems. We show this density-difference for the same $(\text{CsI})_6@\text{CNT}_{(9,0)}$ system as before in Figures 6.1c and 6.1d. The magnitude of the electron density difference is much smaller than that of the density itself; the system contains 1536 valence electrons, most of which belong to the nanotube, while the integrated $|\delta\rho|$ is around $6\,e$. As we will show later, the effects on the encapsulated ions are still significant.

Note also that while the total electron density on the tube is significantly interstitial, the density-difference is mainly on the interior of the CNT wall, rather than in the interstital region as suggested by Yam et al. [2004].

More surprising is the charge-transfer in the case of perturbed CsI wires, shown in Figure 6.2. The transfer to and from the CNT is of the same order of magnitude as for the symmetrical case, but the transfer between ions is much larger, revealing that the presence of the CNT encourages transfer between the filling ions.

## 6.1 Point Charges

The CASTEP code is capable of internally calculating Mulliken charges, using the projection technique of Sanchez-Portal et al. [1995], previously used for both molecular and bulk materials [Segall et al., 1996a,b]. The choice of localised Bloch functions onto which the density is projected is the set of atomic pseudo-orbitals generated from the pseudopotentials used in the calculation. The CASTEP code is also capable of internally calculating Hirshfeld charges using the unrelaxed atomic densities as reference densities.

### 6.1.1 Bader charges

We use the code created by Henkelman et al. [2006] to partition the electron density field output by CASTEP into Bader volumes. We then used the `den2cube` code created by Aaron Hopkinson and Matt Probert [den2cube website] to generate `.cube` files. These files had an extra layer of voxels in each direction, such that the leftmost

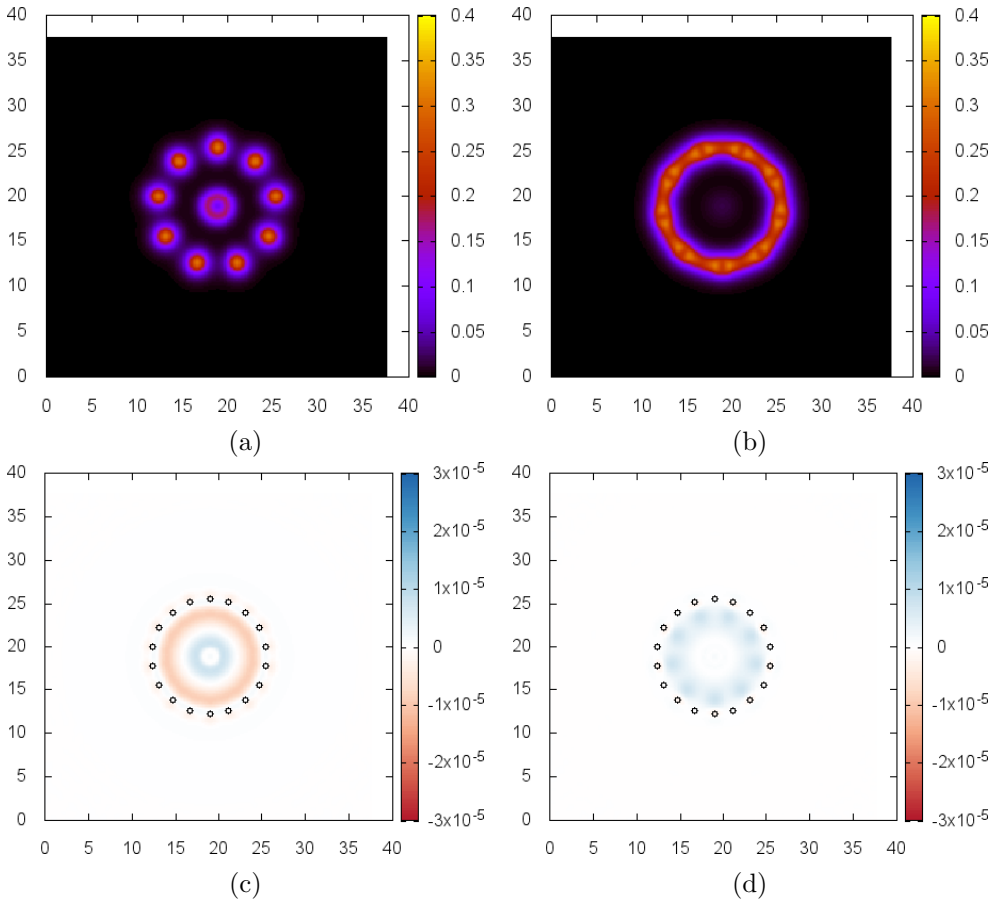


Figure 6.1: Figures 6.1a and 6.1b show cross-sections of the valence electron density of a perfect 1D CsI chain encapsulated in a (9-0) carbon nanotube. The $x$ and $y$ axes give distances in $a_0$, the colour legend gives electron density in $e\,{a_0}^{-3}$. Since the tube has 'zigzag' ($n$-0) structure, it is quite symmetrical. Figure 6.1a shows the carbon-carbon bonds along the axial direction, while Figure 6.1b shows the bonds around the tube, as well as valence electrons centred on the carbon atoms. Figure 6.1a also shows the valence electrons around an encapsulated ion, the negative space in the centre shows where the valence electrons are being excluded by the pseudised core. Figures 6.1c and 6.1d show cross-sections of electron transfer between perfect 1D CsI chain and encapsulating (9-0) carbon nanotube. Figure 6.1c shows the cross-section near an iodine ion, Figure 6.1d shows that near a caesium ion. The white circles represent the centres of the carbon atoms; since the tube is 'zigzag' only every other carbon is present at any one cross-section.

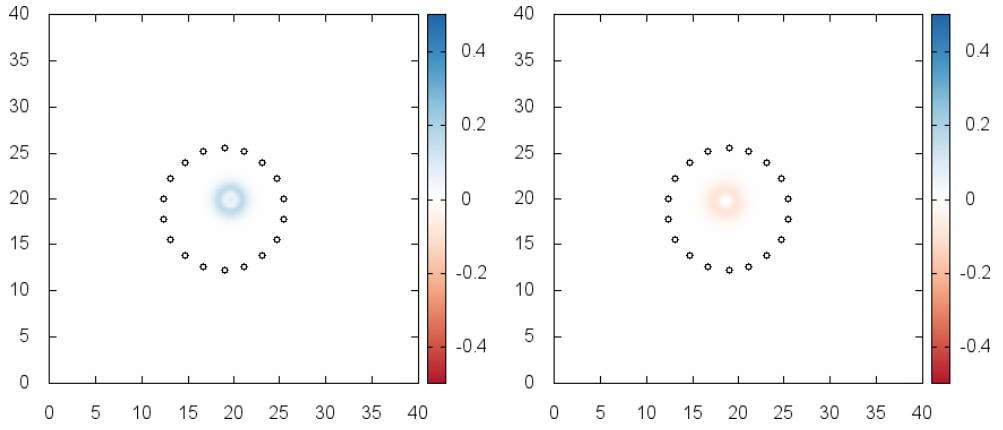


(a) (b)

Figure 6.2: Cross-sections of valence-electron density-difference for perturbed encapsulated 1D CsI. Electron transfer is much stronger than for the symmetrical case of Figures 6.1c and 6.1d. Charge is still transferred to and from the CNT, but at a scale drowned out by the transfer between ions.

layer was repeated on the right and so on, presumably to aid in visualisations of periodic systems. These were removed by custom scripts, which also converted from values of charge-per-voxel to charge-density.

These density files represent only the valence electron density, the core electrons being represented by pseudopotentials. This results in a collection of local maxima around the edge of the pseudopotential, see Figure 6.4.

Each of these local maxima is assigned a separate Bader volume, which - since the density gradient increases most steeply in a radial direction - gives rise to the composition shown in Figure 6.5a. Fortunately, since Bader volumes are assigned to atoms based on the position of their maxima (as opposed to e.g. their centre of mass) the Bader volumes are merged to form atomic volumes in a physically meaningful way.

To confirm that the structure arises from this distribution of maxima and not from some physical property of the system (say, antinodes in the electron distribution) an artificial 'volcano' density was created, of the form:

$$\rho(\mathbf{r}) = A_L \exp\left[-\frac{(\mathbf{r}-\boldsymbol{\mu})^2}{\sigma_L}\right] - A_S \exp\left[-\frac{(\mathbf{r}-\boldsymbol{\mu})^2}{\sigma_S}\right] \tag{6.1}$$

where $A_S < A_L$ and $\sigma_S > \sigma_L$. This 'volcano' distribution produces the same distribution of Bader volumes, see Figure 6.5b.

Another cause for concern is the highly spherical nature of the merged atomic

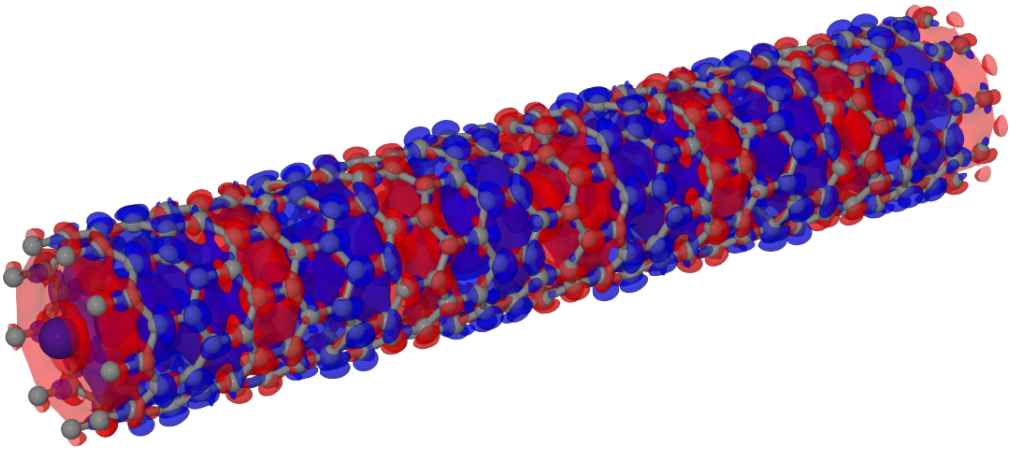

(a)

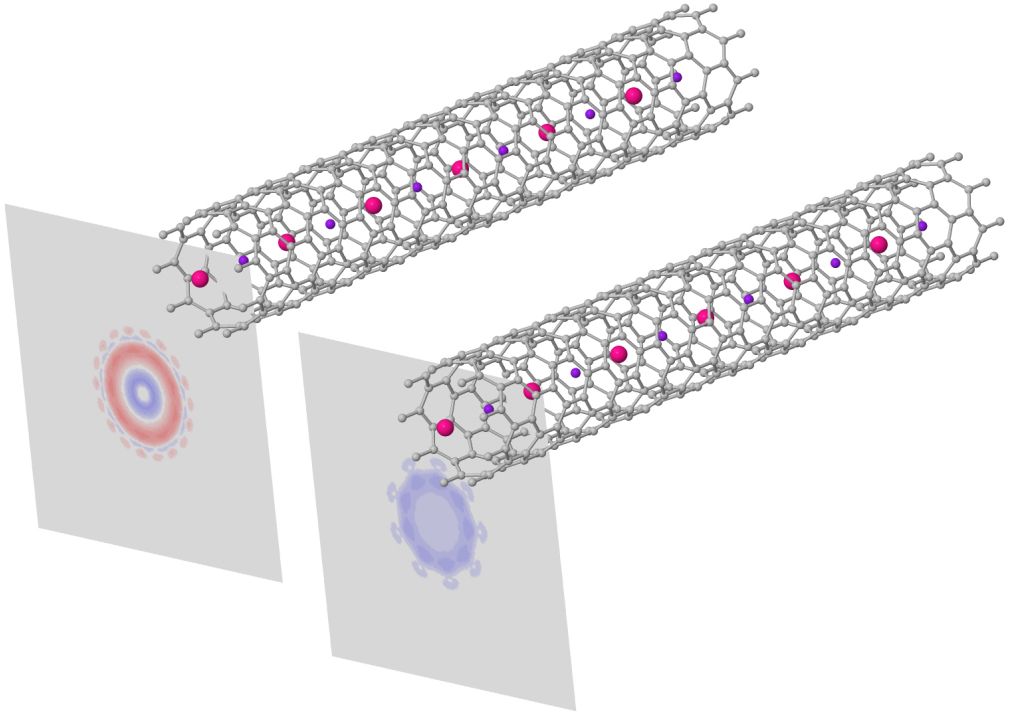

(b)

Figure 6.3: Above: Isosurfaces of the electron density difference for a perfect 1D chain of CsI encapsulated in a (9,0) carbon nanotube. Blue is the $1 \times 10^{-8}\, e\, {a_0}^{-3}$ isosurface, which are centred on the caesium ions; red is the $-1 \times 10^{-8}\, e\, {a_0}^{-3}$ isosurface, which are centred on the iodine atoms.
Below: Offset cross-sections of the electron density difference. The corner of the grey plane shows the ion which the plane intersects. Iodine ions are represented as small purple spheres at 20% Van der Waals diameter, the large pink spheres represent the caesium ions.

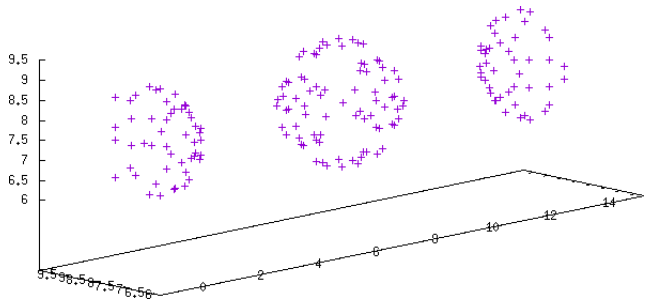


Figure 6.4: Local maxima of the electron density field of a unit cell of a CsI 1D chain. Each is assigned its own Bader volume, which are later assigned to the atom closest to the maximum and merged.

volumes. This arises in part from a detail of the code: any point with a charge density lower than some adjustable 'vacuum cutoff' is ignored, and its charge assigned to the vacuum. As this vacuum cutoff is decreased more points are assigned to atoms, and the Bader volumes take on a more complex shape (see Figure 6.5c). The vacuum cutoff can be sensibly converged (see Figure 6.6) so that a finer tolerance would only increase the size of volumes without significantly affecting atomic charges.

At an appropriate choice of vacuum cutoff (here $1 \times 10^{-5}\, e\,\text{Å}^{-3}$) the electron distributions of filling and tube are clearly separate (see Figure 6.7a) while electrons belonging to the tube are assigned to carbon atoms in a physically sensible manner (see Figure 6.7b).

Very rarely, the maximum of a partial Bader volume will be assigned to an ion to which it does not intuitively belong, see Figure 6.5d. This usually occurs only when atoms are unphysically close, and the large deviation of Bader volume from the expected range makes these artefacts easily detectable.

### 6.1.2 DDEC charges

We used the DDEC3 `chargemol` code created by Manz and Sholl [2012] to assign charges. The code requires density grids with voxel volume of less than $0.0081\, {a_0}^3$, which required setting CASTEP's `fine_grid_size` parameter to 3.6. Minor modifications were required to change the reference core densities used by `chargemol` to avoid the extremely fine grid a core-density field would require, since `chargemol` by default assumes the largest possible complete shell is pseudised. Periodicity was applied in all 3 dimensions, but the DDEC charges were converged to within $0.007\, e$ at an image-separation of 13 Å, comfortably within the 20 Å used for production.

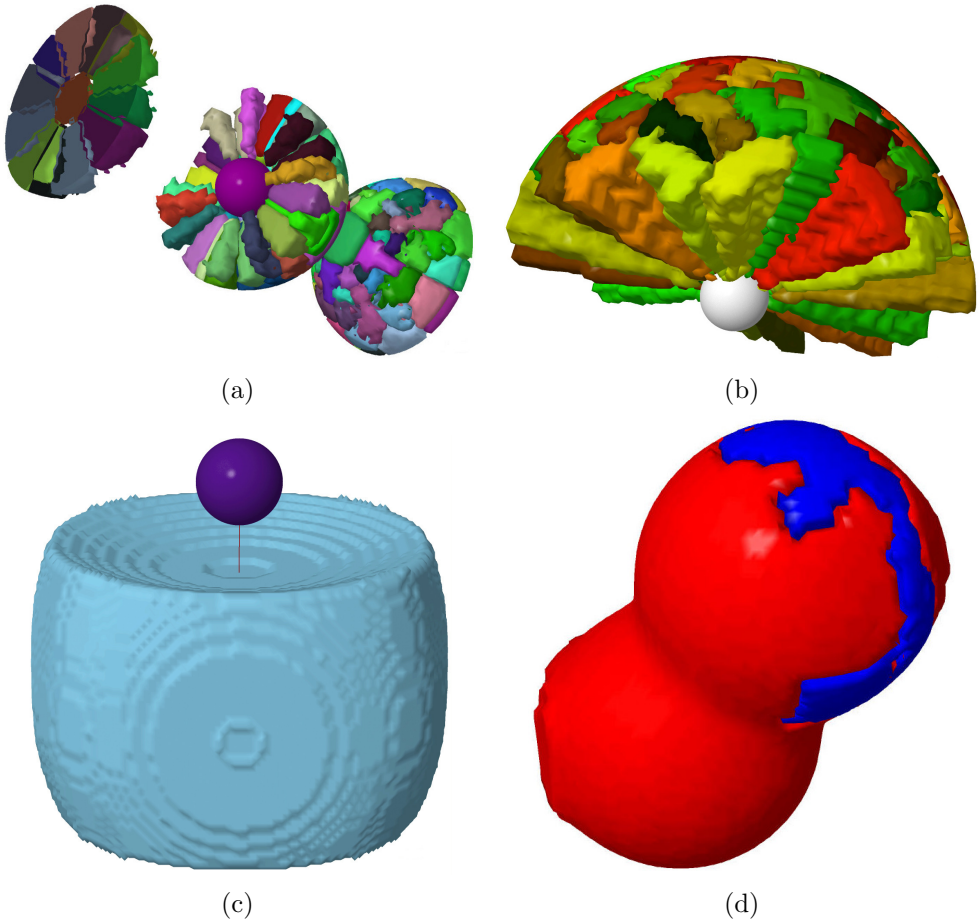

Figure 6.5:
(a) Bader volumes of a unit cell of a CsI 1D chain. The compound nature is due to the multitude of local maxima arising from the use of pseudopotentials, while the sphericity stems from an over-aggressive density cutoff.
(b) Bader volumes of a perfect "volcano" charge distribution. The charge distribution consists of two concentric Gaussian distribution with the smaller Gaussian distribution subtracted from the larger. This gives rise to multiple maxima, each with its own Bader volume.
(c) Compound atomic Bader volume of a Cs ion in a unit cell of a CsI 1D chain. With a lower threshold for 'vacuum charge', the Bader volume is no longer spherical. Ripples in the surface are due to the finite resolution of the grid.
(d) Misattribution of partial Bader volumes from iodine (blue) to caesium (red). This system has an unphysical proximity of the Cs and I ions to exaggerate the effect, their separation here is 2.3 Å compared to a sum of covalent radii of 4 Å. Even in less extreme instances partial volume misattribution can be clearly identified by inspecting the atomic Bader volume.

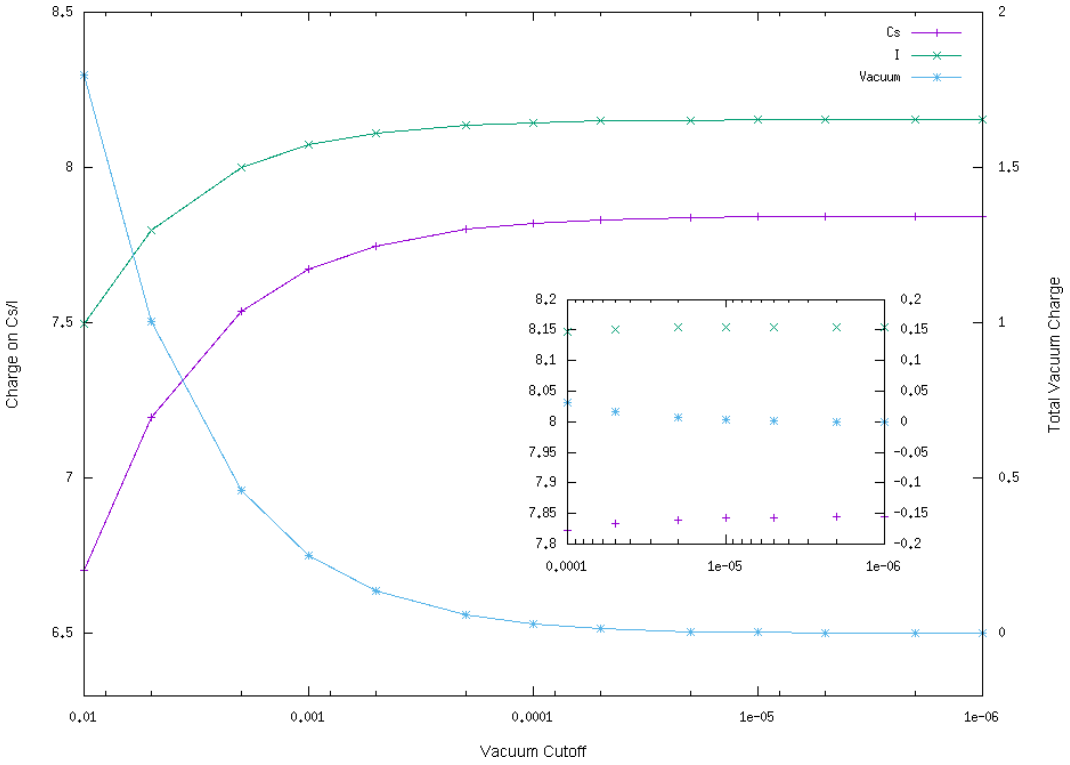


Figure 6.6: Convergence of the charge assigned to the Cs and I ions (left axes) and to the vacuum (right axes) with increasingly-small points are assigned to ions. Once points with electron density $1 \times 10^{-4}\, e\, \text{Å}^{-3}$ are included (see inset) charges are converged to within $0.05\, e$.

### 6.1.3 Comparison of atomic-charge methods

The four population analysis schemes previously discussed — Mulliken (MPA), Hirschfeld (HPA), Bader (BPA) and DDEC — were each applied to systems of CsI@CNT. Figure 6.8 shows the distributions for one representative such set of systems: a set of 100 perturbed 1D $(CsI)_6$ chains encapsulated in (9,0) nanotubes.

The Mulliken and Hirshfeld charges exhibit their expected flaws. The Mulliken charges (Figure 6.8a) are wildly different from the other schemes, describing the clearly unphysical transferal of more than an entire electron from each caesium atom to the nanotube, while the Hirshfeld charges (Figure 6.8b) underestimate the magnitude of the atomic charges compared to other methods.

The mean values of the Bader and DDEC schemes (Figures 6.8c and 6.8d) agree to within $0.05\, e$, however the Bader charge distributions are — in general — broader than those predicted by DDEC, and distributed less regularly. This is especially noticeable for the low-charge carbon atoms: the Bader analysis assigns

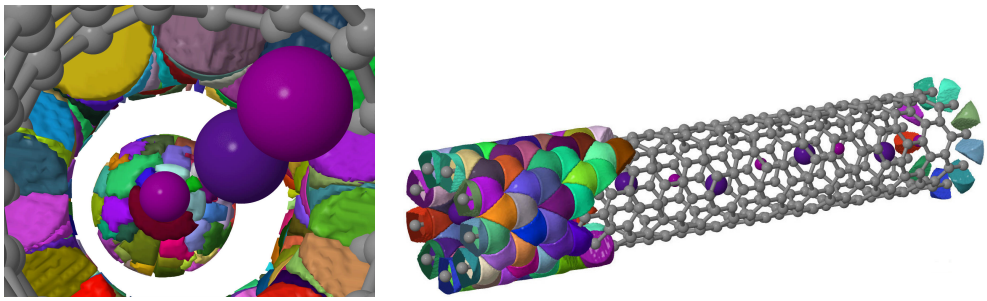

(a) Unmerged Bader volumes (b) Merged atomic Bader volumes

Figure 6.7: Merged and unmerged Bader volumes of a perturbed 1D CsI chain encapsulated in a (9,0) CNT. The vacuum cutoff is set to $1 \times 10^{-5}\, e\,\text{Å}^{-3}$ and the smooth spheres represent 20% of the ionic Van der Waals radii. There is no inter-penetration of the volumes of the ions and of the CNT. The splitting of Bader volumes due to multiple minima does not affect the physical partitioning of the electronic structure. Atomic Bader volumes of larger ions typically comprise more local minima, carbon atomic Bader volumes invariably comprise three whereas iodine and caesium ions comprise around 30 and 50 minima respectively.

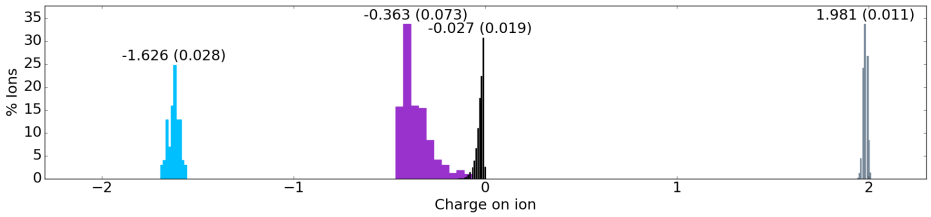


(a) Mulliken (note wider charge scale)

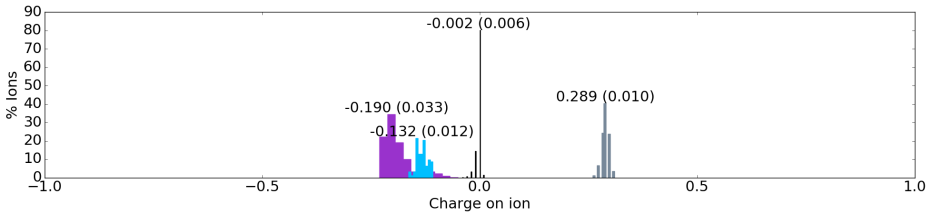


(b) Hirshfeld

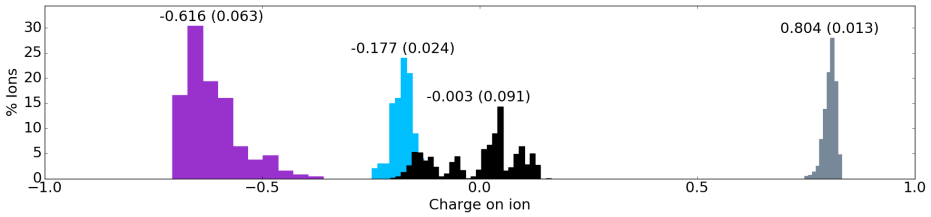


(c) Bader

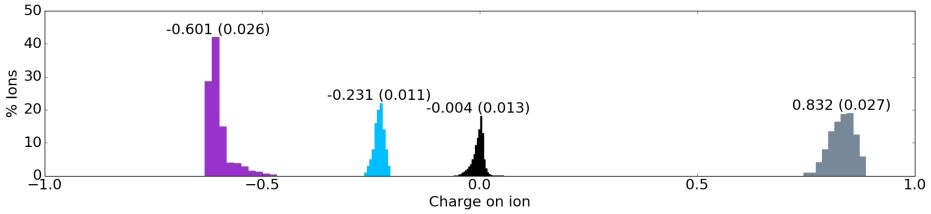


(d) DDEC

Figure 6.8: Comparison of charges (in $e$) assigned by the Mulliken, Hirshfeld, Bader and DDEC schemes to atoms for a collection of 100 systems of perturbed 1D $(CsI)_6$ chain encapsulated in a (9,0) carbon nanotube. Purple bars represent the charge on iodine atoms, silver represents caesium atoms and black represents carbon atoms. The blue bars represent a sixth of the charge on the carbon nanotube, i.e. the charge on the nanotube per (CsI) unit. The numbers above the peaks represent the distribution's mean, with the standard-deviation in brackets.

charges of up to $\pm 0.2\,e$ to the carbon atoms, whereas the charges assigned by DDEC are tightly clustered around 0.

Each distribution is skewed, with a tail leading towards neutrality. This makes the standard-deviation a questionable metric, especially for highly non-normal distributions such as that for the Bader charges of the carbon atoms.

One key detail to note is that while each individual carbon atom has a near-zero charge, the total charge transferred to the carbon nanotube is significant. This suggests that in practice it would be easier to predict the charges of the central ions directly, and infer the charge on the carbon atoms as some distribution of the remaining charge, rather than trying to accurately predict the charge on the carbon atoms directly.

Since the Bader and DDEC schemes use very different approaches to reach the same plausible result, we choose their prediction to represent the characteristic net atomic charge. Since DDEC intentionally minimises any multipole contributions, whereas the Bader volumes are significantly non-spherical (see Figures 6.5c and 6.7b), and since the Bader scheme occasionally misattributed charge (see Figure 6.5d), we use only the DDEC NACs from this point on. This has the added advantage of justifying the use of standard deviation, since the skew of the DDEC distributions is quite small.

### 6.1.4 Effect of nanotube diameter

The same 100 systems of perturbed CsI wire were encapsulated in each of the CNTs of Table 6.1, and DDEC charges were calculated for each ion. Figure 6.9 shows the DDEC charges assigned to the atoms of these systems, together with the charge transferred to the CNT as a whole.

The relationship between charge transfer and tube radius is stronger at narrower tubes, with iodine losing $0.1\,e$ between the (9-0) tube (with diameter 7.05 Å) and the (6-6) tube (with diameter 8.14 Å), before levelling out at larger diameter. The charge on each individual carbon atom is negligible, yet when summed over a whole system the CNT accepts around $0.2\,e$, depending on radius, per CsI unit. Most of this transferred charge is donated by the iodine, the caesium charges are much less affected. The standard deviation of the charges is much greater at narrower tube diameter, since the constant perturbative noise applied to the filling is proportionally larger in those systems.

While the charge-transfer appears to be levelling out at larger diameter, the DDEC charges of the unencapsulated ions are $\pm 0.912\,e$, with a standard deviation of less than $0.005\,e$, and the net charge on the bare nanotube is of course 0. This sug-

gests that the charge-transfer remains even at diameters much larger than examined here.

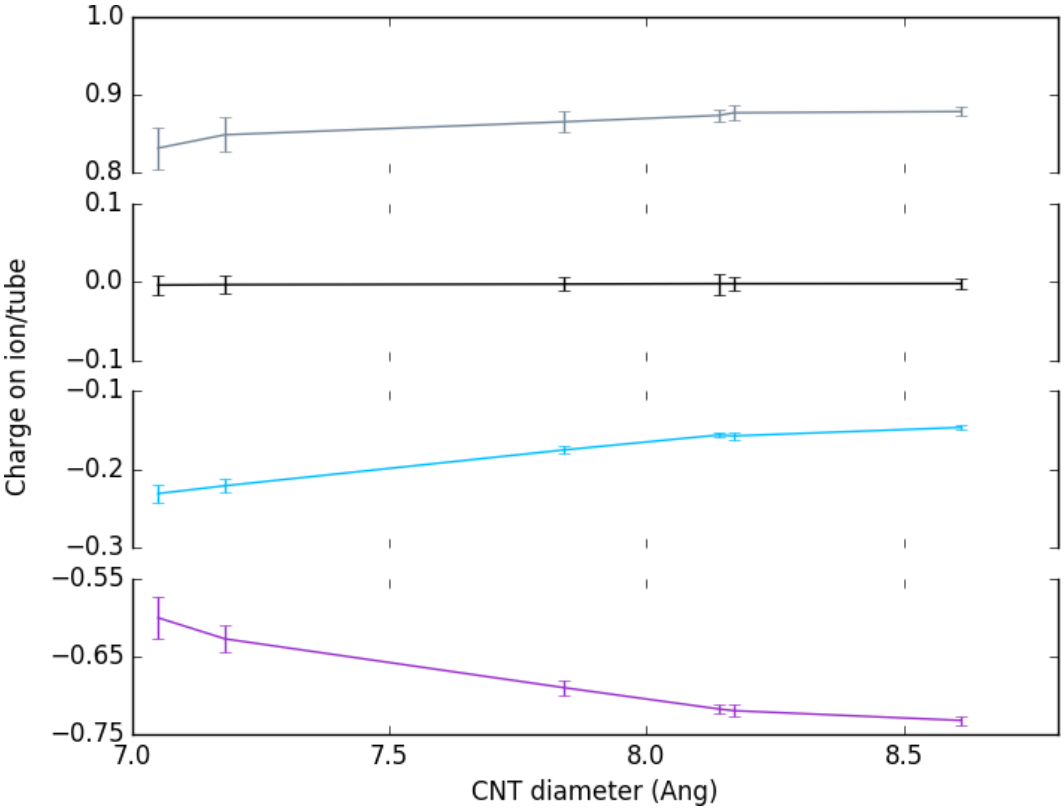


Figure 6.9: DDEC charges assigned to (top to bottom) caesium (grey), carbon (black), nanotube (blue) and iodine (purple), in systems of perturbed 1D CsI encapsulated in CNTs of different radii. The value for the CNT charges is a sixth of the total charge attributed to all carbons in the $(CsI)_6$@CNT system, i.e. the charge transferred to the tube per CsI pair. Error bars show the standard deviation of the charges across 100 perturbed systems per CNT radius.

### 6.1.5 AIRSS structures

We now progress from simple 1D CsI wires to more complex systems. Figure 6.10 show two similar $Cs_2I_2$ structures discovered by Vasylenko [2016] via *ab initio* random-structure search (AIRSS) [Pickard and Needs, 2006] in tubes with chirality (5-5), which were the smallest tubes to show encapsulated structures more complex than a 1D chain. The Cs and I ions in these structures were perturbed by the same Cartesian-normal 1 Å norm distribution as the earlier 1D system, while the distorted CNTs were kept fixed. Only a single periodic unit was used for each system, and 400 perturbations were simulated for each structure.

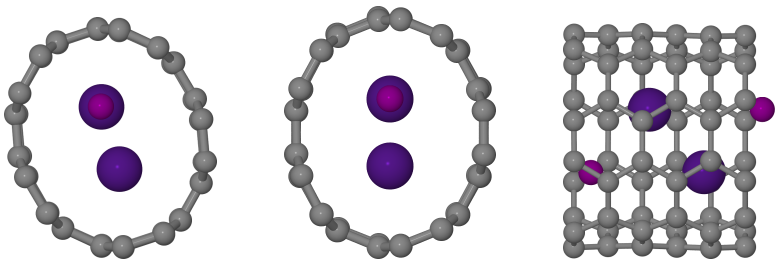

(a) Higher energy (b) Lower energy (c) Side-view

Figure 6.10: Structures of Cs (large purple) and I (small pink) inside a (5-5) CNT, found by Vasylenko [2016] via AIRSS. Figure 6.10a is slightly higher in energy than Figure 6.10b, largely due to the orientiation of the CNT, which has deformed significantly to accommodate the filling. Figure 6.10c shows the side-view of the lower-energy structure, though the higher-energy structure is very similar.

The assigned DDEC charges are shown in Figure 6.11. The Student's $t$-test determines that the charge distributions for the two sets of structures are not significantly different ($p = 0.05$). The most striking difference from the 1D case is the spread of iodine charges, which has a standard-deviation of $\sim 0.2\,e$, roughly four times as large as the other atoms, and ranges over $\pm 0.5\,e$. However, the charge-neutral cell (the maximum system-total DDEC charge being $1 \times 10^{-6}\,e$) enforces the pairing of the iodine charges: the average of a system's pair of iodine charges has a more usual standard-deviation of $\sim 0.05\,e$, and is within one standard-deviation of neutrality. This leads to the second significant difference to the 1D case: while the caesium charge is $\sim 0.6\,e$ compared to $\sim 0.8\,e$ for the 1D case, almost all of that charge is transferred directly to the CNT, spread evenly over many nearly-neutral carbon atoms.

## 6.2 Coulombic Energy

In order to assess the significance of charge-transfer, we now investigate the associated Coulombic energy. We being by addressing the theoretical approach, before assessing various numerical methodologies.

### 6.2.1 Infinite alternating chain

First consider an infinite chain of alternating point charges of charge $+q$ and $-q$, each point charge separated from its neighbours by a distance $\Delta$. We would like to calculate the electric potential energy $U_E$ between one of these points (at $r$) and the

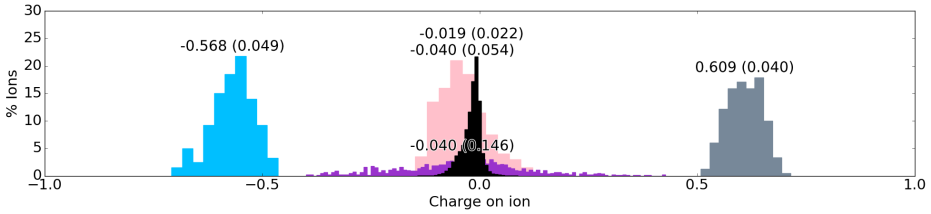


(a) Higher energy

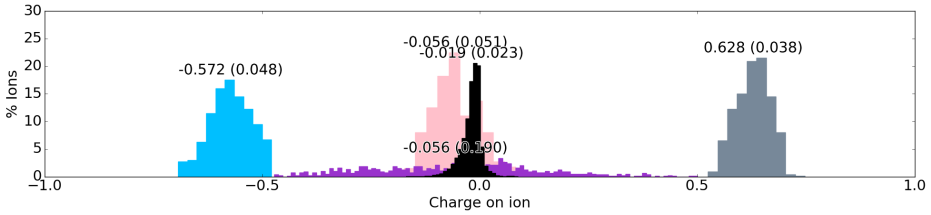


(b) Lower energy

Figure 6.11: DDEC charges for perturbations of the systems of Figure 6.10. As in Figure 6.8, silver represents the charge on caesium atoms, black represents carbon and purple iodine. The blue histogram represents the charge on the CNT per unit of CsI, while the pink histogram shows the system-average charge attributed to an iodine.

rest of the chain:

$$U_E(r) = k_e q \sum_i \frac{q_i}{r_i} \tag{6.2}$$

where $k_e$ is Coulomb's constant, $q_i$ is the charge of the $i$th neighbouring charge and $r_i$ is the (unsigned) distance between $r$ and point $i$.

If we assume our charge at $r$ is positive, then the positions of the negative charges are $(2n-1)\Delta$ and of the other positive charges $2n\Delta$ for all integers $n$.

Taking this into account:

$$U_E(r) = 2k_e q \left( q_+ \sum_{n=1}^{\infty} \frac{1}{2n\Delta} + q_- \sum_{n=1}^{\infty} \frac{1}{(2n-1)\Delta} \right) \tag{6.3}$$

where the factor of 2 takes into account that the infinite chain stretches in both directions.

Combining the sums, and assuming that $|q_+| = |q_-|$:

$$U_E(r) = \frac{2k_e q^2}{\Delta} \sum_{n=1}^{\infty} \left( \frac{1}{2n} - \frac{1}{(2n-1)} \right). \tag{6.4}$$

The Taylor expansion of $\ln(1+x)$ gives us the identity

$$\sum_{n=1}^{\infty} \frac{1}{2n^2 - n} = \ln(4) \tag{6.5}$$

and so

$$U_E(r) = \frac{2k_e q^2}{\Delta} \ln(2). \tag{6.6}$$

Suppose we now relax the assumption that $|q_+| = |q_-|$, and instead consider $q_1$ and $q_2$. Then instead of Equation (6.6) we have

$$U_E(r) = \frac{2k_e q_1}{\Delta} \sum_{n=1}^{\infty} \left( \frac{q_1}{2n} + \frac{q_2}{(2n-1)} \right). \tag{6.7}$$

The summand becomes

$$(q_1 + q_2)\frac{1}{2n-1} - (q_1)\frac{1}{4n^2 - 2n} \tag{6.8}$$

which converges only when $q_1 + q_2 = 0$.

### 6.2.2 Infinite conducting coaxial cylinders

Consider a infinite conducting uniformly-charged cylinder of radius $a$ surrounded by a similar coaxial thin cylinder of radius $b$. A section of the inner cylinder of length $L$ holds charge $+Q$, while the outer holds $-Q$.

Since this is a continuous charge distribution, we must use Gauss' Law:

$$\frac{Q_{\text{enc}}}{\epsilon_0} = \oiint \mathbf{E} \cdot \mathrm{d}\mathbf{a} \tag{6.9}$$

where $\epsilon_0$ is the permittivity of free space, $\mathbf{E}$ is the electric field and $Q_{\text{enc}}$ is the total charge contained within the Gaussian surface with infinitesimal area $\mathrm{d}\mathbf{a}$.

Consider a coaxial Gaussian surface of radius $r$ and length $L$. By symmetry $\mathbf{E} \cdot \mathrm{d}\mathbf{a} = E\,\mathrm{d}a$.

When $r > b$, $Q_{enc} = 0$ and so $E = 0$ everywhere. Inside the inner cylinder $E$ is also zero, since the charge on a conductor exists only on its surface. Otherwise, when $a < r < b$ $Q_{enc} = +Q$, giving:

$$E(r) = \frac{Q}{2\pi r L \epsilon_0} \tag{6.10}$$

and

$$V(r) = -\int_{\infty}^{r} E(r')dr' = \frac{-Q}{2\pi L\epsilon_0}\ln(r) \tag{6.11}$$

assuming that $V(\infty) = 0$.[1]

The potential difference is

$$\Delta V = V(b) - V(a) = -\frac{Q}{2\pi\epsilon_0 L}\ln\left(\frac{b}{a}\right). \tag{6.12}$$

This system is essentially a capacitor, with capacitance $C = Q/|\Delta V|$, and as such the electrical potential energy of the system is the energy required to charge it:

$$U_E = W = \int_0^Q |\Delta V| dq = \frac{1}{2}Q|\Delta V| \tag{6.13}$$

### 6.2.3 Analytic approximation

We now aim to calculate the Coulombic energy of a model of the 1D CsI@CNT system, with representative charges on Cs, I and CNT of 0.9, $-0.7$ and $-0.2\,e$ respectively. Since we need the alternating point charges to be equal for Equation (6.8) to converge, and we assumed equal charges on each cylinder in §6.2.2, we approximate the system as a superposition of alternating points with charge $\pm 0.8\,e$ and coaxial cylinders of charge $\pm 0.2\,e$. The Coulombic energy of our point-charges at a separation of 7.3 Å is therefore $\sim$1.75 eV per ion, or $\sim$21 eV for an system of 6 CsI units.

The radius of CNT we set to be 8 Å, and the length under consideration to be 15 Å. (The reasoning for such rough values will become clear shortly.) The choice of inner radius $a$ is not clear, a 1D line (taking the limit $a \to 0$) would cause a singularity in Equation (6.12). However, an upper bound might be taken to be the radius of the caesium ion, since it is the largest single ion radius. At $a = 2$ Å the Coulombic energy of the 'capacitor' system is only $\sim$50 meV, at 1 Å it has increased only to $\sim$80 meV. To reach a scale comparable to the energy of the alternating point charges the inner radius must approach the Planck length. We interpret this as meaning that the total Coulombic energy is dominated by the ions, and that the charge transfer to the walls has much less effect.

[1] It may seem unusual to use the logarithm of a physical quantity, which by itself has no physical meaning. However, these quantities can be usefully 'carried' in equations, similarly to imaginary numbers, provided that at some point they cancel out. For example, $\ln(1\,\text{Å})$ has no physical meaning, but $\ln(1\,\text{Å}) - \ln(2\,\text{Å})$ does. Equivalently, the quantity $A$ may be implicitly determined by a 'reference' quantity $A_0$, such that $\ln(A)$ should properly be thought of as shorthand for $\ln(A/A_0)$.

### 6.2.4 Numerical methods

We use the LAMMPS molecular dynamics simulator [Plimpton, 1995] to compute Coulombic interactions for the perturbed systems numerically. Its `ewald` Coulombic solver implements the standard Ewald summation method, which is described in detail in for example Frenkel and Smit [2001] but we provide an overview here.

We start with a system of $N$ points, each with charge $q_i$ and position $r_i$, in a unit-cell of volume $V$ and diameter $L$ (extension from the cubic case is trivial). The Coulombic potential energy is $U_E = 1/2 \sum_{i=1}^{N} q_i \phi(r_i)$, where the electrostatic potential $\phi(r_i) = \sum'_{j,\mathbf{n}} q_j / |r_{ij} + \mathbf{n}L|$. The sum over $\mathbf{n}$ is over all periodic images, the primed sum indicates that the $\mathbf{n} = 0$ case excludes a point's self-interaction.

In order to accelerate convergence of this sum, the Ewald scheme screens each delta-function point charge $q_i$ with a Gaussian charge distribution

$$\rho_{\text{Gauss}} = -q_i (\alpha/\pi)^{3/2} \exp(-\alpha r^2). \tag{6.14}$$

This allows the total Coulombic energy to be constructed from three terms, a screened local term

$$U_{\text{screened}} = 1/2 \sum_{i \neq j}^{N} q_i q_j \operatorname{erfc}(\sqrt{\alpha} r_{ij}) / r_{ij} \tag{6.15}$$

where erfc is the complementary error function, a Fourier treatment of the long-range smooth screening Gaussians

$$U_{\text{long-range}} = \frac{1}{2V} \sum_{\mathbf{k} \neq 0} \frac{4\pi}{k^2} |\rho(\mathbf{k})|^2 \exp(-k^2/4\alpha) \tag{6.16}$$

and a constant to remove the self-interaction between a point and its screening

$$U_{\text{self}} = (\alpha/\pi)^{1/2} \sum_i q_i^2 \tag{6.17}$$

such that $U_E = U_{\text{screened}} + U_{\text{long-range}} - U_{\text{self}}$. The screening of the point charges allows much faster convergence of the real-space expansion, and the smoothness of the screening Gaussians allows a quickly-converging Fourier expansion.

For a simple 1D periodic system of point charges of $\pm 1\,e$ with a 1 Å separation, Equation (6.6) predicts an energy of $-19.962\,15$ eV. Images in the 'non-periodic' dimensions are once more an issue: at a 'non-periodic' separation $L_{\text{np}}$ of 2 Å the Ewald summation is $-19.738\,32$ eV, only by $L_{\text{np}} = 10$ Å has the Ewald

summation converged to within 1 meV of the theoretical value. Our nanowire systems converge even slower, with separations of 50 Å required before convergence to the meV scale. At these separations the calculation is impractically slow for our systems; fortunately alternative solvers exist.

LAMMPS also includes an `MSM` solver, which implements the Multilevel Summation Method (MSM) of Hardy et al. [2009]. This maps atom charge to a 3D mesh and solves the short-range interactions directly before projecting onto progressively coarser grids with longer short-range cutoffs. The MSM method is considerably faster than the direct Ewald method, and also allows explicit control of periodicity. Using an explicit 1D periodicity, a force tolerance of $1 \times 10^5$ relative error, and a short-range cutoff of 40 Å (within which the Coulombic interaction is computed directly), the MSM method predicted the electric potential energy within 0.1 meV of the direct Ewald method, which itself only converges to that accuracy at a non-periodic separation of hundreds of Angstroms.

Figure 6.12 shows the electric potential energy of the systems of perturbed 1D CsI encapsulated in tubes of various radii and band gap. The energy centers around ∼20 eV, validating our statement in Section 6.2.3 that the ions dominate the Coulombic energy. The energy falls with increasing tube radius even for the larger tubes, since fixed charges have a lower energy when their separation increases.

## 6.3 Charge Prediction

The DDEC scheme is fairly computationally expensive, taking minutes to calculate charges from DFT-produced density fields which are themselves very expensive. We would like to use our existing results to build an interpolative model to predict these charges. Since we have established that the charge on an individual carbon atom is negligible, we focus here on predicting only the charge on filling ions.

One of the simplest descriptors of our system is the position of the ion within the tube. For the perturbed 1D system there are two measures which stand out: the radial distance from tube axis and the distance to the nearest carbon atom. Figure 6.13 shows simple linear, quadratic and cubic fits for these measures for Cs ions encapsulated in a (10-0) CNT. The mean fit error of the linear fit to tube axis is $0.0052\,e$, reducing to $0.0041\,e$ for the higher-order fits. The distance to the nearest carbon atoms performs slightly worse at $0.0058\,e$ and $0.0050\,e$ respectively.

This approach performs similarly well for different tubes and ions, but is not transferable between tube radii nor between filling structures.

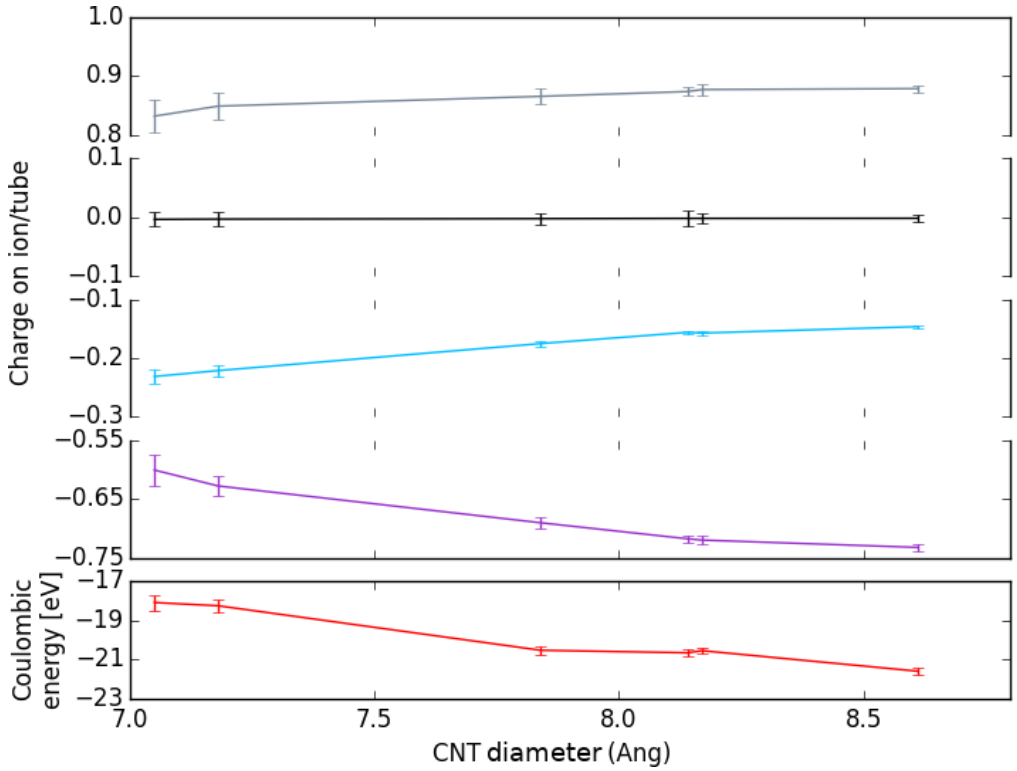


Figure 6.12: Top four graphs: DDEC charges assigned to atoms and nanotube of perturbed 1D CsI encapsulated in CNTs of different radii, see Figure 6.9 for detail. Bottom: Coulombic energy of $(CsI)_6$@CNT systems of DDEC point charges. Error bars show the standard deviation across 100 perturbed systems per CNT radius.

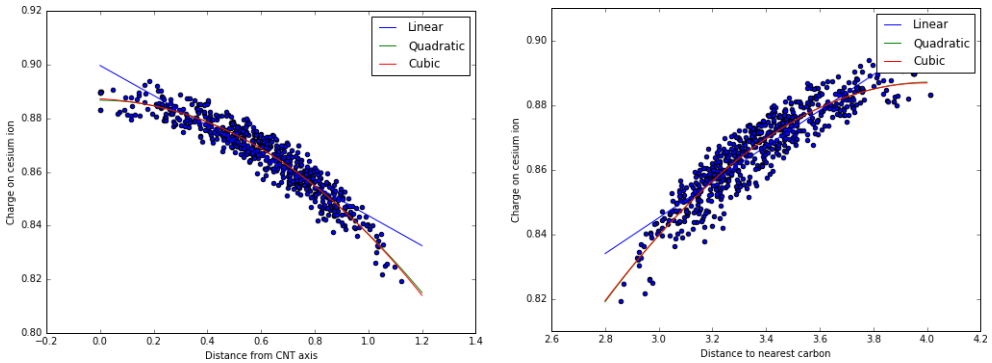


(a) (b)

Figure 6.13: Charge on Cs ions encapsulated in a (10-0) CNT with respect to radial distance from CNT axis (left) and distance to nearest carbon (right), with linear, quadratic and cubic least-squares fits.

### 6.3.1 SOAP charge-prediction

In order to create a transferable predictor of net atomic charge, we investigate the SOAP kernel of Bartók et al. [2013], with aim of predicting charge rather than the potential energy surface.

We generate SOAP descriptors for each caesium ion from each of 100 perturbed systems in each tube, 3600 descriptors in total, and calculate their DDEC charges. These are split into training as testing sets, and Gaussian Process Regression is performed on the data.

The charge predictions were converged to within $0.002\,e$ at a SOAP neighbourhood radius of 5 Å, though a value of 6 Å was chosen with a 0.5 Å cutoff skin.

In order to converge the SOAP descriptors with respect to $n_{\max}$ and $l_{\max}$ (discussed in Section 3.3.4), corresponding to numbers of radial functions and spherical harmonics respectively, a reference kernel matrix $K_{\text{ref}}$ of 100 arbitrary systems $\rho_i$ was created at high values of $n_{\max}$ and $l_{\max}$. Then, at any given $n_{\max}$ and $l_{\max}$ the same kernel matrix was created and the element-wise difference to the reference kernel was computed and averaged.

Figures 6.14a and 6.14b suggest that gains in accuracy of SOAP descriptors could be achieved up to $n_{\max} = 20$ and $l_{\max} = 15$. However, we used the default values of $n_{\max} = 40$ and $l_{\max} = 8$, since these provided satisfactory results. Even higher values of $n_{\max}$ and $l_{\max}$, corresponding to high-frequency basis functions, were prone to numerical problems, causing catastrophic failure.

The Gaussian Process Regression also requires convergence, with respect both to noise-variance $\sigma$ and to the size of the training set. Stratification is seen at poor values of either (see Figures 6.15a and 6.15b), where either the training samples are too sparse or their information is underutilised by a pessimistic value of $\sigma$. We find that 75 training samples are enough to predict the DDEC charge to within $0.004\,e$ (see Figure 6.15c), and a noise-variance of $1 \times 10^{-5}$ gives tight results without the overfitting seen in much lower values of $\sigma$.

## 6.4 Summary

In Figures 6.1a, 6.1b and 6.2 we see that significant charge is transferred between the crystal and tube, compared to the isolated component systems, in a manner dependent on the relative positions of encapsualted ions. This charge-density is simplified by the use of point-charges, where charge is partitioned and attributed to ions. Four such partitioning population-analysis schemes are explored here, and while the Hirshfeld and Mulliken exhibit their expected short-comings, the Bader

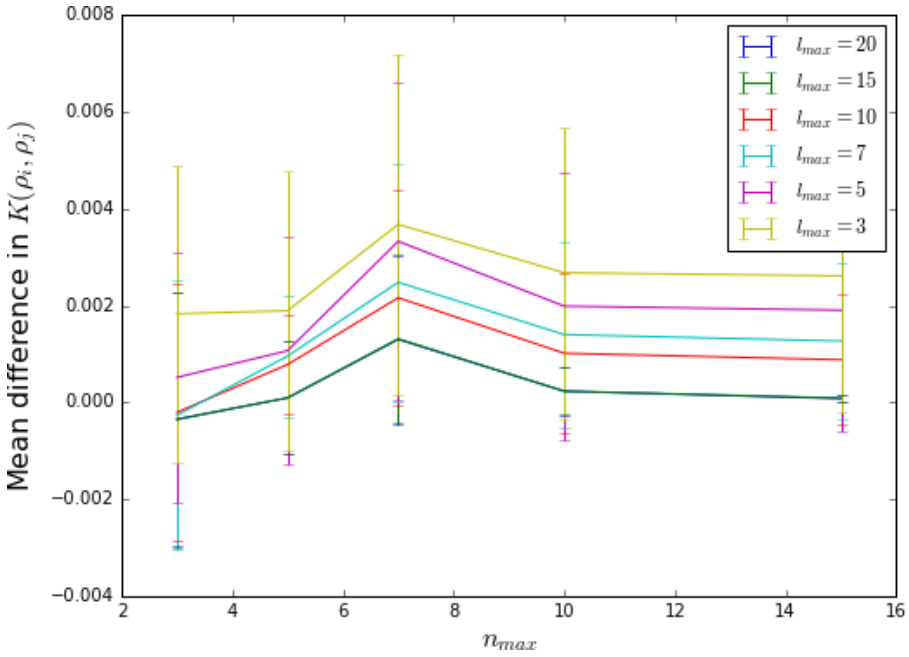


(a)

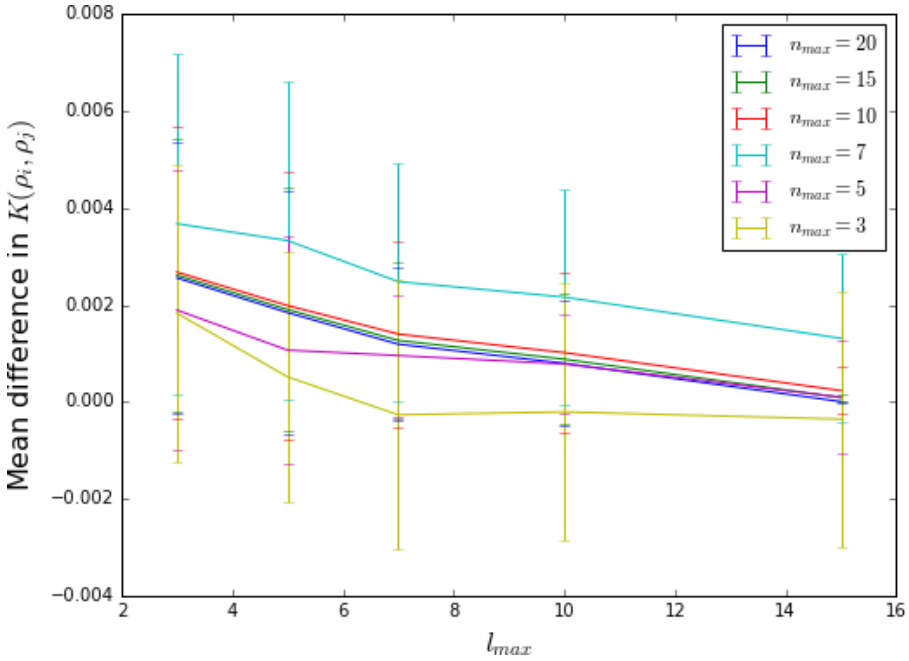


(b)

Figure 6.14: Average element-wise difference between a kernel matrix of 100 arbitrary systems and a reference kernel with $n_{\max} = l_{\max} = 20$. Error-bars show the standard deviation.

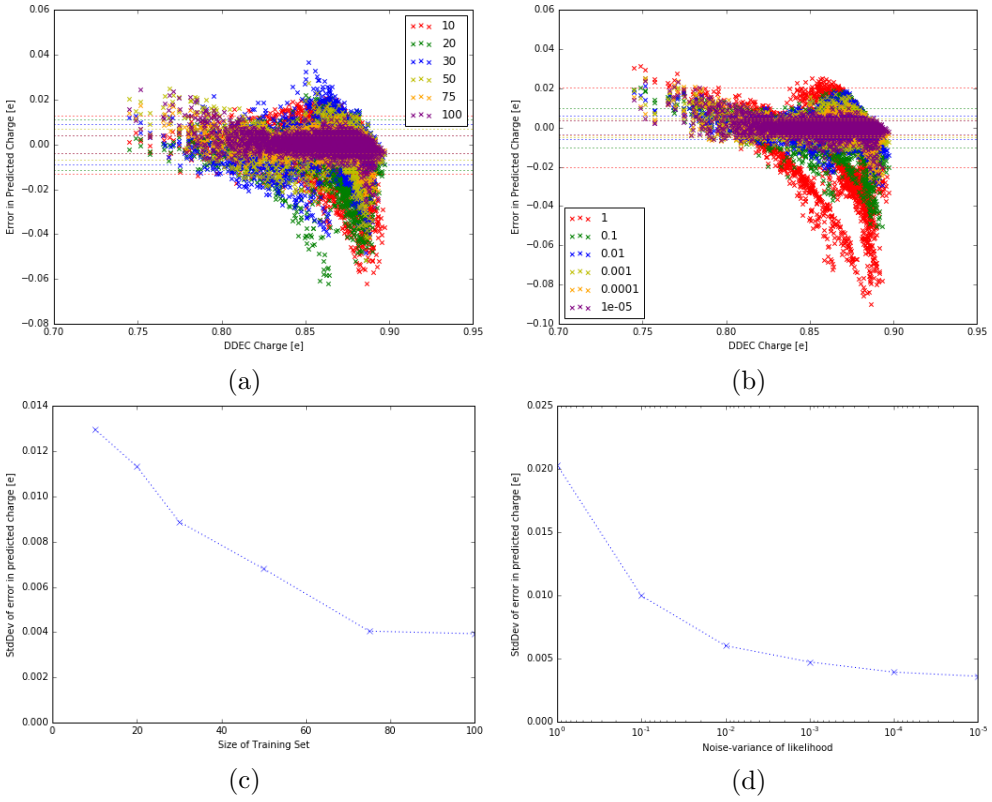


(a) (b)

(c) (d)

Figure 6.15: Error on the predicted charge of Cs ions inside CNTs of various size, with respect to the size of training set (left) and magnitude of noise-variance (right). Dotted lines in the top two scatter graphs show the standard deviation of the error, plotted in the bottom two graphs.

method (motivated by physical properties of the charge field) and DDEC method (motivated by reproducting the electrostatic-potential) independently produce the same physically-sensible values. Since the DDEC method is the more reliable of the latter two, it is chosen to represent the charge on ions and tube in our analysis.

We see in Figure 6.9 that the charge transfer both from core to tube and between core ions is dependent on the tube radius, with $\sim 0.2\,e$ being tranferred to tubes of diameter $\sim 7\,\text{Å}$, reducing at larger diameters but still significant at $\sim 9\,\text{Å}$. While the charge on the tube as a whole is significant, it is spread over many carbon atoms whose charge is nearly negligible. Most of this charge is donated by the iodine atoms, and in general both caesium and iodine ionic charges vary significantly from their formal charge, with the charge on the iodine ions in the thinnest tubes nearly half its formal charge. These results were seen both for 1D chains of encapsulated CsI and for more complex structures discovered via AIRSS.

The Coulombic energy of these systems is examined, both analytically (by modelling the system as alternating chains superimposed on capacitative coaxial cylinders) and numerically (using Ewald summation and the Multiscale Summation Method). The comparison of the two methods shows that, for reasonable radii of inner coaxial cylinder, the energy of the system is dominated by the ionic (rather than capacitative) contribution.

The charge on the tube is spread evenly over nearly-neutral carbon atoms, and so the most effective method of tube-charge prediction (for, say, an implicit model encapsulating tube) is to predict the much-larger ionic charges and attribute the remainder to the tube. To this end we examine interpolative models which take into account the tube-radius and ion-positions. Linear and quadratic fits to the distance from tube axis are very effective (with an error of thousandths of $e$), but not transferrable between tubes nor filling structures. However, by training a SOAP kernel on 100 systems from 6 tubes a model is created whereby charge on filling ions (and therefore on the tube) can be predicted by the ions' local environment to within $0.004\,e$ across all examined tubes.

Having addressed the issue of charge-transfer, and having built an interpolative model of radius-dependent charges, we now proceed to investigate the energetics of filling with a view to determining at which tube-radii filling can sensibly be expected to occur.

# Chapter 7

# Energetics of Filling

So far we have investigated properties which depend on the radius of the encapsulating nanotube. It is therefore necessary to have some idea of the radii of tubes at which filling can sensibly be expected to occur. Experiment can be useful, since theory must agree that filling of observed systems (for example Sloan et al. [2002a] report on $2 \times 2 \times 2$ KI crystals forming within a 1.4 nm SWNT, and $3 \times 3 \times 2$ crystals forming in 1.6 nm SWNTs) must be energetically-favourable at the temperatures and pressures used for system formation. However, the absence of experimental evidence does not necessarily indicate the inverse, and indeed it may be possible to predict systems which would form in heretofore unattempted conditions.

### 7.0.1 Internal-energy differences

We begin by investigating the energy cost of filling, calculating the difference between the DFT energies of the nanowire system and of its component parts. This provides only zero-temperature energies, and does not include any entropic contributions to the Gibbs free energy per particle. However, since $pV$ contributions are negligible for solids at reasonable pressures, it is a standard approach to approximate the Gibbs free energy by the DFT internal energy (see for example Hine et al. [2009]).

Using the perturbed 1D chain of CsI encapsulated in the CNTs of Chapter 6, we find a range of $E_{\text{filled}}$ for each tube radius. The energy of the tube $E_{\text{empty}}$ is calculated using the same parameters as the filled tube, detailed in Chapter 6. The nanowire used to calculate $E_{\text{empty}}$ was modelled at the same supercell as used in the filled simulations, to avoid any numerical issues arising from $k$-point differences.

The energy of the unencapsulated core material is very dependent on the reservoir in which it exists. A variety of such reservoirs were modelled: the usual

rocksalt CsI bulk, the CsCl-structure bulk, the ideal 1D CsI wire, isolated atoms of caesium and iodine, isolated iodine diatomic molecules and isolated CsI diatomic molecules.

The bulk structures were relaxed after the application of small positional noise. A cutoff energy of 500 eV was used, and the $k$-points were arranged as a Monkhorst-Pack grid with maximum spacing of 0.03 $Å^{-1}$, which converged the final energy to ~1 meV per atom. The same standard CASTEP-8 on-the-fly (OTF) PBE pseudopotentials were used as in the perturbed CsI@CNT simulations. The atomic systems were simulated in boxes of side-length 20 Å, which was well-converged, and a single $k$-point. All other parameters were the same as for the bulk calculations. The $I_2$ and CsI diatomic molecules were simulated as atomic systems, after the relaxation of the bond-length. Their energy as a function of bond-length is plotted in Figure 7.2.

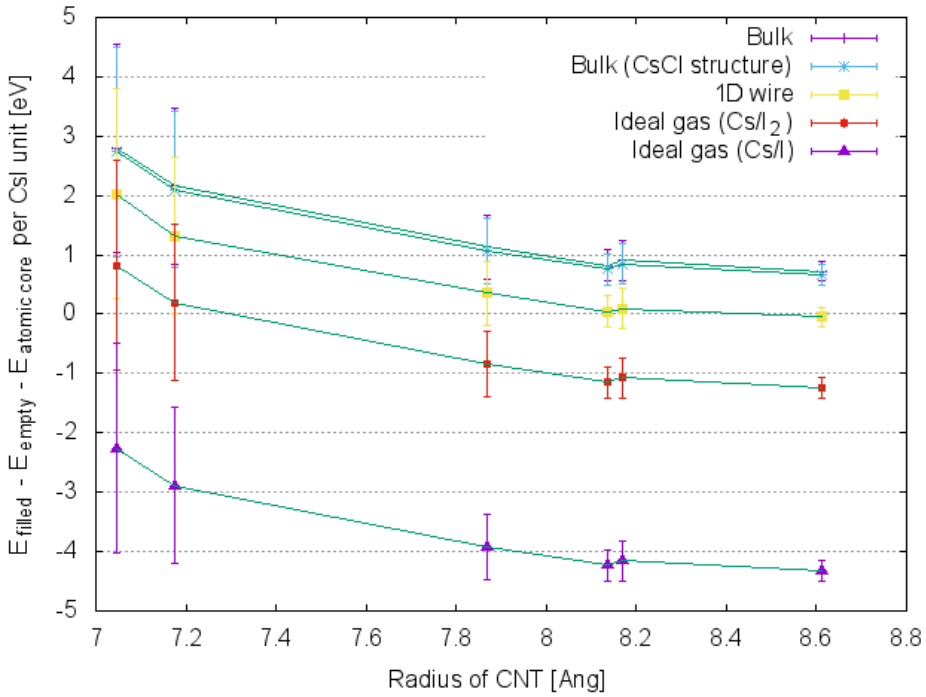


Figure 7.1: Energy cost of filling CNTs with perturbed 1D CsI wires. Entropic terms are not included. Each line represents the use of a different CsI reservoir. Error bars show standard-deviation of sets of 100 perturbed systems.

Figure 7.1 shows a clear decrease of filling-cost with increasing CNT radius. The spread decreases, which is also seen in the charge-tranfer (see Figure 6.9), due to an equal perturbation being proportionally larger at smaller radius. However, the choice of reservoir dominates the energy-cost of filling, with different choices

predicting all, some or none of the tubes to be filled. Note that the cost of filling for the larger radii tends to zero when the 1D wire is chosen as reservoir, this highlights that the difference between reservoir energies is simply the relative formation energies of those reservoirs.

Experimentally, tubes are often filled via capillary action [Hong et al., 2010] or sublimation [Senga et al., 2014], at significant temperatures. While the melting point of caesium iodide at atmospheric pressure is 894.2 K, carbon nanotubes have been filled by CsI sublimed *in vacuo* at 820 K [Senga et al., 2014, Suppl. Inf.], and vaporisation can be observed even at 753 K [Venugopal et al., 1985].

| Material | Melting Point | Boiling Point |
|---|---|---|
| Cesium | 301.6 | 944 |
| Iodine | 386.8 | 457.4 |
| CsI | 894.2 | 1,553 |

Table 7.1: Melting and boiling points of CsI, Cs and I, in degrees Kelvin, at atmospheric pressure.

Ignoring the entropic terms is therefore no longer a viable option, since gas or liquid reservoirs are the most realistic, which have significant $pV$ and thermal energy contributions. We must, therefore, consider the chemical potential of the fillings. The liquid chemical potential is complex, and we shall not deal with it here beyond bounding it between the ideal-gas and solid chemical potentials. We proceed to quantify the entropic contributions to the gaseous CsI reservoir.

## 7.1 Chemical potentials

### 7.1.1 Monatomic ideal gas

We begin by treating both Cs and I as separate monatomic ideal gases. The partition function of a single ideal gas particle is

$$\begin{aligned} Z_1(V,T) &= \frac{1}{(2\pi\hbar)^3}\int \exp[-\beta H(\mathbf{x},\mathbf{p})]\,\mathrm{d}\mathbf{p}\,\mathrm{d}\mathbf{x} \\ &= \frac{1}{(2\pi\hbar)^3}\int \exp[-\beta \mathbf{p}^2/2m]\,\mathrm{d}\mathbf{p}\,\mathrm{d}\mathbf{x} \\ &= V\left(\frac{mk_BT}{2\pi\hbar^2}\right)^{\frac{3}{2}} = \frac{V}{\lambda^3}. \end{aligned} \tag{7.1}$$

where $V$ is the volume within which the particle is bounded. $\lambda$ is defined as the "thermal wavelength" of the particle, dependent on constants $(k_B, 2\pi\hbar)$, intrinsic

particle properties (mass $m$), and the temperature $T$ of the system.

The partition function of a monatomic ideal gas of $N$ particles is $Z_{mon} = Z_1^N/N!$, the Helmholtz free energy is $F = -k_B T \ln(Z_{mon})$ and the chemical potential is

$$\mu = \left(\frac{\partial F}{\partial N}\right)_{V,T} = k_B T \ln\left(\frac{\lambda^3 N}{V}\right). \tag{7.2}$$

### 7.1.2 Diatomic ideal gas

Iodine often exists in its diatomic form, and so we proceed to calculate the chemical potential of diatomic ideal gases, largely following the approach of Murray [2006]. The case of diatomic ideal CsI gas is also addressed. The partition function for a single diatomic molecule is

$$Z_1 = Z_{tr} Z_{rot} Z_{vib} \tag{7.3}$$

The translational partition function is that of a monatomic ideal gas, see Equation (7.1). Since the mass $m$ of the $I_2$ molecule is $2 \times 126.9\,\mathrm{u}$ and that of diatomic CsI is $(126.9 + 132.9)\mathrm{u}$ we have

$$Z_{tr} = V(\alpha_{tr} T)^{\frac{3}{2}} \tag{7.4}$$

where $\alpha_{tr,I_2} = 8.327 \times 10^{19}\,\mathrm{m^{-2}\,K^{-1}}$ and $\alpha_{tr,CsI} = 4.361 \times 10^{19}\,\mathrm{m^{-2}\,K^{-1}}$.

The rotational partition function [Spencer and Moore, 2001] is

$$Z_{rot} = \sum_l (2l+1) \exp\left[-\beta(\hbar^2/2I)[l(l+1)]\right] \tag{7.5}$$

where $I = \mu r^2$, $\mu = (m_1 m_2)/(m_1 + m_2)$ and $r$ is the bond-length. For $I_2$ $\mu = m_I/2$ and $r = 267\mathrm{pm}$ (see Figure 7.2a and references in Table 7.2) so $I_{I_2} = 7.51 \times 10^{-45}\,\mathrm{kgm^2}$. For CsI $r = 332\mathrm{pm}$ (see Figure 7.2b and Story [1976]) so $I_{CsI} = 1.188 \times 10^{-44}\,\mathrm{kgm^2}$.

When $T >> \Theta_r = \hbar^2/(2k_B I) \approx 0.05\mathrm{K}$ this reduces to

$$Z_{rot} = \frac{2Ik_B T}{\sigma \hbar^2}. \tag{7.6}$$

For molecular iodine we must consider its rotational symmetry $\sigma$: a rotation of 180° exchanges two identical nuclei, and so we must divide $Z_{rot,I_2}$ by a symmetry factor $\sigma = 2$ to avoid double-counting [Capitelli et al., 2011]. Thus

$$Z_{rot} = \alpha_{rot} T \tag{7.7}$$

where $\alpha_{rot,I_2} = 9.325\,\mathrm{K}^{-1}$ and $\alpha_{rot,CsI} = 29.5\,\mathrm{K}^{-1}$.

The vibrational partition function [Spencer and Moore, 2001] is

$$Z_{vib} = \frac{1}{1 - \exp(-\beta\hbar\omega)} \tag{7.8}$$

The stretching mode of iodine is very dependant on environment. Kaiho [2014] gives the spectroscopic wavenumber $\bar{\nu}$ of the stretching mode to be $180\,\mathrm{cm}^{-1}$ for solid $I_2$, a range of $140\,\mathrm{cm}^{-1}$ to $210\,\mathrm{cm}^{-1}$ in the presence of adducts, and variously $167\,\mathrm{cm}^{-1}$, $202\,\mathrm{cm}^{-1}$ and $205\,\mathrm{cm}^{-1}$ in solutions of pyridine, ethanol and benzine. McNaught [1980] gives $\bar{\nu}$ for infinitesimal amplitudes of vibration of molecular iodine as $214\,\mathrm{cm}^{-1}$. Walmsley and Anderson [1964, p.414] give $\bar{\nu}$ for iodine in the gas phase as $215\,\mathrm{cm}^{-1}$, and $211\,\mathrm{cm}^{-1}$ in the crystal. Nash [2001] calculates, via the *Hyperchem* program, $\bar{\nu}$ to be $255\,\mathrm{cm}^{-1}$.

The DFT calculation of an $I_2$ molecule subject to bond-stretching described above is shown in Figure 7.2a. A parabolic fit of the minimum gives the force constant to be $10.81\,\mathrm{eV\AA}^{-2}$, which via $k = 4\pi^2 c^2 \mu \bar{\nu}^2$ gives a spectroscopic wavenumber of $215\,\mathrm{cm}^{-1}$, agreeing with Walmsley and Anderson [1964] and McNaught [1980].

| Source | Vibrational Frequency $\mathrm{cm}^{-}1$ |
|---|---|
| McNaught [1980] | 214 |
| Walmsley and Anderson [1964] | 215 |
| Nash [2001] | 255 |
| DFT | 215 |

Table 7.2: Vibrational frequencies of the stretching mode of an iodine diatomic molecule.

Using a value of $215\,\mathrm{cm}^{-1}$ for the vibrational frequency gives $\hbar\omega = hc\bar{\nu} = 26.7\,\mathrm{meV}$. The equivalent values for diatomic CsI are $k = 2.982\,\mathrm{eV\,\AA}^{-2}$, $\nu = 119\,\mathrm{cm}^{-1}$ (agreeing with Honerjäger and Tischer [1974]) and $\hbar\omega = 14.8\,\mathrm{meV}$.

There is a "turn-on" temperature $\Theta_v = \hbar\omega/k_B \approx 310\mathrm{K}$ for $I_2$ and $\approx 170\,\mathrm{K}$ for CsI, such that Equation (7.8) reduces to:

$$Z_{vib} = \begin{cases} 1 & \text{if } T << \Theta_v \\ k_B T/\hbar\omega = \alpha_{vib} T & \text{if } T >> \Theta_v \end{cases} \tag{7.9}$$

where $\alpha_{vib,I_2} = 3.20 \times 10^{-2}\,\mathrm{K}^{-1}$ and $\alpha_{vib,CsI} = 5.82 \times 10^{-3}\,\mathrm{K}^{-1}$.

When $T >> \Theta_{vib}$ (i.e. $Z_{vib} = \alpha_{vib} T, Z_{rot} = \alpha_{rot} T$), by Stirling's approxima-

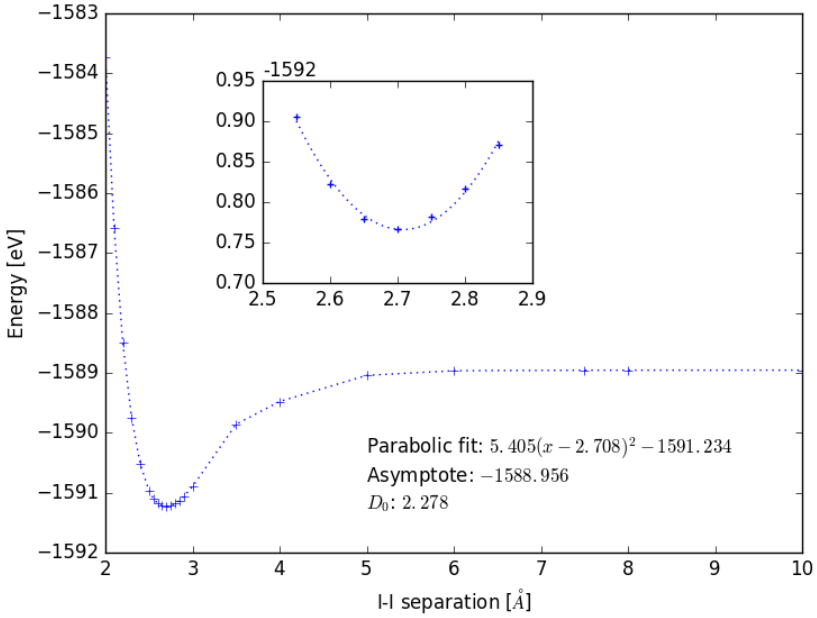


(a) Iodine

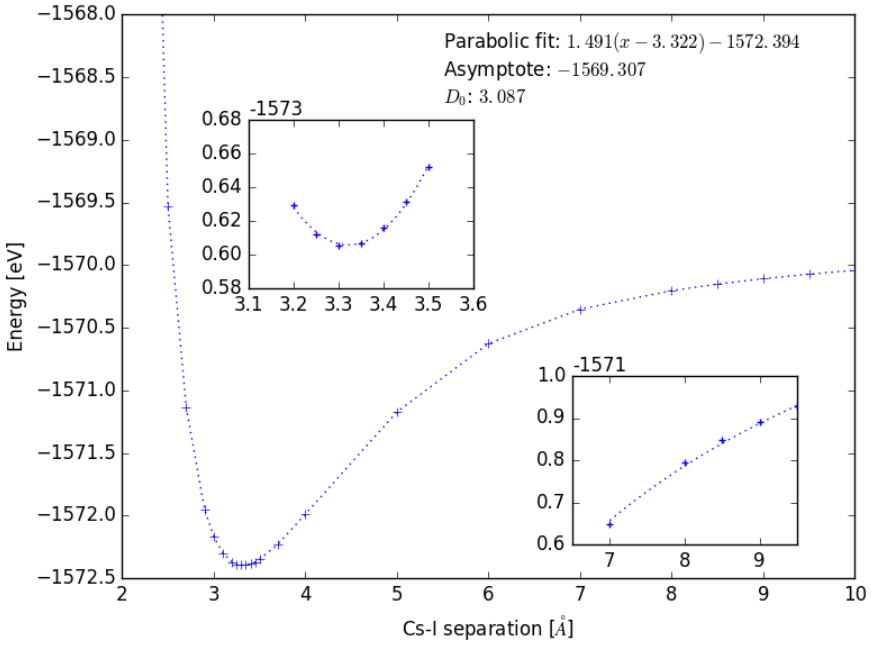


(b) Cesium iodide

Figure 7.2: Change in energy of an iodine diatomic molecule (top) and CsI molecule (bottom) with bond length. Right inset of the bottom graph shows long-range behaviour, with $1/r$ fit. Other insets show the region around the minimum, with parabolic fit. Dotted line in the main graph is to guide the eye.

tion:

$$F = k_B T N_{\text{dimers}} \left( \ln(N_{\text{dimers}}) - \ln(V) - \frac{7}{2} \ln(k_B T) - \sigma \right) \tag{7.10}$$

where $\sigma$ relies only on properties of the dimeric molecule:

$$\sigma = 1 + \frac{3}{2} \ln \left( \frac{2m\pi}{h_0^2} \right) + \ln \left( \frac{2I}{S\hbar^2} \right) + \ln \left( \frac{1}{\hbar\omega} \right). \tag{7.11}$$

If we restrict ourselves to measuring all quantities in S.I. units, we have $\sigma_{I_2} = 249$ and $\sigma_{CsI} = 251$.

Finally the chemical potential is

$$\mu = \left( \frac{\partial F}{\partial N_{\text{dimers}}} \right)_{V,T} \tag{7.12}$$

$$= k_B T \left( \ln(N_{\text{dimers}}) - \ln(V) - \frac{7}{2} \ln \left( \frac{1}{\beta} \right) - \sigma + 1 \right) \tag{7.13}$$

### 7.1.3 Ideal gas mixtures

The chemical potential of an ideal gas in mixture is the same as the chemical potential of the pure gas, except evaluated at its partial pressure in the mixture [Spencer and Moore, 2001].

$$\mu_i(P, T, X_i) = \mu_i'(P' = X_i P, T, X_i' = 1) \tag{7.14}$$

where $X_i$ is the molar fraction of an ideal gas $i$ such that $P_i/P_{tot} = N_i/N_{tot} = X_i$. Treating gaseous CsI as a mixture of an ideal dimeric gas of $I_2$ and an ideal atomic gas of Cs, we can use the partial pressures $P_{Cs}$ and $P_{I_2}$ to calculate a total chemical potential $\mu_{Cs+\frac{1}{2}I_2}$.

For a constant stochiometry of CsI, $N = N_{tot} = N_{Cs} + N_{I_2} = 3N_{I_2}$ and so

$$P_{I_2} = P_{tot} X_{I_2} = \frac{P_{tot}}{3} \qquad P_{Cs} = P_{tot} X_{Cs} = \frac{2P_{tot}}{3}. \tag{7.15}$$

Since we are treating Cs as an atomic ideal gas (*i.e.* using Equation (7.1), *not* using the partial volume $V_{Cs} = V_{tot} X_{Cs}$), we arrive at the standard result that

$$\mu_{Cs}(T, P, X_{Cs}) = \mu_{0,Cs} + k_B T \ln(X_{Cs}) \tag{7.16}$$

and $\mu_{I_2}(T, P, X_{I_2})$ follows similarly.

Combining these:

$$\mu_{Cs+\frac{1}{2}I_2}(T,P) = \mu_{Cs}(T,P,X_{Cs}) + \frac{1}{2}\mu_{I_2}(T,P,X_{I_2}) \tag{7.17}$$

$$\begin{aligned} &= \left[k_B T \ln\left(\frac{\lambda_{Cs}^3 N_{Cs}}{V}\right) + k_B T \ln(2/3)\right] \\ &+ \left[\frac{1}{2}k_B T\left(\ln(N_{I_2}) - \ln(V) - \frac{7}{2}\ln\left(\frac{1}{\beta}\right) - \sigma_{I_2} + 1\right) + \frac{1}{2}k_B T \ln(1/3)\right] \\ &= k_B T\left(\frac{3}{2}\ln\frac{N}{V} + \frac{13}{4}\ln\beta - \frac{\sigma_{I_2}}{2} + \frac{3}{2}\ln\frac{2\pi\hbar^2}{m_{Cs}} + \frac{1}{2} - \ln\frac{3}{2} + \ln 2 - 2\ln 3\right). \end{aligned} \tag{7.18}$$

Restricting to SI units:

$$\mu_{Cs+\frac{1}{2}I_2}(T,P) = k_B T\left(\frac{3}{2}\ln\frac{N}{V} + \frac{13}{4}\ln\beta + 19.4\right) \tag{7.19}$$

### 7.1.4 Einstein solid

Since we are calculating the chemical potentials of the gaseous reservoirs at non-zero temperatures, we must also take into account the entropic energy of the encapsulated filling. The entropic behaviour of the CNT should properly be addressed as well, but we assume that the chemical potentials of carbon in empty and filled CNTs cancel out. We assume that the filling ions are constrained to vibrate in three dimension around fixed points, *i.e.* they are modelled as simple harmonic oscillators. The partition function of a single such ion's vibration in 1D is

$$Z^{(1)}_{\text{1D Einstein}} = \sum_{n=0}^{\infty} \exp\left[-\hbar\omega(n+1/2)\beta\right] \tag{7.20}$$

and the chemical potential is

$$\mu^{(1)}_{\text{1D Einstein}} = k_B T \ln(1 - \exp(-\hbar\omega\beta)). \tag{7.21}$$

As in the case of the diatomic ideal gas, the total partition function is simply the product of partial partition functions, and so $Z^{(1)}_{\text{3D Einstein}} = Z^{(1)}_x Z^{(1)}_y Z^{(1)}_z$. In our case symmetry reduces this to $Z^{(1)}_l (Z^{(1)}_t)^2$, where $Z_l$ and $Z_t$ correspond to longitudinal and transverse perturbations.

In order to calculate $\hbar\omega$, the perfect $(CsI)_6$ chain was simulated, and single

ions were perturbed in longitudinal and transverse directions. The energy was measured as a function of perturbation and fit to a quadratic, giving a spring-constant from which the frequency follows using $\omega = \sqrt{k/m}$. The transverse and longitudinal frequencies for perturbation of the iodine atom give $\hbar\omega$ of 1.58 meV and 5.64 meV respectively, the equivalent values for the caesium atom are 1.53 meV and 5.14 eV.

### 7.1.5 Total enthalpy

We can now include enthalpic contributions to the reservoirs and filling, using the fact that the partition function of an ideal gas of $N$ particles is $Z_N = Z_1^N/N!$, the Helmholtz free energy is $F = -k_B T \ln(Z_N)$ and the chemical potential is $\mu = (\partial F/\partial N)_{V,T}$. Figure 7.3 shows that even here the difference between reservoirs is significant. In particular, the proportion of dissociated iodine would make the difference between filling only those tubes wider than 8 Å in radius, or filling tubes even narrower than 7 Å in radius. We must therefore calculate the ratio of dissociated iodine in our expected filling conditions.

With knowledge of the usual setup for filling experiments, we can create an estimate of the conditions. A usual setup consists of 10 mg CsI ($4.6 \times 10^{19}$ atoms) inside a quartz tube of internal diameter 5 mm and length 100 mm, giving a number density of $2.3 \times 10^{25}\,\mathrm{m}^{-3}$. (By comparison, an ideal gas at 0 °C and 1 atm has number density $2.7 \times 10^{25}\,\mathrm{m}^{-3}$). Excepting the few mg of CNT, the tube otherwise contains vacuum.

## 7.2 Dissociation

While iodine gas is diatomic at room temperature and pressure, at low density it begins thermally dissociating at around 700 K. DeVries and Rodebush [1927] observe that at number-densities $\sim 10^{21}\mathrm{m}^{-3}$ by 732 K it is 17.8% dissociated, by 823 K it is 50.4% dissociated and dissociation reaches 80% by 898 K.

We wish to compare our DFT simulations to experimental values. Figure 7.2b shows the energetic behaviour of a caesium-iodide diatomic molecule as a function of bond-length, given by a DFT calculation converged as described above to ∼1 meV. The atoms are charged at the maximum distance simulated, yet their charge is converged, allowing a $1/r$ fit to extrapolate the long-range behaviour. The DFT dissociation energy $D_0$ of 3.087 eV is close to the value given by NIST data [Darwent, 1970] of 3.27 eV at 0 K and 3.31 eV at 298 K.

However, the DFT dissociation energy $D_0$ of an $I_2$ molecule (see Figure 7.2a) of 2.278 eV compares unfavourably with NIST data [Darwent, 1970], which gives the

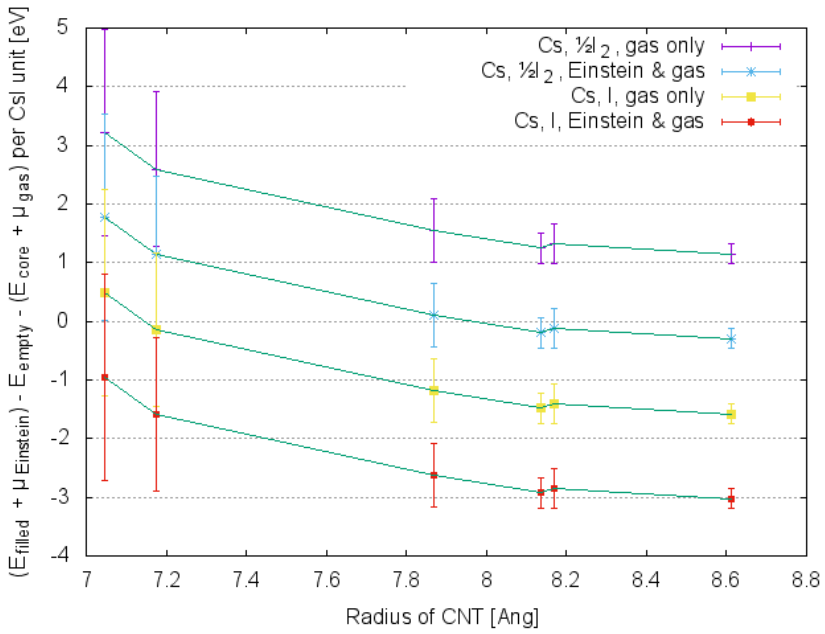


Figure 7.3: Enthalpy cost of filling CNTs with perturbed 1D CsI wires, calculated at 820 K, the temperature of the sublimation filling of Senga et al. [2014] and a number density of $2.3 \times 10^{25}\,\mathrm{m}^{-3}$. Error bars show standard-deviation of sets of 100 perturbed systems.

dissociation energy of diatomic iodine as 1.544 eV at 0 K and 1.567 eV at 298 K. By default CASTEP assumes that the densities of spin-up and spin-down electrons are equivalent for systems with an even number of electrons (such as diatomic iodine), and simply doubles the population of spin-unpolarised bands. Lifting this constraint lowers $D_0$ by $\sim$70 meV, since the ground-state of diatomic iodine has a non-zero magnetic moment. DFT also neglects the effects of van der Waals (dispersion) interactions [Grimme, 2011]. Applying the semi-empirical dispersion correction of Tkatchenko and Scheffler [2009] lowers $D_0$ by $\sim$10 meV. Both corrections still leave a large discrepancy, and the correction for the zero-point energy is similarly negligible. However, Olsen and Thygesen [2013] perform similar atomisation experiments to find PBE overbinds fluorine by 0.6 eV, similar to the overbinding seen here. They find that the random phase approximation (RPA) exchange-correlation functional corrects the DFT to within 0.4 eV, and their modification to the adiabatic local density approximation (LDA) exchange-correlation functional is correct to within 50 meV. Both functionals are higher up the "Jacob's ladder" hierarchy of Perdew [2001], and as such have poor computational scaling. Since we have much better agreement with literature for the CsI diatomic molecule and bulk properties (and

also the near-equilibrium behaviour of the $I_2$ molecule) we continue to use the PBE functional for our DFT calculations, conceding to using the experimental values for iodine dissociation.

As shown in Figure 7.4, the predicted dissociation temperature of diatomic iodine is ∼1800 K and of diatomic CsI is ∼5000 K, both above any realistic filling temperature due to destruction of the CNTs (multiwall CNTs (MWCNTs) have been observed by Mahajan et al. [2013] to remain stable in argon-rich atmosphere up to 1600 K). We can therefore assume the CsI gas to be entirely diatomic, and any excess gaseous iodine to also be entirely diatomic.

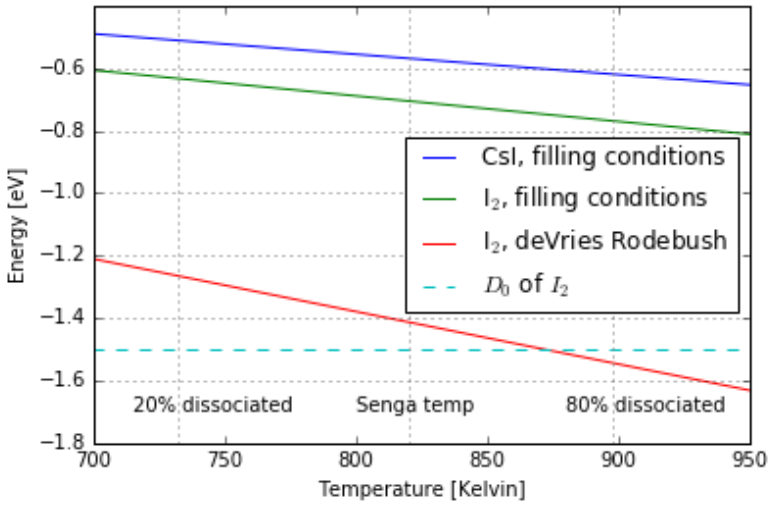


Figure 7.4: Difference between $I_2$ chemical potential and twice the I chemical potential, varying with temperature, for the densities in the work of DeVries and Rodebush [1927] and for estimated filling densities. Also shown is the difference between the diatomic CsI chemical potential and those of its component atoms at estimated filling densities. The difference at the DeVries-Rodebush conditions crosses the dissociation energy (∼1.5 eV) in the region expected. Extrapolation of the 'filling conditions' lines predicts iodine dissociation at ∼1800 K and CsI dissociation at ∼5000 K. The 'Senga' temperature is that used for CsI sublimation filling in the work of Senga et al. [2014].

## 7.3 Required thermal and density filling conditions

With the knowledge of the gaseous reservoir, we now proceed to examine the energetics of filling with respect to temperature, at the estimated filling densities. Figure 7.5 shows that at higher temperatures tubes are *less* likely to be filled, de-

spite the higher pressure these temperatures imply. We also see that a radius of 7.8 Å appears to be the cutoff for filling at these densities.

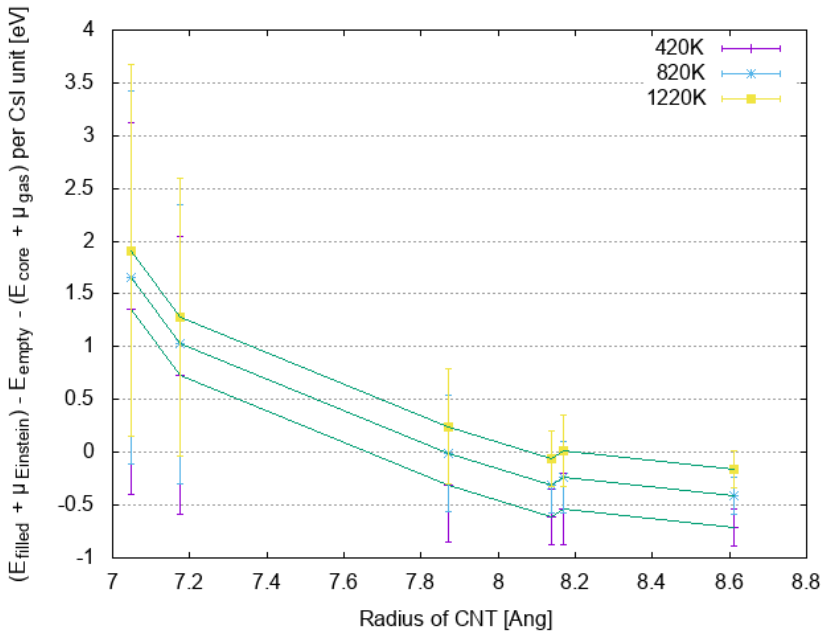


Figure 7.5: Enthalpy cost of filling CNTs with perturbed CsI wires at various temperatures and at the estimated filling number density of $2.3 \times 10^{25}\,\mathrm{m}^{-3}$, using the diatomic gaseous CsI reservoir.

The other way of increasing the gas pressure is to increase the gas density. By using 100 mg of filling material, rather than the usual 10, filling becomes 0.12 eV more favourable at 420 K, and 0.15 eV more favourable at 1220 K. This is considerably less effective than changing temperature, and relies on the assumption that all material would sublime at the temperature used.

In any case, it seems that significantly narrower tubes cannot be filled merely be altering the filling conditions; even a 1 Å difference in radius requires order-of-magnitude difference in density or temperature, likely preventing filling at all. An alternative method of greatly increasing the gas pressure, perhaps by altering the volume of the system, may be more promising.

## 7.4 Assessment of previous octopolar KI systems

The approach described above was carried out again with potassium iodide, in order to assess the CNT radii used in Chapter 5. DFT calculations were used to investigate the energy of diatomic KI as a function of bond-length, with the same

| | (8-8) | | (14-0) | |
|---|---|---|---|---|
| | K | I | K | I |
| axial | 2.92 | 1.71 | 2.74 | 1.83 |
| cross-section y | 1.20 | 1.13 | 0.87 | 1.04 |
| cross-section z | 1.18 | 1.25 | 0.80 | 1.05 |

Table 7.3: Values of vibrational energy $\hbar\omega$ in meV for Einstein solids corresponding to the equilibrium encapsulated octopolar KI structures of Chapter 5. Cross-sectional values are not quite equal since the lines of symmetry do not coincide perfectly with the Cartesian axes.

parameters as used in Chapter 5 (namely, a cutoff energy of 1000 eV, the same PBE PPs, a grid-scale of 2 and fine-grid-scale of 2.5, at the Γ-point). The equilibrium bond-length was found to be 3.051 Å and $\hbar\omega$ to be 22.38 meV, in agreement with the experimental values of 3.048 Å and 23.13 meV found by Honig et al. [1954]. The same $1/r$ extrapolation was required as for the CsI case. The dissociation energy was found to be 3.189 eV, whereas the experimental NIST value is 3.34(13) eV [Darwent, 1970]. These values lead to a molecule-specific constant of $\sigma = 251$. Assuming the same filling conditions (10 mg KI in a quartz tube of length 100 mm and internal diameter 5 mm) the KI dissociation temperature is ∼7000 K, and so we again assume an ideal gas of diatomic molecules.

The Einstein solid chemical potential must also be recalculated. In this instance, the equilibrium structure depends on the radius of the encapsulating CNT, and so we must calculate the vibrational behaviour around equilibrium for each system. The loss of symmetry requires each Cartesian direction to be investigated separately, but enough symmetry remains in the case of octopolar filling for each species to have only one symmetry-reduced location. The values of $\hbar\omega$ for certain crystals are listed in Table 7.3, calculated via the same harmonic approximation of near-equilibrium perturbation.

For the tubes examined here, of chirality (8-8) and (14-0) with radii 10.8 Å and 10.2 Å respectively, we find that filling is favourable in both cases by ∼4 eV per KI unit. More precisely, the favourability of the (8-8) tube filling at 820 K with 10 mg of material is 3.96 eV, increasing only to 3.99 eV at 420 K and with 10 times as much material, decreasing to 3.92 eV at 1020 K and with a tenth of the material. The respective values for the octopoles in (14-0) CNT are 4.15 eV, 4.18 eV and 4.12 eV. This agrees with our previous conclusion that low temperatures and high densities are favourable for filling, but are fairly weak compared to the difference in internal energy over the practically accessible temperature and density ranges. The large favourability compared to the perturbed 1D CsI wires is likely for this same

reason: that internal energy is the primary determinant of filling favourability, and the octopolar systems here were examined at their relaxed, lowest-energy states.

# Chapter 8

# Conclusion

In this thesis, the simulation of materials encapsulated in carbon nanotubes has been explored in detail. The mismatch between the encapsulating CNT and filling has been investigated. A simple method of quantifying this mismatch has been developed, which quantatively predicts distortion of the soft host material, as well as strain energy. A method has been described to find minimum supercells of tube and filling to satisfy constraints on these artefacts. Iterative cycles of component-analysis and mismatch calculation were required where the component structures changed after encapsulation. However, the limiting assumption is that the equilibrium length of both filling and tube are unaffected by the act of encapsulation.

Existing methods of avoiding the expense of explicit simulation of carbon atoms in the encapsulating tube are limited to smooth cylinders. This thesis has shown that in fact the interiors of the CNTs are textured, with a chirality-dependent resistance to rotation and translation of the encapsulated crystal, whose associated energy is significant for experimentally-motivated systems. Encapsulated crystals have been shown to twist inside the CNT to conform to the texture, revealing new metastable states and raising the possibility of different chirality-dependent structures at the same CNT radius, an effect that clearly cannot be captured by smooth confining potentials. The ridging can also be balanced against the strain energy associated with mismatch, giving a value for physically realistic mismatch between core and filling and thus guiding the choice of compound supercell.

Three structures seen experimentally to exist within nanotubes have been relaxed *in vacuo*. The 'Eliseev' structure was seen to be stable, but to have weak interactions between neutral planes. Two rocksalt-like structures, one of which was sheared, were seen to be unstable without the CNT confinement. Artificial symmetry-constraints were applied, which resulted in relaxed rocksalt-like struc-

tures, but unstable phonons were seen when the artificial constraints were removed. These phononic modes were followed and the resultant structures modelled inside CNTs. Two sets of restorative forces were seen: radial forces due to confinement which decreased with tube radius, and axial forces due to mismatch-like axial constraint, which were independent of tube radius. These results question the practicality of CNT-neglect in all but serendipitous instances.

The charge distributions of encapsulated 1D chain systems, and of more complex structures discovered by AIRSS, have been investigated and charge transfer has been observed compared to the simple superposition of electron density distributions. Various methods of population analysis have been investigated, with the Mulliken and Hirshfeld methods displaying their expected shortcoming and the Bader and DDEC methods giving concordant and reasonable results. DDEC charges have been used to measure charge-transfer between filling and tube, with a magnitude of a few tenths of $e$ being transferred to the CNT, varying dependent on the CNT radius as well as the positions of crystal ions. Charge-transfer between core ions has been shown to be increased by the presence of CNTs. The associated Coulombic energy has been shown to be dominated by the core, the capacitor-like interaction of charged tube wall is comparably weak.

Quadratic fits based on an ion's distance from the axis, and distance to the nearest carbon atom, have been found to be accurate to within a few thousandths of $e$, but not transferrable between systems. The SOAP chemical-environment descriptors have been used to successfully machine-learn DDEC charges for encapsulated ions at a fraction of the time and computational cost, while being transferrable across all examined systems. The work in this thesis has discussed only the perturbed 1D case, but the extension to wider nanotubes and thicker fillings is expected to be straightforward.

The exploration of filling with respect to tube radius has been performed by DFT calculations of internal energy and chemical potentials, with the results justifying the choice of nanotubes used in the rest of the work described in this thesis. The effect of the entropic chemical potential terms was seen to be almost negligible, and dominated by the internal energy for a large range of practicable filling conditions. However, the work makes the assumption that all filling material is sublimed during the filling method, and also neglects kinetic effects.

### 8.0.1 Further work

The work on texture of the CNT prompts the creation of a textured confining potential, to allow larger- and longer-scale simulations of encapsulated materials.

The most basic such potential would be a simple repulsive potential which acts only on the encapsulated nuclei, tuned to reproduce the ridging behaviour detailed in this thesis. A short-ranged repulsion centred on the positions of the constituent carbon atoms of the tube would likely provide the encapsulation seen in existing smooth confining potentials, while control of the repulsive function would provide a tunable ridging. The focus on the carbon atoms would lend itself to a model which is transferrable across nanotube diameters and chiralities. However this potential could, if needed, be supplemented by an existing smooth encapsulating potential should effects such as Van de Waals smoothing require the effect of the ridging to be significantly weaker than that of the encapsulation. The added expense of the extra complication of a simple classical repulsion would be negligible in the context of *ab initio* simulations, more than worth the removal of the carbon atoms from the *ab initio* calculation.

A more comprehensive replacement of the carbon atoms would take electrical charge into account. The machine-learned charge-transfer prediction could be used to parameterise a chargeable confinement model. Carbon atoms could, in addition to neutral repulsive potentials, be endowed with point charges. The machine-learned charge-transfer model described in this thesis could be used to dynamically update the size of these point charges based on the neighbourhoods of explicitly-modelled core atoms. The number of valence electrons would need to be adjusted, this could be done in an update step similar to that of the atom positions. A more sophisticated method would be to develop a pseudopotential-like representation of the nanotube as a whole, such that valence electrons can transfer to the tube within a single SCF loop.

Rather than act as a method to support *ab initio* calculations, the machine-learned model could also be integrated into a broader potential or force-field, such as the existing SOAP potential, to integrate long-range Coulombic forces into the otherwise-local model. Such a model, properly trained on *ab initio* data, would be much faster than the *an inito* approach itself, though the accuracy of such a model remains to be seen.

The ability to model larger and longer systems would permit the exploration of a variety of physical effects. Of particular interest would be the relationship between chirality at equivalent radii and filling structure. Since helical crystals have been seen in encapsulation both experimentally [Philp et al., 2003] and in simulation [Wilson, 2002; Baldoni et al., 2007], and also we have shown the texture-dependence of metastable twisted states in this thesis, the relationship between chirality and structure merits attention.

The larger length-scale would also allow investigation into the effect of tube bending on the filling, which is so far restricted by the need for rhombohedral unit cells. This is of interest since filling shearing, which has been proposed by microscopy, has been attributed to tube bending [Sloan et al., 2003]. Further investigation could determine whether this shearing is indicative of a metastable phase or merely a continuous distortion due to tube bending.

Also enabled by this increased scale is insight into the interaction and relative stability of filling phases within nanotubes. While the energy-per-length of the sheared and unsheared metastable states will give some idea as to which is preferable, larger tubes allow the investigation into the interface between the phases. When investigated in bent tubes, this could give direct validation of the bend-induced phase-change of Sloan et al. [2003]. Apart from the rocksalt-like shearing, left- and right-handed helical crystals should be seen in equal measure. Since the helicity of the crystal could couple to the encapsulating tube, the interface between handedness could be expected to depend on the chirality of the tube.

It is not immediately clear whether the method of phonon analysis used in this thesis could be used in more general cases to model crystals *in vacuo* with the aim of faithfully representing encapsulated behaviour or even structure. While the process itself effectively shows the stabilisation of unstable modes in *ansatze* by the encapsulating tube, the significant expense of phonon calculations must compete with the cost of simply modelling the tube. While the work in this thesis shows that future work must - in general - model the tube at least implicitly, more research would be required to develop the phonon-based technique into a predictive model.

The competition between a periodic 'ridging' potential and encapsulated ionic 'springs' raises the possibility of a Frenkel-Kontorova model [Braun and Kivshar, 1998, 2004], opening the door to nonlinear interactions which admits topological and dynamical soliton-like behaviour of defects, potentially leading to a new medium for nonlinear waves.

# Bibliography


Antonio Ferreira Ãvila and Guilherme Silveira Rachid Lacerda. Molecular mechanics applied to single-walled carbon nanotubes. *Materials Research*, 11:325 – 333, 2008. ISSN 1516-1439.

Adolf A. Abrahamson. Born-Mayer-type interatomic potential for neutral ground-state atoms with Z=2 to Z=105. *Physical Review*, 178(1):76–79, 1969. doi: 10.1103/physrev.178.76.

P. M. Ajayan and Sumio lijima. Capillarity-induced filling of carbon nanotubes. *Nature*, 361(6410):333–334, 1993. doi: 10.1038/361333a0.

Ethem Alpaydin. *Introduction to Machine Learning*. The MIT Press, 2nd edition, 2010. ISBN 026201243X, 9780262012430.

B. M. Axilrod and E. Teller. Interaction of the van der Waals type between three atoms. *The Journal of Chemical Physics*, 11(6):299, 1943. doi: 10.1063/1.1723844.

R.F.W. Bader. *Atoms in Molecules: A Quantum Theory*. International Ser. of Monogr. on Chem. Clarendon Press, 1994. ISBN 9780198558651.

Matteo Baldoni, Stefano Leoni, Antonio Sgamellotti, Gotthard Seifert, and Francesco Mercuri. Formation, structure, and polymorphism of novel lowest-dimensional AgI nanoaggregates by encapsulation in carbon nanotubes. *Small*, 3 (10):1730–1734, 2007. ISSN 1613-6829. doi: 10.1002/smll.200700296.

Albert P. Bartók, Mike C. Payne, Risi Kondor, and Gábor Csányi. Gaussian approximation potentials: The accuracy of quantum mechanics, without the electrons. *Phys. Rev. Lett.*, 104:136403, 2010. doi: 10.1103/PhysRevLett.104.136403.

Albert P. Bartók, Risi Kondor, and Gábor Csányi. On representing chemical environments. *Phys. Rev. B*, 87:184115, 2013. doi: 10.1103/PhysRevB.87.184115.

Jonathan Barzilai and Jonathan M. Borwein. Two-point step size gradient methods. *IMA Journal of Numerical Analysis*, 8(1):141–148, 1988. doi: 10.1093/imanum/8.1.141.

Jörg Behler. Neural network potential-energy surfaces in chemistry: a tool for large-scale simulations. *Phys. Chem. Chem. Phys.*, 13(40):17930, 2011. doi: 10.1039/c1cp21668f.

Jörg Behler and Michele Parrinello. Generalized neural-network representation of high-dimensional potential-energy surfaces. *Phys. Rev. Lett.*, 98:146401, 2007. doi: 10.1103/PhysRevLett.98.146401.

Robert A. Bell, Simon M.-M. Dubois, Michael C. Payne, and Arash A. Mostofi. Electronic transport calculations in the onetep code: Implementation and applications. *Computer Physics Communications*, 193:78–88, 2015. doi: 10.1016/j.cpc.2015.04.002.

Elena Bichoutskaia and Nicholas C. Pyper. Theoretical study of the structures and electronic properties of all-surface KI and CsI nanocrystals encapsulated in single walled carbon nanotubes. *The Journal of Chemical Physics*, 129(15):154701, 2008. doi: 10.1063/1.2987703.

Salomon R. Billeter, Alessandro Curioni, Dominik Fischer, and Wanda Andreoni. *Ab initio* derived augmented Tersoff potential for silicon oxynitride compounds and their interfaces with silicon. *Phys. Rev. B*, 73:155329, 2006. doi: 10.1103/PhysRevB.73.155329.

Clare L. Bishop and Mark Wilson. The energetics of inorganic nanotubes. *Molecular Physics*, 106(12-13):1665–1674, 2008. doi: 10.1080/00268970802304593.

Clare L Bishop and Mark Wilson. The mechanisms for filling carbon nanotubes with molten salts: carbon nanotubes as energy landscape filters. *J. Phys.: Condens. Matter*, 21(11):115301, 2009a. ISSN 1361-648X. doi: 10.1088/0953-8984/21/11/115301.

Clare L. Bishop and Mark Wilson. The filling of flexible carbon nanotubes by molten salts. *J. Mater. Chem.*, 19(19):2929, 2009b. ISSN 1364-5501. doi: 10.1039/b814902j.

P. E. Blöchl. Projector augmented-wave method. *Physical Review B*, 50(24):17953–17979, 1994. doi: 10.1103/physrevb.50.17953.

Max Born and Joseph E. Mayer. Zur gittertheorie der ionenkristalle. *Zeitschrift für Physik*, 75(1-2):1–18, 1932. doi: 10.1007/bf01340511.

Oleg M. Braun and Yuri S. Kivshar. Nonlinear dynamics of the frenkel–kontorova model. *Physics Reports*, 306(1-2):1–108, 1998. doi: 10.1016/s0370-1573(98)00029-5.

Oleg M. Braun and Yuri S. Kivshar. *The Frenkel-Kontorova Model*. Springer-Verlag GmbH, 2004. ISBN 3540407715.

Donald W. Brenner. Empirical potential for hydrocarbons for use in simulating the chemical vapor deposition of diamond films. *Phys. Rev. B*, 42(15):9458–9471, 1990. doi: 10.1103/physrevb.42.9458.

Peter Brommer and David Quigley. Automated effective band structures for defective and mismatched supercells. *Journal of Physics: Condensed Matter*, 26(48):485501, 2014. doi: 10.1088/0953-8984/26/48/485501.

C. G. Broyden. A class of methods for solving nonlinear simultaneous equations. *Mathematics of Computation*, 19(92):577–577, 1965. doi: 10.1090/s0025-5718-1965-0198670-6.

R. A. Buckingham. The classical equation of state of gaseous helium, neon and argon. *Proceedings of the Royal Society A: Mathematical, Physical and Engineering Sciences*, 168(933):264–283, 1938. doi: 10.1098/rspa.1938.0173.

Mario Capitelli, Gianpiero Colonna, and Antonio D'Angola. Molecular partition function: Vibrational, rotational and electronic contributions. In *Fundamental Aspects of Plasma Chemical Physics*, pages 79–99. Springer Nature, 2011. doi: 10.1007/978-1-4419-8182-0_5.

Robin Carter, Mikhail Suyetin, Samantha Lister, M. Adam Dyson, Harrison Trewhitt, Sanam Goel, Zheng Liu, Kazu Suenaga, Cristina Giusca, Reza J. Kashtiban, and et al. Band gap expansion, shear inversion phase change behaviour and low-voltage induced crystal oscillation in low-dimensional tin selenide crystals. *Dalton Trans.*, 43(20):7391–7399, 2014. ISSN 1477-9234. doi: 10.1039/c4dt00185k.

CASTEP website. CASTEP. `http://www2.castep.org`.

Augustin-Louis Cauchy. Méthode générale pour la résolution des systèmes d'équations simultanées. *Compte Rendu des S'eances de L'Acad'emie des Sciences XXV*, S'erie A(25):536–538, 1847.

D. M. Ceperley and B. J. Alder. Ground state of the electron gas by a stochastic method. *Physical Review Letters*, 45(7):566–569, 1980. doi: 10.1103/physrevlett.45.566.

Yan Chai, Ting Guo, Changming Jin, Robert E. Haufler, L. P. Felipe Chibante, Jan Fure, Lihong Wang, J. Michael Alford, and Richard E. Smalley. Fullerenes with metals inside. *J. Phys. Chem.*, 95(20):7564–7568, 1991. ISSN 1541-5740. doi: 10.1021/j100173a002. Introduction of X@Y notation.

Z. Cheng, P.M. Chaikin, W.B. Russel, W.V. Meyer, J. Zhu, R.B. Rogers, and R.H. Ottewill. Phase diagram of hard spheres. *Materials & Design*, 22(7):529–534, 2001. doi: 10.1016/s0261-3069(01)00015-2.

S. J. Clark, M. D. Segall, C. J. Pickard, P. J. Hasnip, M. J. Probert, K. Refson, and M. C. Payne. First principles methods using CASTEP. *Z. Krystallogr.*, 220: 567–570, 2005.

B. de B. Darwent. *Bond Dissociation Energies in Simple Molecules*. NSRDS-NBS. U.S. National Bureau of Standards, 1970.

B. L. Davis and L. H. Adams. High-pressure polymorphs in the silver iodide phase diagram. *Science*, 146(3643):519–521, 1964. doi: 10.1126/science.146.3643.519.

den2cube website. `den2cube` website. `http://theory.cm.utexas.edu/henkelman/code/bader/download/den2cube.tar.gz`.

Thomas DeVries and Worth H. Rodebush. The thermal dissociation of iodine and bromine. *Journal of the American Chemical Society*, 49(3):656–666, 1927. ISSN 1520-5126. doi: 10.1021/ja01402a008.

E. Dujardin, T. W. Ebbesen, H. Hiura, and K. Tanigaki. Capillarity and wetting of carbon nanotubes. *Science*, 265(5180):1850–1852, 1994. doi: 10.1126/science.265.5180.1850.

A.A. Eliseev, L.V. Yashina, M.M. Brzhezinskaya, M.V. Chernysheva, M.V. Kharlamova, N.I. Verbitsky, A.V. Lukashin, N.A. Kiselev, A.S. Kumskov, R.M. Zakalyuhin, and et al. Structure and electronic properties of agx (x=cl, br, i)-intercalated single-walled carbon nanotubes. *Carbon*, 48(10):2708–2721, 2010. ISSN 0008-6223. doi: 10.1016/j.carbon.2010.02.037.

Andrei Eliseev, Lada Yashina, Marianna Kharlamova, and Nikolay Kiselev. *One-Dimensional Crystals inside Single-Walled Carbon Nanotubes: Growth, Structure*

*and Electronic Properties*, chapter 8, pages 127–156. Intech, 2011. doi: 10.5772/19060.

ELK website. ELK: all-electron full-potential linearised augmented-plane wave code. `http://elk.sourceforge.net/`.

Andrey N. Enyashin, Ronen Kreizman, and Gotthard Seifert. Capillary imbibition of PbI2 melt by inorganic and carbon nanotubes. *The Journal of Physical Chemistry C*, 113(31):13664–13669, 2009. doi: 10.1021/jp903649w.

Ricardo Ferreira. Principle of electronegativity equalization. Part 1. Bond moments and force constants. *Transactions of the Faraday Society*, 59:1064, 1963. ISSN 0014-7672. doi: 10.1039/tf9635901064.

R. Fletcher. *Practical Methods of Optimization*. A Wiley-Interscience publication. Wiley, 2000. ISBN 9780471494638.

D. Frenkel and B. Smit. *Understanding Molecular Simulation: From Algorithms to Applications*. Computational science series. Elsevier Science, 2001. ISBN 9780080519982.

Steffi Friedrichs, Uwe Falke, and Malcolm L. H. Green. Phase separation of LaI3 inside single-walled carbon nanotubes. *ChemPhysChem*, 6(2):300–305, 2005. doi: 10.1002/cphc.200400361.

Toshihiko Fujimori, Renato Batista dos Santos, Takuya Hayashi, Morinobu Endo, Katsumi Kaneko, and David Tomànek. Formation and properties of selenium double-helices inside double-wall carbon nanotubes: Experiment and theory. *ACS Nano*, 7(6):5607–5613, 2013. ISSN 1936-086X. doi: 10.1021/nn4019703.

Giulia Galli. Linear scaling methods for electronic structure calculations and quantum molecular dynamics simulations. *Current Opinion in Solid State and Materials Science*, 1(6):864–874, 1996. doi: 10.1016/s1359-0286(96)80114-8.

Dmitri Golberg, Yoshio Bando, Masanori Mitome, Keita Fushimi, and Chengchun Tang. Boron nitride nanotubes as nanocrucibles for morphology and phase transformations in encapsulated nanowires of the Mg–O system. *Acta Materialia*, 52 (11):3295–3303, 2004. doi: 10.1016/j.actamat.2004.03.025.

Stefan Grimme. Density functional theory with london dispersion corrections. *Wiley Interdisciplinary Reviews: Computational Molecular Science*, 1(2):211–228, 2011. doi: 10.1002/wcms.30.

Noriaki Hamada, Shin ichi Sawada, and Atsushi Oshiyama. New one-dimensional conductors: Graphitic microtubules. *Phys. Rev. Lett.*, 68(10):1579–1581, 1992. doi: 10.1103/physrevlett.68.1579.

D. R. Hamann, M. Schlüter, and C. Chiang. Norm-conserving pseudopotentials. *Phys. Rev. Lett.*, 43(20):1494–1497, 1979. doi: 10.1103/physrevlett.43.1494.

Wei-Qiang Han, C. W. Chang, and A. Zettl. Encapsulation of one-dimensional potassium halide crystals within BN nanotubes. *Nano Letters*, 4(7):1355–1357, 2004. doi: 10.1021/nl0494452.

D. Hanneke, S. Fogwell, and G. Gabrielse. New measurement of the electron magnetic moment and the fine structure constant. *Phys. Rev. Lett.*, 100:120801, 2008. doi: 10.1103/PhysRevLett.100.120801.

J. S. Hansen, Thomas B. Schrøder, and Jeppe C. Dyre. Simplistic coulomb forces in molecular dynamics: Comparing the Wolf and shifted-force approximations. *The Journal of Physical Chemistry B*, 116(19):5738–5743, 2012. doi: 10.1021/jp300750g.

David J. Hardy, John E. Stone, and Klaus Schulten. Multilevel summation of electrostatic potentials using graphics processing units. *Parallel Computing*, 35(3):164–177, 2009. doi: 10.1016/j.parco.2008.12.005.

D R Hartree. The calculation of atomic structures. *Rep. Prog. Phys.*, 11(1):113–143, 1947. doi: 10.1088/0034-4885/11/1/305.

Graeme Henkelman, Andri Arnaldsson, and Hannes Jónsson. A fast and robust algorithm for bader decomposition of charge density. *Computational Materials Science*, 36(3):354–360, 2006. doi: 10.1016/j.commatsci.2005.04.010.

N. D. M. Hine, K. Frensch, W. M. C. Foulkes, and M. W. Finnis. Supercell size scaling of density functional theory formation energies of charged defects. *Physical Review B*, 79(2), 2009. ISSN 1550-235X. doi: 10.1103/physrevb.79.024112.

Nicholas D. M. Hine, Jacek Dziedzic, Peter D. Haynes, and Chris-Kriton Skylaris. Electrostatic interactions in finite systems treated with periodic boundary conditions: Application to linear-scaling density functional theory. *The Journal of Chemical Physics*, 135(20):204103, 2011. doi: 10.1063/1.3662863.

F. L. Hirshfeld. Bonded-atom fragments for describing molecular charge densities. *Theoretica chimica acta*, 44(2):129–138, 1977. ISSN 1432-2234. doi: 10.1007/BF00549096.

P. Hohenberg and W. Kohn. Inhomogeneous electron gas. *Phys. Rev.*, 136:B864–B871, 1964. doi: 10.1103/PhysRev.136.B864.

R. Honerjäger and R. Tischer. Mikrowellenrotationsspektren der Molekeln CsF, CsCl, CsBr und Csl. *Z. Naturforsch. A*, 29:819, 1974.

Sung You Hong, Ronen Kreizman, Rita Rosentsveig, Alla Zak, Jeremy Sloan, Andrey N. Enyashin, Gotthard Seifert, Malcolm L. H. Green, and Reshef Tenne. One- and two-dimensional inorganic crystals inside inorganic nanotubes. *Eur. J. Inorg. Chem.*, 2010(27):4233–4243, 2010. ISSN 1099-0682. doi: 10.1002/ejic.201000456.

A. Honig, M. Mandel, M. L. Stitch, and C. H. Townes. Microwave spectra of the alkali halides. *Phys. Rev.*, 96(3):629–642, 1954. doi: 10.1103/physrev.96.629.

Sumio Iijima. Helical microtubules of graphitic carbon. *Nature*, 354(6348):56–58, 1991. doi: 10.1038/354056a0.

M. R. Jarvis, I. D. White, R. W. Godby, and M. C. Payne. Supercell technique for total-energy calculations of finite charged and polar systems. *Phys. Rev. B*, 56 (23):14972–14978, 1997. doi: 10.1103/physrevb.56.14972.

T. Kaiho. *Iodine Chemistry and Applications*. Wiley, 2014. ISBN 9781118466292.

M V Kharlamova. Electronic properties of pristine and modified single-walled carbon nanotubes. *Phys.-Usp.*, 56(11):1047–1073, 2013. ISSN 1468-4780. doi: 10.3367/ufne.0183.201311a.1145.

V. K. Khersonskii, A. N. Moskalev, and D. A. Varshalovich. *Quantum Theory of Angular Momemtum*. WORLD SCIENTIFIC PUB CO INC, 1988. ISBN 9971501074.

Alex Kleiner and Sebastian Eggert. Band gaps of primary metallic carbon nanotubes. *Phys. Rev. B*, 63(7), 2001. doi: 10.1103/physrevb.63.073408.

W. Kohn and L. J. Sham. Self-consistent equations including exchange and correlation effects. *Phys. Rev.*, 140:A1133–A1138, 1965. doi: 10.1103/PhysRev.140.A1133.

D. S. Kosov and P. L. A. Popelier. Atomic partitioning of molecular electrostatic potentials. *J. Phys. Chem. A*, 104(31):7339–7345, 2000. doi: 10.1021/jp0003407.

Ronen Kreizman, Sung You Hong, Jeremy Sloan, Ronit Popovitz-Biro, Ana Albu-Yaron, Gerard Tobias, Belén Ballesteros, Benjamin G. Davis, Malcolm L. H.

Green, and Reshef Tenne. Core-shell PbI2@WS2 inorganic nanotubes from capillary wetting. *Angewandte Chemie International Edition*, 48(7):1230–1233, 2008. doi: 10.1002/anie.200803447.

G. Kresse and J. Furthmüller. Efficient iterative schemes forab initiototal-energy calculations using a plane-wave basis set. *Physical Review B*, 54(16):11169–11186, 1996. doi: 10.1103/physrevb.54.11169.

G. Kresse and D. Joubert. From ultrasoft pseudopotentials to the projector augmented-wave method. *Physical Review B*, 59(3):1758–1775, 1999. doi: 10.1103/physrevb.59.1758.

LAMMPS website. LAMMPS molecular dynamics simulator. `http://lammps.sandia.gov`.

Guillaume Lamoureux and Benoî Roux. Modeling induced polarization with classical Drude oscillators: Theory and molecular dynamics simulation algorithm. *The Journal of Chemical Physics*, 119(6):3025, 2003. doi: 10.1063/1.1589749.

Jhinhwan Lee, H. Kim, S.-J. Kahng, G. Kim, Y.-W. Son, J. Ihm, H. Kato, Z. W. Wang, T. Okazaki, H. Shinohara, and Young Kuk. Bandgap modulation of carbon nanotubes by encapsulated metallofullerenes. *Nature*, 415(6875):1005–1008, 2002. doi: 10.1038/4151005a.

Xin Lu and Zhongfang Chen. Curved pi-conjugation, aromaticity, and the related chemistry of small fullerenes (<C 60 ) and single-walled carbon nanotubes. *Chem. Rev.*, 105(10):3643–3696, 2005. ISSN 1520-6890. doi: 10.1021/cr030093d.

David J. C. MacKay. *Information Theory, Inference and Learning Algorithms*. Cambridge University Pr., 2003. ISBN 0521642981.

G. K. H. Madsen, C. Gatti, B. B. Iversen, Lj. Damjanovic, G. D. Stucky, and V. I. Srdanov. F center in sodium electrosodalite as a physical manifestation of a non-nuclear attractor in the electron density. *Phys. Rev. B*, 59:12359–12369, 1999. doi: 10.1103/PhysRevB.59.12359.

Amit Mahajan, Angus Kingon, Ákos Kukovecz, Zoltan Konya, and Paula M. Vilarinho. Studies on the thermal decomposition of multiwall carbon nanotubes under different atmospheres. *Materials Letters*, 90:165–168, 2013. doi: 10.1016/j.matlet.2012.08.120.

Thomas A. Manz and David S. Sholl. Chemically meaningful atomic charges that reproduce the electrostatic potential in periodic and nonperiodic materials. *Journal of Chemical Theory and Computation*, 6(8):2455–2468, 2010. doi: 10.1021/ct100125x. PMID: 26613499.

Thomas A. Manz and David S. Sholl. Improved atoms-in-molecule charge partitioning functional for simultaneously reproducing the electrostatic potential and chemical states in periodic and nonperiodic materials. *J. Chem. Theory Comput.*, 8(8):2844–2867, 2012. doi: 10.1021/ct3002199.

Sergei Manzhos, Richard Dawes, and Tucker Carrington. Neural network-based approaches for building high dimensional and quantum dynamics-friendly potential energy surfaces. *Int. J. Quantum Chem.*, 115(16):1012–1020, 2014. doi: 10.1002/qua.24795.

Richard M. Martin. *Electronic Structure: Basic Theory and Practical Methods*. Cambridge University Press, 1st paperback edition, 2008.

Glenn J. Martyna and Mark E. Tuckerman. A reciprocal space based method for treating long range interactions in ab initio and force-field-based calculations in clusters. *The Journal of Chemical Physics*, 110(6):2810, 1999. doi: 10.1063/1.477923.

Yuki Matsuda, Jamil Tahir-Kheli, and William A. Goddard. Definitive band gaps for single-wall carbon nanotubes. *J. Phys. Chem. Lett.*, 1(19):2946–2950, 2010. doi: 10.1021/jz100889u.

Ian J. McNaught. The electronic spectrum of iodine revisited. *Journal of Chemical Education*, 57(2):101, 1980. doi: 10.1021/ed057p101.

Peter Minary, Joseph A. Morrone, Dawn A. Yarne, Mark E. Tuckerman, and Glenn J. Martyna. Long range interactions on wires: A reciprocal space based formalism. *The Journal of Chemical Physics*, 121(23):11949–11956, 2004. doi: 10.1063/1.1806403.

V. I. Minkin. Glossary of terms used in theoretical organic chemistry. *Pure and Applied Chemistry*, 71(10), 1999. doi: 10.1351/pac199971101919.

J. W. Mintmire, B. I. Dunlap, and C. T. White. Are fullerene tubules metallic? *Phys. Rev. Lett.*, 68(5):631–634, 1992. doi: 10.1103/physrevlett.68.631.

P J Mitchell and D Fincham. Shell model simulations by adiabatic dynamics. *Journal of Physics: Condensed Matter*, 5(8):1031–1038, 1993. doi: 10.1088/0953-8984/5/8/006.

Hendrik J Monkhorst and James D Pack. Special points for brillouin-zone integrations. *Physical Review B*, 13(12):5188, 1976.

Philip M. Morse. Diatomic molecules according to the wave mechanics. II. vibrational levels. *Physical Review*, 34(1):57–64, 1929. doi: 10.1103/physrev.34.57.

R. S. Mulliken. Electronic population analysis on LCAO-MO molecular wave functions. i. *The Journal of Chemical Physics*, 23(10):1833–1840, 1955. doi: http://dx.doi.org/10.1063/1.1740588.

Lambert Murray. Thermodynamics (phys 425) chapter 12: "classical" statistical physics and the partition function. 2006.

John J. Nash. Vibrational modes of small molecules. http://www.chem.purdue.edu/gchelp/vibs/i2.html, 2001.

Radford M. Neal. *Bayesian Learning for Neural Networks*. Springer, 1996. ISBN 0387947248.

Thomas Olsen and Kristian S. Thygesen. Beyond the random phase approximation: Improved description of short-range correlation by a renormalized adiabatic local density approximation. *Physical Review B*, 88(11), 2013. ISSN 1550-235X. doi: 10.1103/physrevb.88.115131.

ONETEP website. ONETEP (Order-N Electronic Total Energy Package). `http://www2.tcm.phy.cam.ac.uk/onetep/`.

M. Ouyang. Energy gaps in "metallic" single-walled carbon nanotubes. *Science*, 292(5517):702–705, 2001. doi: 10.1126/science.1058853.

A. Pantano, M. C. Boyce, and D. M. Parks. Mechanics of axial compression of single and multi-wall carbon nanotubes. *Journal of Engineering Materials and Technology*, 126(3):279, 2004. doi: 10.1115/1.1752926.

M. Parrinello and A. Rahman. Crystal structure and pair potentials: A molecular-dynamics study. *Phys. Rev. Lett.*, 45(14):1196–1199, 1980. doi: 10.1103/physrevlett.45.1196.

Linus Pauling. The nature of the chemical bond, IV: The energy of single bonds and the relative electronegativity of atoms. *J. Am. Chem. Soc.*, 54(9):3570–3582, 1932. doi: 10.1021/ja01348a011.

Linus Pauling. Atomic radii and interatomic distances in metals. *J. Am. Chem. Soc.*, 69(3):542–553, 1947. doi: 10.1021/ja01195a024.

Mark R. Pederson and Jeremy Q. Broughton. Nanocapillarity in fullerene tubules. *Phys. Rev. Lett.*, 69:2689–2692, 1992. doi: 10.1103/PhysRevLett.69.2689.

John P. Perdew. Jacob's ladder of density functional approximations for the exchange-correlation energy. *AIP Conference Proceedings*, 2001. ISSN 0094-243X. doi: 10.1063/1.1390175.

John P. Perdew and Yue Wang. Accurate and simple analytic representation of the electron-gas correlation energy. *Phys. Rev. B*, 45:13244–13249, 1992. doi: 10.1103/PhysRevB.45.13244.

John P. Perdew, Kieron Burke, and Matthias Ernzerhof. Generalized gradient approximation made simple. *Phys. Rev. Lett.*, 77:3865–3868, 1996. doi: 10.1103/PhysRevLett.77.3865.

Eilidh Philp, Jeremy Sloan, Angus I. Kirkland, Rudiger R. Meyer, Steffi Friedrichs, John L. Hutchison, and Malcolm L. H. Green. An encapsulated helical one-dimensional cobalt iodide nanostructure. *Nat. Mater.*, 2(12):788–791, 2003. ISSN 1476-1122.

Chris J. Pickard and R. J. Needs. High-pressure phases of silane. *Phys. Rev. Lett.*, 97(4), 2006. doi: 10.1103/physrevlett.97.045504.

C. E. Piermarini, G. J.; Weir. A diamond cell for x-ray diffraction studies at high pressures. *Journal of Research of the National Bureau of Standards*, 66A(4):325, 1962.

Steve Plimpton. Fast parallel algorithms for short-range molecular dynamics. *Journal of Computational Physics*, 117(1):1–19, 1995. doi: 10.1006/jcph.1995.1039.

Paul L. A. Popelier. QCTFF: On the construction of a novel protein force field. *Int. J. Quantum Chem.*, 115(16):1005–1011, 2015. doi: 10.1002/qua.24900.

Mercè Pacios Pujadó. *Carbon Nanotubes as Platforms for Biosensors with Electrochemical and Electronic Transduction.* Springer-Verlag GmbH, 2012. ISBN 3642314201.

Péter Pulay. Convergence acceleration of iterative sequences. the case of SCF iteration. *Chemical Physics Letters*, 73(2):393–398, 1980. doi: 10.1016/0009-2614(80)80396-4.

Quickstep website. Quickstep GPW/GAPW code. `https://www.cp2k.org/quickstep`.

L.V. Radushkevich and V.M. Lukyanovich. The structure of carbon forming in thermal decomposition of carbon monoxide on an iron catalyst (in russian). *Russian Journal of Physical Chemistry*, 26:88–95, 1952.

Raghuveer M. Rao and Soheil A. Dianat. Fast algorithms for phase and magnitude reconstruction from bispectra. *Optical Engineering*, 29(5):504–512, 1990. doi: 10.1117/12.55619.

Anthony K. Rappe and William A. Goddard. Charge equilibration for molecular dynamics simulations. *The Journal of Physical Chemistry*, 95(8):3358–3363, 1991. doi: 10.1021/j100161a070.

Rappe-Bennet pseudopotential library. Atomic simulation environment. `https://wiki.fysik.dtu.dk/ase/`.

Rasmussen. *Gaussian Processes for Machine Learning*. MIT University Press Group Ltd, 2006. ISBN 026218253X.

Robert J. Le Roy, Nikesh S. Dattani, John A. Coxon, Amanda J. Ross, Patrick Crozet, and Colan Linton. Accurate analytic potentials for $Li_2(x^1\Sigma_g^+)$ and $Li_2(a^1\Sigma_u^+)$ from 2 to 90 å, and the radiative lifetime of Li(2p). *The Journal of Chemical Physics*, 131(20):204309, 2009. doi: 10.1063/1.3264688.

Carlo A. Rozzi, Daniele Varsano, Andrea Marini, Eberhard K. U. Gross, and Angel Rubio. Exact coulomb cutoff technique for supercell calculations. *Phys. Rev. B*, 73(20), 2006. doi: 10.1103/physrevb.73.205119.

Álvaro Ruiz-Serrano and Chris-Kriton Skylaris. A variational method for density functional theory calculations on metallic systems with thousands of atoms. *The Journal of Chemical Physics*, 139(5):054107, 2013. doi: 10.1063/1.4817001.

Matthias Rupp, Alexandre Tkatchenko, Klaus-Robert Müller, and O. Anatole von Lilienfeld. Fast and accurate modeling of molecular atomization energies with machine learning. *Phys. Rev. Lett.*, 108(5), 2012. doi: 10.1103/physrevlett.108.058301.

Soumen Saha, Ram Kinkar Roy, and Paul W. Ayers. Are the Hirshfeld and Mulliken population analysis schemes consistent with chemical intuition? *International Journal of Quantum Chemistry*, 109(9):1790–1806, 2009. ISSN 1097-461X. doi: 10.1002/qua.21901.

Daniel Sanchez-Portal, Emilio Artacho, and Jose M Soler. Projection of plane-wave calculations into atomic orbitals. *Solid State Communications*, 95(10):685–690, 1995. doi: 10.1016/0038-1098(95)00341-x.

Emma L. Sceats, Jennifer C. Green, and Stephanie Reich. Theoretical study of the molecular and electronic structure of one-dimensional crystals of potassium iodide and composites formed upon intercalation in single-walled carbon nanotubes. *Phys. Rev. B*, 73(12), 2006. doi: 10.1103/physrevb.73.125441.

Emma L. Sceats, Malcolm L.H. Green, Angus I. Kirkland, and Jennifer C. Green. DFT calculations of KI crystals formed within single-walled carbon nanotubes. *Chem. Phys. Lett.*, 466(1-3):76 – 78, 2008. ISSN 0009-2614. doi: 10.1016/j.cplett.2008.10.030.

M. D. Segall, C. J. Pickard, R. Shah, and M. C. Payne. Population analysis in plane wave electronic structure calculations. *Molecular Physics*, 89(2):571–577, 1996a. doi: 10.1080/002689796173912.

M. D. Segall, R. Shah, C. J. Pickard, and M. C. Payne. Population analysis of plane-wave electronic structure calculations of bulk materials. *Phys. Rev. B*, 54 (23):16317–16320, 1996b. doi: 10.1103/physrevb.54.16317.

M D Segall, Philip J D Lindan, M J Probert, C J Pickard, P J Hasnip, S J Clark, and M C Payne. First-principles simulation: ideas, illustrations and the CASTEP code. *Journal of Physics: Condensed Matter*, 14(11):2717–2744, 2002. doi: 10.1088/0953-8984/14/11/301.

Thomas P Senftle, Sungwook Hong, Md Mahbubul Islam, Sudhir B Kylasa, Yuanxia Zheng, Yun Kyung Shin, Chad Junkermeier, Roman Engel-Herbert, Michael J Janik, Hasan Metin Aktulga, Toon Verstraelen, Ananth Grama, and Adri C T van Duin. The ReaxFF reactive force-field: development, applications and future directions. *npj Computational Materials*, 2:15011, 2016. doi: 10.1038/npjcompumats.2015.11.

Ryosuke Senga, Hannu-Pekka Komsa, Zheng Liu, Kaori Hirose-Takai, Arkady V. Krasheninnikov, and Kazu Suenaga. Atomic structure and dynamic behaviour of

truly one-dimensional ionic chains inside carbon nanotubes. *Nat Mater*, 13(11): 1050–1054, 2014. ISSN 1476-4660. doi: 10.1038/nmat4069.

D. B. Sirdeshmukh, L. Sirdeshmukh, and K. G. Subhadra. *Alkali Halides*. Springer, 2010. ISBN 3642075789.

Chris-Kriton Skylaris, Arash A. Mostofi, Peter D. Haynes, Oswaldo Diéguez, and Mike C. Payne. Nonorthogonal generalized wannier function pseudopotential plane-wave method. *Phys. Rev. B*, 66(3), 2002. doi: 10.1103/physrevb.66.035119.

Chris-Kriton Skylaris, Peter D. Haynes, Arash A. Mostofi, and Mike C. Payne. Introducing ONETEP: Linear-scaling density functional simulations on parallel computers. *The Journal of Chemical Physics*, 122(8):084119, 2005. doi: 10.1063/1.1839852.

J. Sloan, M.C. Novotny, S.R. Bailey, G. Brown, C. Xu, V.C. Williams, S. Friedrichs, E. Flahaut, R.L. Callender, A.P.E. York, K.S. Coleman, M.L.H. Green, R.E. Dunin-Borkowski, and J.L. Hutchison. Two layer 4:4 co-ordinated KI crystals grown within single walled carbon nanotubes. *Chemical Physics Letters*, 329(1-2):61–65, 2000. doi: 10.1016/s0009-2614(00)00998-2.

Jeremy Sloan, Angus I. Kirkland, John L. Hutchison, and Malcolm L. H. Green. Structural characterization of atomically regulated nanocrystals formed within single-walled carbon nanotubes using electron microscopy. *Accounts of Chemical Research*, 35(12):1054–1062, 2002a. doi: 10.1021/ar010169x.

Jeremy Sloan, Angus I. Kirkland, John L. Hutchison, and Malcolm L. H. Green. Integral atomic layer architectures of 1D crystals inserted into single walled carbon nanotubes. *Chemical Communications*, (13):1319–1332, 2002b. doi: 10.1039/b200537a.

Jeremy Sloan, Mauricio Terrones, Stefan Nufer, Steffi Friedrichs, Sam R. Bailey, Hee-Gweon Woo, Manfred Rühle, John L. Hutchison, and Malcolm L. H. Green. Metastable one-dimensional $AgCl_{1-x}I_x$ solid-solution wurzite "tunnel"" crystals formed within single-walled carbon nanotubes. *Journal of the American Chemical Society*, 124(10):2116–2117, 2002c. ISSN 1520-5126. doi: 10.1021/ja0173270.

Jeremy Sloan, Angus I. Kirkland, John L. Hutchison, and Malcolm L.H. Green. Aspects of crystal growth within carbon nanotubes. *C. R. Phys.*, 4(9):1063–1074, 2003. ISSN 1631-0705. doi: 10.1016/S1631-0705(03)00102-6.

Edward Snelson and Zoubin Ghahramani. Sparse Gaussian processes using pseudo-inputs. In Y. Weiss, B. Schölkopf, and J. C. Platt, editors, *Advances in Neural Information Processing Systems 18*, pages 1257–1264. MIT Press, 2006.

Nicholas D Spencer and John H Moore. *Encyclopedia of chemical physics and physical chemistry: Applications*, volume 1. Taylor & Francis, 2001.

Paul J. Steinhardt, David R. Nelson, and Marco Ronchetti. Bond-orientational order in liquids and glasses. *Phys. Rev. B*, 28(2):784–805, 1983. doi: 10.1103/physrevb.28.784.

T. L. Story. Dipole moments of KI, RbBr, RbI, CsBr, and CsI by the electric deflection method. *The Journal of Chemical Physics*, 64(2):855, 1976. doi: 10.1063/1.432235.

Guangyu Sun, Jenö Kürti, Miklos Kertesz, and Ray H. Baughman. Variations of the geometries and band gaps of single-walled carbon nanotubes and the effect of charge injection. *J. Phys. Chem. B*, 107(29):6924–6931, 2003. ISSN 1520-5207. doi: 10.1021/jp022629p.

W Tang, E Sanville, and G Henkelman. A grid-based Bader analysis algorithm without lattice bias. *Journal of Physics: Condensed Matter*, 21(8):084204, 2009.

J. Tersoff. New empirical model for the structural properties of silicon. *Phys. Rev. Lett.*, 56(6):632–635, 1986. doi: 10.1103/physrevlett.56.632.

J. Tersoff. Empirical interatomic potential for silicon with improved elastic properties. *Phys. Rev. B*, 38(14):9902–9905, 1988a. doi: 10.1103/physrevb.38.9902.

J. Tersoff. New empirical-approach for the structure and energy of covalent systems. *Phys. Rev. B*, 37:6991–7000, 1988b. doi: 10.1103/PhysRevLett.56.632.

J. Tersoff. Modeling solid-state chemistry: Interatomic potentials for multicomponent systems. *Phys. Rev. B*, 39(8):5566–5568, 1989. doi: 10.1103/physrevb.39.5566.

Alexandre Tkatchenko and Matthias Scheffler. Accurate molecular van der waals interactions from ground-state electron density and free-atom reference data. *Physical Review Letters*, 102(7), 2009. ISSN 1079-7114. doi: 10.1103/physrevlett.102.073005.

Adri C. T. van Duin, Siddharth Dasgupta, Francois Lorant, and William A. Goddard. ReaxFF: a reactive force field for hydrocarbons. *J. Phys. Chem. A*, 105 (41):9396–9409, 2001. doi: 10.1021/jp004368u.

W.F. van Gunsteren, P.K. Weiner, T. Wilkinson, and A.J. Wilkinson. *Computer Simulation of Biomolecular Systems: Theoretical and Experimental Applications*. Number v. 3 in Computer Simulation of Biomolecular Systems: Theoretical and Experimental Applications. Springer, 1997. ISBN 9789072199256.

David Vanderbilt. Soft self-consistent pseudopotentials in a generalized eigenvalue formalism. *Phys. Rev. B*, 41(11):7892–7895, 1990. doi: 10.1103/physrevb.41.7892.

Andrij Vasylenko. Private communication. 2016.

V Venugopal, R Prasad, and D.D Sood. Vaporisation thermodynamics of caesium iodide and caesium chromate. *Journal of Nuclear Materials*, 130:115–121, 1985. ISSN 0022-3115. doi: 10.1016/0022-3115(85)90300-9.

S.H. Walmsley and A. Anderson. Far infra-red spectra of molecular crystals. *Molecular Physics*, 7(5):411–416, 1964. ISSN 1362-3028. doi: 10.1080/00268976300101181.

C. T. White, D. H. Robertson, and J. W. Mintmire. Helical and rotational symmetries of nanoscale graphitic tubules. *Phys. Rev. B*, 47(9):5485–5488, 1993. doi: 10.1103/physrevb.47.5485.

Jeroen W. G. Wilder, Liesbeth C. Venema, Andrew G. Rinzler, Richard E. Smalley, and Cees Dekker. Electronic structure of atomically resolved carbon nanotubes. *Nature*, 391(6662):59–62, 1998. doi: 10.1038/34139.

Mark Wilson. Structure and phase stability of novel 'twisted' crystal structures in carbon nanotubes. *Chemical Physics Letters*, 366(5-6):504–509, 2002. doi: 10.1016/s0009-2614(02)01613-5.

Mark Wilson. Formation of, and ion-transport in, low-dimensional crystallites in carbon nanotubes. *Faraday Discuss.*, 134:283–295, 2007. ISSN 1364-5498. doi: 10.1039/b602488b.

Ying Xu, John S. Tse, Artem R. Oganov, Tian Cui, Hui Wang, Yanming Ma, and Guangtian Zou. Superconducting high-pressure phase of cesium iodide. *Physical Review B*, 79(14), 2009. doi: 10.1103/physrevb.79.144110.

B. I. Yakobson, C. J. Brabec, and J. Bernholc. Nanomechanics of carbon tubes: Instabilities beyond linear response. *Physical Review Letters*, 76(14):2511–2514, 1996. doi: 10.1103/physrevlett.76.2511.

ChiYung Yam, ChiChiu Ma, XiuJun Wang, and GuanHua Chen. Electronic structure and charge distribution of potassium iodide intercalated single-walled carbon nanotubes. *Appl. Phys. Lett.*, 85(19):4484, 2004. doi: 10.1063/1.1819510.

Shu Zhen and G. J. Davies. Calculation of the Lennard-Jones n–m potential energy parameters for metals. *Physica Status Solidi (a)*, 78(2):595–605, 1983. doi: 10.1002/pssa.2210780226.